Thermodynamic Optimization of the Ca-RE and Mg-Ca-Nd Systems Coupled with Experimental Investigation

Department of Mining and Materials Engineering

McGill University

Montreal, Quebec, Canada

May 2019

A thesis submitted to McGill University in partial fulfillment of the requirements of the degree of Master of Engineering in the Department of Mining and Materials Engineering

TABLE OF CONTENTS

ABSTRACT

The main purpose of the present study is to obtain accurate thermodynamic database to describe the phase equilibria and thermodynamic properties of the entire Mg-Ca-Nd system, which can be utilized for Mg alloy design containing Ca and RE.

The Ca-RE (RE = Nd, Y, Ce) binary systems were optimized based on assessed phase diagram data. All available data in the literature were critically evaluated and used to optimize the model parameters to reproduce all available phase diagram data. Liquid solution was described using the Modified Quasichemical Model (MQM), and the solid solutions were described with the Compound Energy Formalism (CEF). It should be noted that all Ca-RE systems show liquid miscibility gap.

In order to facilitate the thermodynamic optimization of the Mg-Ca-Nd ternary system, key phase diagram experiments were performed to supplement the few existing phase diagram experimental data. Differential scanning calorimetry (DSC) was successfully conducted up to 750ºC on samples of 5 different compositions in the Mg-rich side and up to about 30 mole percent Nd and 50 mole percent Ca. To prevent the volatilization and oxidation of samples, sealed Fe capsule was employed. Based on the new phase diagram data and all available information in literature, thermodynamic optimization of the ternary Mg-Ca-Nd system was carried out. In particular, the solubility of Ca in $Mg_{41}Nd_5$ and Nd in Mg_2Ca were well reproduced by CEF. In general, the available phase diagram data were well reproduced and the phase diagram of the entire Mg-Ca-Nd system was predicted.

RÉSUMÉ

Le but principal de la présente étude est d’obtenir une base de données thermodynamique précise décrivant les équilibres de phase et les propriétés thermodynamiques de l’ensemble du système Mg-Ca-Nd pouvant être utilisés pour la conception d’alliages de Mg contenant du Ca et des RE (terres rares).

Les systèmes binaires Ca-RE (RE = Nd, Y, Ce) ont été optimisés en utilisant les données estimées du diagramme de phase. Toutes les données disponibles dans la littérature ont été évaluées de manière critique et utilisées pour optimiser les paramètres du modèle afin de reproduire toutes les données disponibles du diagramme de phase. La solution liquide a été décrite à l'aide du modèle quasichimique modifié (MQM), et les solutions solides ont été décrites avec le formalisme d'énergie des composés (CEF). Il convient de noter que tous les systèmes Ca-RE présentent une lacune de miscibilité liquide-liquide.

Afin de faciliter l'optimisation thermodynamique du système ternaire Mg-Ca-Nd, des expériences clés ont été réalisées pour compléter les quelques données expérimentales existantes du diagramme de phase. La calorimétrie à balayage différentiel (DSC) a été réalisée avec succès jusqu'à 750 °C sur des échantillons de 5 compositions différentes du côté riche en Mg et jusqu'à environ 30% en moles de Nd et 50% en moles de Ca. Pour éviter la volatilisation et l'oxydation des échantillons, une capsule de Fe scellée a été utilisée. Sur la base des nouvelles données du diagramme de phase et de toutes les informations disponibles dans la littérature, l'optimisation thermodynamique du système ternaire Mg-Ca-Nd a été réalisée. En particulier, la solubilité de Ca dans Mg41Nd5 et de Nd dans Mg2Ca a été bien reproduite par le CEF. En général, les données disponibles du diagramme de phase ont été bien reproduites et le diagramme de phase de l’ensemble du système Mg-Ca-Nd a été prédit.

ACKNOWLEDGMENTS

First of all, I would like to express my deep appreciation and sincere gratitude to my supervisors, Prof. In-Ho Jung and Prof. Stephen Yue, for their guidance, encouragement, critical advice and continuous support throughout my studies at McGill University. It has been a great honor and a true pleasure to work for professors with high achievements and great characters as my supervisors, Prof. Jung and Prof. Yue, and I am very lucky to gain inspiration from both of them.

I would like to express my very great gratitude to Research Associate Dr. Pierre Hudon for his vital assistance in experiments and technical writing, as well as Post-Doctoral Fellows Dr. Junghwan Kim and Dr. Zhijun Zhu for their guidance in thermodynamic optimizations.

I would also like to extend my deep gratitude to Prof. Jun Song for his crucial input in the joint research efforts on Mg alloy development, and his kind guidance as my committee member. The support from lab manager Dr. Lang Shi and my fellow students, Mr. Yang Liu and Mr. Li Xin has been instrumental in the EPMA experimental efforts. Great thanks to Dr. Florence Paray, Mr. Robert Paquette and Dr. Evelin Barbosa de Melo for the training and support they offered during the process of sample preparation. I would also like to thank Mr. Ranjan Roy for his diligent support in conducting the ICP-OES analysis.

I would like to also extend my sincere gratitude to members of Prof. Jung's research group: Dr. Marie-Aline Van Ende, Dr. Bikram Konar, Dr. Dong-geun Kim, Mr. Sunyong Kwon, Mr. Zhimin You, Dr. Sourav Kumar Panda, Ms. Xintong Du, Ms. Tiantian Yin, Mr. Jun-Hyung Lee, Mr. Kota Matsuo, Ms. Yumin Zhang and all other members for their great support. The same gratitude also extends to members of Prof. Yue's research group: Dr. Evelin Barbosa de Melo, Dr. Jing Su, Dr. Hanqing Che, Mr. Yang Liu, and other fellow members for their kind encouragements and support.

In addition, financial and technical support from Magna International Inc., CANMET-MTL laboratories, and NSERC through the CRD grant programs are gratefully acknowledged.

I would like to thank all staff members of the Mining and Materials Engineering Department at McGill University, for their great assistance and support.

Finally, I would like to take the opportunity to express my deepest gratitude to my family, my girlfriend, and my dear friends. Their love, encouragement, and continuous support have inspired me with purpose, resilience and vibrant creativity, which have been an indispensable part of this journey.

CONTRIBUTIONS TO ORIGINAL KNOWLEDGE

Thermodynamic optimization of the ternary Mg-Ca-Nd system was conducted based on critically assessed literature data in conjunction with experimental investigations through DSC analysis. The following contributions could be seen:

- As a prerequisite to the optimization efforts for the ternary system, the Ca-RE (RE = Nd, Y, Ce) binary systems were optimized based on the methodical review and assessment of all literature data. The Modified Quasichemical Model (MQM) was adopted for describing the liquid solution, while the solid solutions were described with the Compound Energy Formalism (CEF). Optimization results presented in this study mark a significant improvement in the accuracy and coherence in thermodynamic modeling for the Ca-RE (RE = Nd, Y, Ce) binary systems, and is compatible with existing optimizations on the Mg-Ca and Mg-RE binary systems.
- Differential scanning calorimetry (DSC) was carried out successfully on five ternary Mg-Ca-Nd alloys of different compositions in the Mg-rich side. With the employment of Fe capsules based on precision welding, the oxidation and volatilization problems which have long affected systems with high Ca or RE content were overcome. The DSC data for the Mg-Ca-Nd ternary system were acquired at compositions up to about 30 mole percent Nd and 50 mole percent Ca for the first time, expanding the scope of knowledge on the phase equilibria in the system.
- Optimization conducted on the ternary Mg-Ca-Nd system has successfully reproduced the experimental results. Based on the optimization, isothermal phase diagrams and liquidus projection of the ternary system could be accurately predicted. The optimized thermodynamic model could be integrated with the existing database for the Mg alloys, contributing to the design of various Mg alloys involving Ca and Nd.

1 INTRODUCTION

1.1 MAGNESIUM ALLOYS

The main interest in magnesium alloys from the industry lies in their light weight, great castability and machinability, as well as the relatively high specific strength. Commonly referred to as the "lightest structural metal", magnesium is 75% lighter than steel. Even aluminum counterparts are still 50% heavier at the same volume. Typical alloys such as AZ31 and AM60 have found a variety of usages in, most notably, the automobile sector (Fig. 1), [1] aviation, and consumer electronics, offering significant weight reduction and better fuel efficiency for transportations. As reported by the United States Automotive Materials Partnership, a collaboration between GM, Ford and Chrysler, estimated that "*...by 2020, 250 pounds of magnesium will replace 500 pounds of steel and 90 pounds of magnesium will replace 130 pounds of aluminum per vehicle, resulting in an overall 15% weight reduction*", while current use in gearboxes, steering wheels, and seat frames, utilizes roughly 10-12 pounds of magnesium, this number is still dwarfed "*compared to 260 lbs. of plastics, 280 lbs. of aluminum, and 2,150 lbs. of steel/cast iron*". [2, 3]

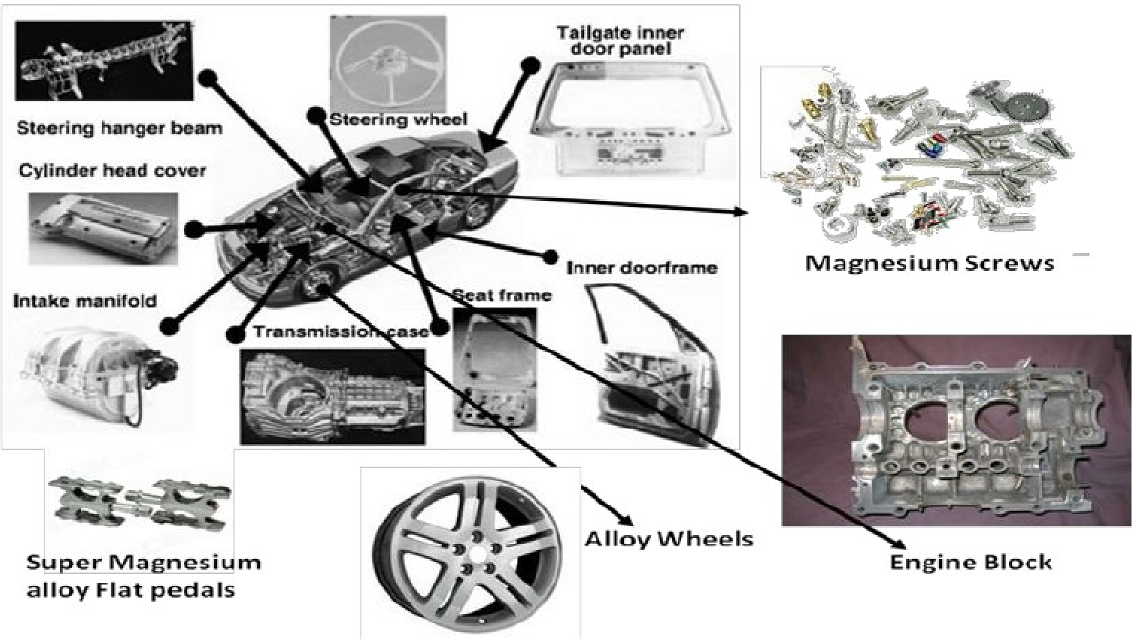

Figure 1, Examples of components made by magnesium alloys (Kulekci 2008) [1]

With the ongoing demand for better fuel economy and stricter environmental regulations, growing demand from the automotive sector conceivably contributes to future increase of magnesium consumption, while developments in magnesium alloys, in turn, would be of direct benefits to the automobile industry, which represents 14% production revenue and 115,000 employment for Canadian domestic manufacturing industry, and stands for over 1.94 trillion dollars of revenue worldwide (2013, Statistics Canada). [4]

1.2 CHOICE OF ALLOYING ELEMENTS

Despite all the promising aspects, pure magnesium faces a series of serious constraints when it comes to utilization, which involves its flammability, corrosion issues, creep under high temperature and poor formability related to excessive work hardening. Certain combinations of alloying elements have been chosen to mitigate the problems as illustrated in Fig. 2, [5] which include Al, Zn, Mn, Si, Li, Sr, Sn, Sc and noticeably, Ca and rare earth elements (REE) such as yttrium (Y) and neodymium (Nd).

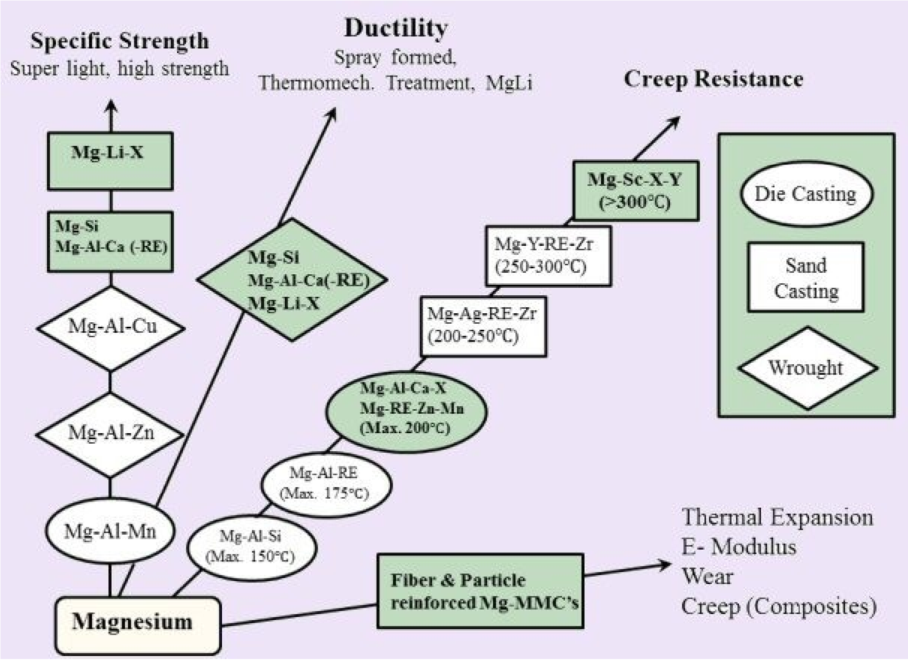

Figure 2, Evolution of the Mg alloys (Mordike and Ebert 2001) [5]

The use of calcium (Ca) in magnesium alloys is known to be one of the most effective ways for improving mechanical performances and creep resistance for magnesium alloys. Research by Pekguleryuz and Renaud [6] found that the addition of Ca in Mg-Al alloy helped to improve tensile strength, creep resistance, while achieving corrosion resistance comparable to commercialized Mg alloys with rare earth elements. Zhou et al. [7] also confirmed that Ca addition in AZ91 magnesium alloy as a cost-effective way to enhance mechanical properties at elevated temperatures. Stanford[8] further suggested that Ca exhibited similar behavior as rare earth elements when alloyed with magnesium due to its large atomic radius, and the presence of Ca effectively weakened the extrusion texture in the Mg-1.3Mn alloy.

Rare earth elements (REE) are practically known to improve castability and provide solid solution and precipitation hardening at both ambient and elevated temperature, resulting in enhanced tensile strength and creep resistance. Yttrium, in particular, is commonly used for grain refinement and better corrosion resistance. Jung et al. [9] at McGill University studied the role of rare earth elements in deformation and recrystallization of Mg alloys, identifying the changes in stack fault energy (SFE) in hcp magnesium, and enhancement of the solute-drag effect of grain boundaries and dislocations as two crucial factors for texture weakening. It is further suggested that due to the high concentrations of REE required for ideal texture weakening in binary alloys, along with the ineffectiveness of binary and ternary REE precipitants towards this goal, use of costly REE could be minimized based on solubility limit in hcp Mg (Fig. 3), and ternary or higher order Mg alloys would be a preferable choice.

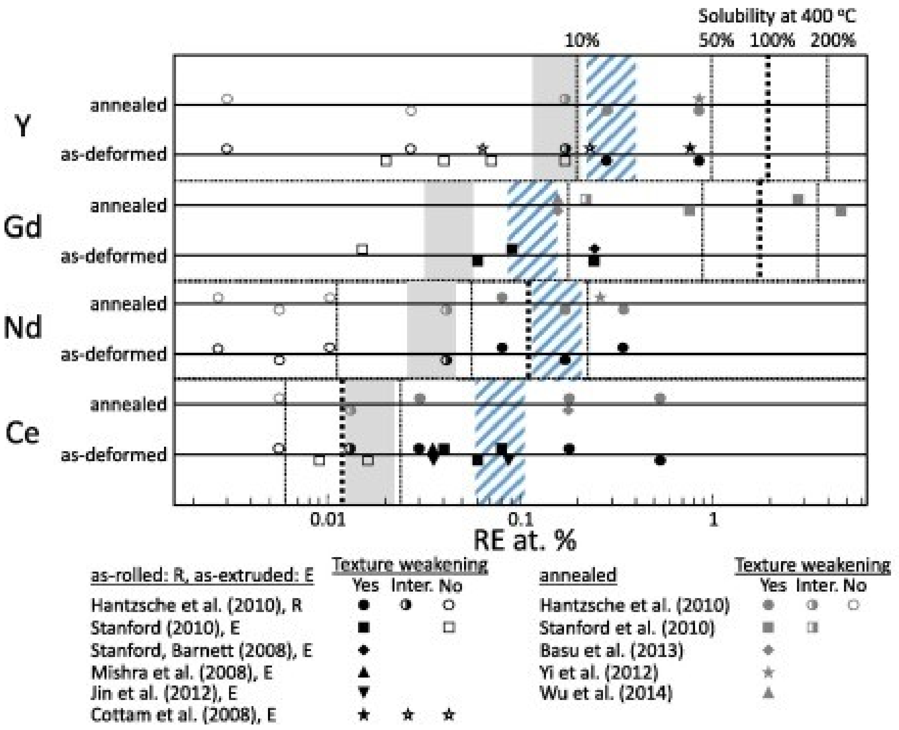

Figure 3, Critical amounts of REE necessary for texture weakening in the Mg-RE systems during deformation and post-annealing conditions at about 400 °C (Jung et al. 2014) [9]

1.3 PURPOSE OF THE PRESENT STUDY

The present study is inspired by the development of high-performance, high-formability Mg alloys containing calcium and rare earth elements (REE), with neodymium as the most notable candidate. In order to achieve the desired formability through texture-weakening while maintaining cost-effectiveness, it is necessary to minimize the use of REE based on a well-established model with accurate predictions of the solid solubility of REE in the Mg matrix, while accounting for the synergistic effect of Ca presence.

This study aims to achieve a thermodynamic database which could accurately describe and predict the phase equilibria as well as thermodynamic properties of the entire Mg-Ca-Nd system, which would greatly facilitate the design efforts toward high-formability Mg alloys with minimal Nd usage, as well as any future studies related to Mg alloys containing Ca and Nd.

Optimization of the ternary Mg-Ca-Nd system would be achieved by re-assessing and optimizing the binary Ca-Nd systems, followed by the optimization of the ternary system. Furthermore, two other Ca-RE (RE = Y, Ce) systems with application potentials would also be investigated and optimized, which would offer a solid foundation for future efforts in alloy development and thermodynamic studies involving Ca-RE systems.

2 THERMODYNAMIC MODELING METHODOLOGY

2.1 THE CALPHAD METHOD

One of the paramount goals for materials engineering lies in understanding the underlying interaction between chemical composition, processing, resulting microstructure, and properties. Phase transitions are often involved in processes such as melting and solidification, introducing of alloying elements, annealing, quenching or hot extrusion, where phase diagrams are utilized as a crucial aid. However, limited availability of ternary or higher order phase diagrams calls for an effective extrapolation technique so that through combination and reasonable optimization efforts, higher order phase diagrams of interest could be deduced with accuracy.

The pioneering work by Kaufman et al. [10] in the early 1970s marks the inception of computational thermodynamics, evolving into what is known today as the CALPHAD method. Short for *CALculation of PHAse Diagrams*, this method is based on the fact that the phase diagram, as a representation of thermodynamic properties of a system, can be derived if sufficient experimental data are available to describe the system. Description of the Gibbs free energy of all phases is used as a common starting point for the calculations due to the ease of describing the Gibbs energy from a relatively small set of polynomials in relation to temperature and chemical composition. The description can be verified and optimized based on all available experimental measurements of melting points, solubility limits, phase transformation reaction temperatures, alongside thermodynamic properties including enthalpies of formation, entropy data, heat capacities, and chemical potentials. Modeling usually starts with well-established data of the unary and binary systems, which could then be expanded into higher-order systems (Fig. 4). [11, 12]

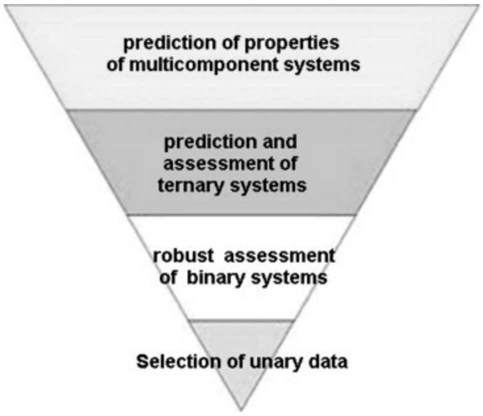

Figure 4, Sequence of modeling the thermodynamic properties of systems with the CALPHAD method (Kroupa 2012) [11]

2.2 PROCEDURE OF THERMODYNAMIC OPTIMIZATION

The typical workflow of utilizing the CALPHAD method in thermodynamic modeling and optimization consists of gathering and critically reviewing all available experimental measurements and theoretical predictions related to phase equilibria and thermodynamic description of the defined system, choosing the proper model for extrapolation, and mathematically fitting parameters to recalculate the phase diagram.

For the specific task of thermodynamically optimizing the binary Ca-RE system and the ternary Mg-Ca-Nd system, the following steps are taken in the present study:

- Review and critically assess all the available literature on binary and ternary systems
- Design and conduct experimental investigation for the binary or ternary system, if necessary
- Optimize the Mg-Ca-Nd system
- Utilize the results in Mg alloy design for better formability and overall performance

The general procedure of the thermodynamic optimization of the Ca-RE and Mg-Ca-Nd systems is presented in Figure 5:

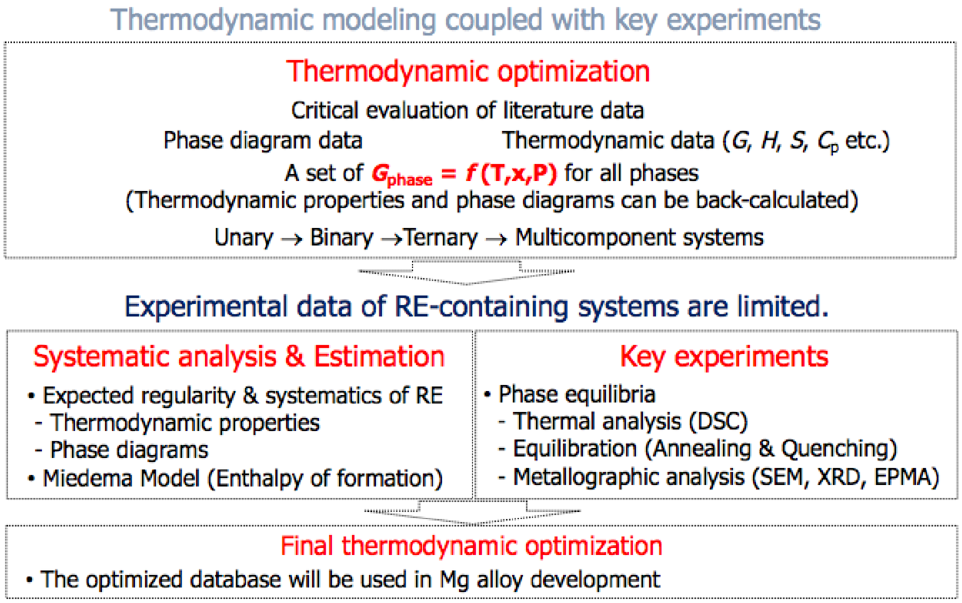

Figure 5, General procedure of the thermodynamic optimization

2.3 THE GOVERNING EQUATIONS

The Gibbs energy of a stoichiometric compound is expressed as:

$$G_T^{\circ} = H_T^{\circ} - TS_T^{\circ} \quad \ldots (1)$$

where, enthalpy H_T° and entropy S_T° are expressed by the standard enthalpy of formation ΔH_{298K}°, standard entropy S_{298K}°, and heat capacity Cp:

$$H_T^{\circ} = \Delta H_{298K}^{\circ} + \int_{298K}^{T} Cp\, dT\,;\ S_T^{\circ} = S_{298K}^{\circ} + \int_{298K}^{T} \frac{Cp}{T}\, dT \quad \ldots (2)$$

The Modified Quasichemical Model (MQM) in the pair approximation is used for the liquid solution, and is described as follows: [13]

$$(\mathrm{A}-\mathrm{A}) + (B-B) = 2(A-B) \quad \ldots (3)$$

$$G_{solution} = \left(n_A g_A^{\circ} + n_B g_B^{\circ}\right) - T\Delta S_{conf} + \left(\frac{n_{AB}}{2}\right)\Delta g_{AB} \quad \ldots (4)$$

$$\Delta S_{conf} = -R(n_A lnX_A + n_B lnX_B) - R(n_{AA} \ln\left(\frac{X_{AA}}{{Y_A}^2}\right) + n_{BB}\ln\left(\frac{X_{BB}}{{Y_B}^2}\right) + n_{AB}\ln\left(\frac{X_{AB}}{2\,Y_A Y_B}\right)) \quad \ldots(5)$$

$$\Delta g_{AB} = \Delta g_{AB}^{\circ} + \sum_{i\geq 1} g_{AB}^{i0} X_{AA}^{i} + \sum_{j\geq 1} g_{AB}^{0j} X_{BB}^{j} \quad \ldots (6)$$

where Δg_{AB} stands for the Gibbs free energy of the pair exchange reaction (3), g_A° and g_B° are the molar Gibbs energies of pure A and B, n_{AB} is the moles of (A-B) pairs present in the solution, and ΔS_{conf} stands for the configurational entropy by randomly mixing (A-A), (B-B) and (A-B) pairs in the one-dimensional Ising approximation. X_{ij} stand for (i-j) pair fraction; X_A, and X_B represent the overall mole fractions of element A and B, and "coordination-equivalent" fractions Y_A and Y_B are defined as:

$$Y_A = X_{AA} + \frac{X_{AB}}{2}\,;\ Y_B = X_{BB} + \frac{X_{AB}}{2} \quad \ldots (7)$$

Δg°_{AB}, g^{i0}_{AB} and g^{0j}_{AB} which can be function of temperature are the model parameters to be optimized in the MQM. The equilibrium pair distribution is calculated by setting:

$$\left(\frac{\partial \mathrm{G}}{\partial n_{AB}}\right)_{n_A,n_B} = 0 \quad \dots(8)$$

The Compound Energy Formalism (CEF) is chosen to describe the solid solution phases: [14]

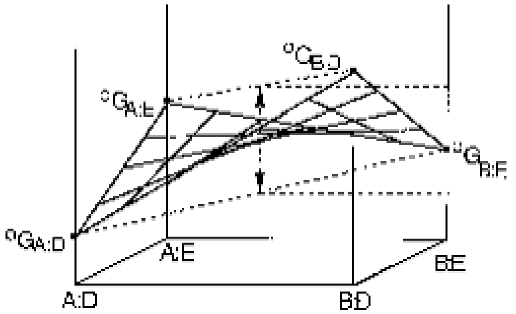

$$(A)_p[D]_q - (B)_p[E]_q \; mixture$$

$$\rightarrow (A,B)_p[D,E]_q$$

$$G^{(A,B)(D,E)} = y'_A y''_D G^{\circ,(A,B)(D,E)}_{A:D} + y'_A y''_E G^{\circ,(A,B)(D,E)}_{A:E} + y'_B y''_D G^{\circ,(A,B)(D,E)}_{B:D} + y'_B y''_E G^{\circ,(A,B)(D,E)}_{B:E} + RT(y'_A \ln y'_A + y'_B \ln y'_B) + RT(y''_D \ln y''_D + y''_E \ln y''_E) + \sum_i L^i_{A,B:D}(y'_A - y'_B)^i y'_A y'_B y''_D + \sum_i L^i_{A,B:E}(y'_A - y'_B)^i y'_A y'_B y''_E + \sum_i L^i_{A:D,E}(y''_D - y''_E)^i y'_A y''_D y''_E + \sum_i L^i_{B:D,E}(y''_D - y''_E)^i y'_B y''_D y''_E + L_{(A,B)(D,E)} y'_A y'_B y''_D y''_E \quad \dots(9)$$

where $\mathrm{y'}_{\mathrm{A}}$, and $\mathrm{y'}_{\mathrm{B}}$ stand for the site fractions of element A and B in the first sublattice, while $\mathrm{y''}_{\mathrm{D}}$and $\mathrm{y''}_{\mathrm{E}}$ correspond to the site fractions of element D and E in the second sublattice. $\mathrm{G}^{\circ,(\mathrm{A,B})(\mathrm{D,E})}_{\mathrm{A:D}}$, $\mathrm{G}^{\circ,(\mathrm{A,B})(\mathrm{D,E})}_{\mathrm{A:E}}$, $\mathrm{G}^{\circ,(\mathrm{A,B})(\mathrm{D,E})}_{\mathrm{B:D}}$, $\mathrm{G}^{\circ,(\mathrm{A,B})(\mathrm{D,E})}_{\mathrm{B:E}}$ are the Gibbs energies of end members AD, AE, BD, and BE, which are temperature-dependent.

$L^i_{A,B:D}$, $L^i_{A,B:E}$, $L^i_{A:D,E}$, $L^i_{B:D,E}$, $L_{(A,B)(D,E)}$ are interaction parameters which could be optimized to reproduce the experimental phase diagram or thermodynamic property data.

3 REVIEW OF LITERATURE

3.1 THE CALCIUM-NEODYMIUM BINARY SYSTEM

The phase diagram for the Ca-Nd system was proposed by Stroganova et al. [15] based on their thermal analysis and metallographic examination, and was assessed later by Gschneidner and Calderwood, [16] as depicted in Figure 6 below. The other assessment on the Ca-Nd system was conducted by Predel,[17] yielding highly similar results. No thermodynamic data was reported on the Ca-Nd system.

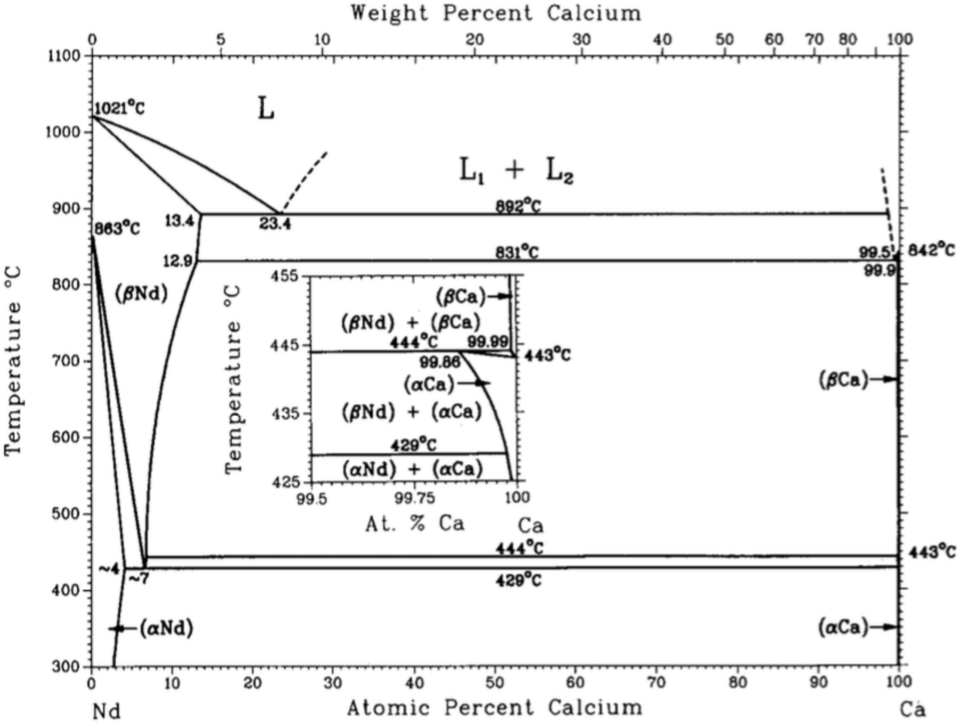

Figure 6, Assessed phase diagram of the Ca-Nd system (Gschneidner and Calderwood 1987) [16]

The purity of the starting materials and the method employed for alloy preparation were not reported by Stroganova. [15] However, some insights might be gained from another research, where the same authors conducted research on the Ca-Y and Ca-Eu systems. [18] They reported the use of sealed containers in order to overcome the issues induced by the high vapor pressure of calcium: molybdenum container was employed for Ca-Y alloys, while iron containers with tantalum foil liner were used for Ca-Eu alloys. It would be likely that the same or a similar method was employed for studying the Ca-Nd system.

Gschneidner and Calderwood [16] also reported the crystal structure data for the Ca-Nd system, summarized in Table 1.

Table 1, The summary of the Ca and Nd crystal structure data (Gschneidner and Calderwood 1987) [16]

Phase	Composition at. % Ca	Pearson symbol	Space group	Strukturbericht designation	Prototype
α-Nd	0	*hP*4	$P6_3/mmc$	*A*3’	α-La (DHCP)
β-Nd	0	*cI*2	$Im\overline{3}m$	*A*2	W (BCC)
α-Ca	100	*cF*4	$Fm\overline{3}m$	*A*1	Cu (FCC)
β-Ca	100	*cI*2	$Im\overline{3}m$	*A*2	W (BCC)

3.2 THE CALCIUM-YTTRIUM BINARY SYSTEM

Stroganova et al. [18] investigated the phase diagram of the Ca-Y system over the entire concentration range using a combined approach of thermal, dilatometric, microstructures, X-ray structural analysis, micro-hardness, as well as electrical resistivity. The Ca-Y alloy samples were successfully prepared with the help of sealed molybdenum containers. However, no compositional analysis was reported on the starting materials. According to their proposed phase diagram (Fig. 7 (a)), it would be reasonable to assume that the reported data points are based on differential thermal analysis (DTA), featuring a series of transition temperatures for specific alloy compositions.

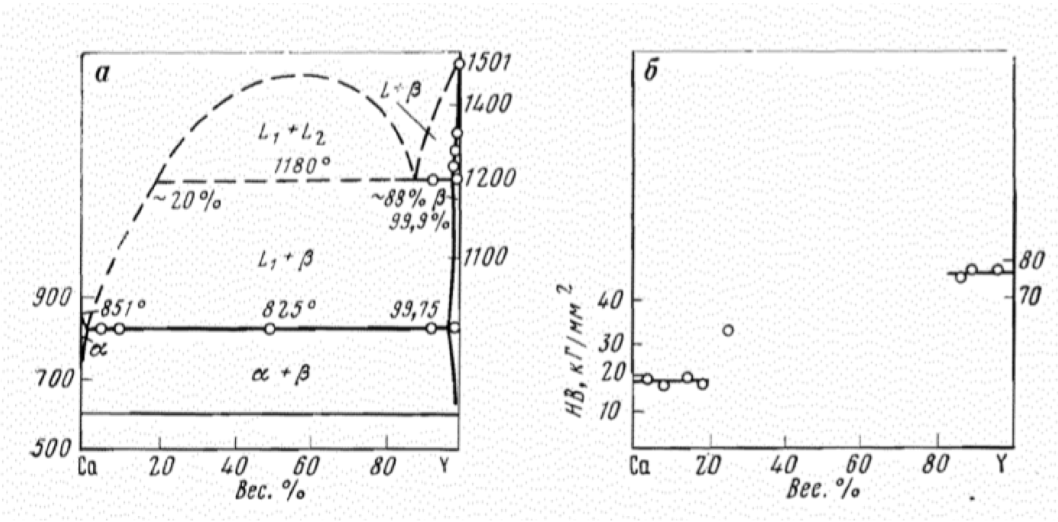

Figure 7, (a) Phase diagram and (b) composition - hardness diagram of the Ca-Y system (Stroganova et al. 1971) [18]

X-axis: Weight % of Y; Y-axis: Temperature, ºC; HB, kilogram-force / mm² (kgf/mm²)

The Ca-Y phase diagram proposed by Stroganova et al. [18] listed the melting point of Ca at 851 ºC (9 ºC lower than the accepted value at 842 ºC), while the melting point of Y was listed at 1501 ºC (21ºC lower than the 1522 ºC accepted value). Unfortunately, detailed analytical conditions and experimental error were not specified in their paper. They also reported the monotectic reaction at 88 wt.% of Y with another liquid composition at 20 wt.% of Y, but no details were given for this invariant reaction.

Gschneidner and Calderwood [19] assessed the experiments of Stroganova et al. on the Ca-Y system, suggesting to raise the monotectic temperature from the 1180 ºC reported by Stroganova to 1200 ºC, while lowering the eutectic temperature from the reported 825 ºC to 815 ºC. The adjustments maintain the approximate temperature difference (within ±1ºC) between the reported invariant reaction temperatures and the melting point of adjacent metals, while correcting the Ca, Y melting points to the accepted values summarized by Haynes. [20]

Dzhuraev and Altynbaev [21] re-determined the phase equilibria through the systematic modeling of the Ca (Sr, Ba) - Sc (Y) systems (see Fig. 8), employing a combination of ideal and regular solution model, supplemented by the Hildebrand-Mott model in determining the limits of liquid immiscibility and solid solubility. The liquid immiscibility ranges from 10.0-76.8 at.% of Y, which highly agrees with results reported Stroganova et al. [18]

The modeling was refined with corrections based on the relative ionization potentials, for determining temperatures for the invariant reactions. However, the estimated 1050 ºC monotectic and 756 ºC eutectic temperatures were significantly lower than the respective 1180 ºC and 825 ºC reported by Stroganova based on DTA results. The latter data, after correcting for the melting points of pure metals, were adopted for the present optimizations.

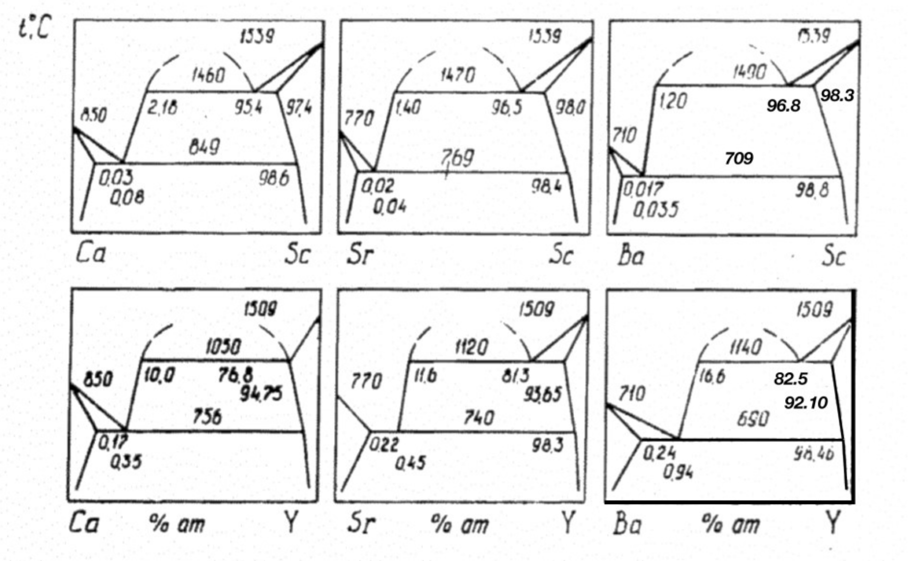

Figure 8, Calculated phase diagrams of Ca, Sr, and Ba with Sc and Y (Dzhuraev and Altynbaev 1986) [21]

X-axis: at. %; Y-axis: temperature, ºC

Predel[22] re-evaluated all the previous works [18, 19, 21] and presented an assessed Ca-Y phase diagram based on the review by Moffatt, [23] as shown in Fig. 9. Note that in Fig. 9, the two-phase region Liquid+α-Y is added, correcting what would likely be an error made by Dzhuraev and Altynbaev in Fig. 8. Their estimation with the solid solubility of calcium in α-Y (HCP) contradicts the experimental study by Stroganova et al. [18] while the estimation of the range of liquid immiscibility seems to be in good agreement.

The crystal structure information for the Ca-Y system is summarized by Gschneidner and Calderwood, [19] as listed in Table 2. No thermodynamic data have been reported on the Ca-Y system so far.

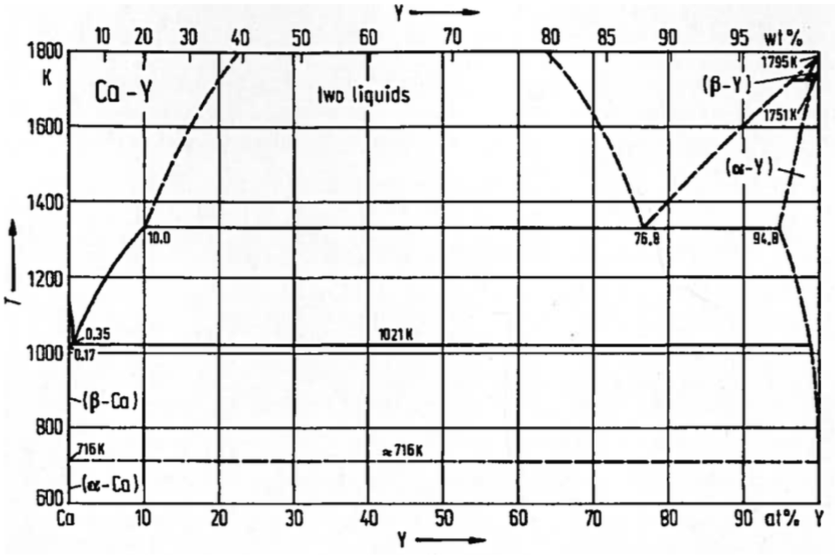

Figure 9, Reported phase diagram of the Ca-Y system (Predel 1993) [22]

Table 2, The summary of the Ca and Y crystal structure data (Gschneidner and Calderwood 1987) [19]

Phase	Composition at. % Ca	Pearson symbol	Space group	Strukturbericht designation	Prototype
α-Y	0	*hP*2	$P6_3/mmc$	*A*3	Mg (HCP)
β-Y	0	*cI*2	$Im\bar{3}m$	*A*2	W (BCC)
α-Ca	100	*cF*4	$Fm\bar{3}m$	*A*1	Cu (FCC)
β-Ca	100	*cI*2	$Im\bar{3}m$	*A*2	W (BCC)

3.3 THE CALCIUM-CERIUM BINARY SYSTEM

Zverev[24] investigated the Ca-Ce system as part of the Ce-Ca-Cl ternary system. His results were assessed later by Gschneidner and Calderwood. [25] Gschneidner and Calderwood also summarized crystal structure information for the Ca-Ce system, as listed in Table 3.

Table 3, The summary of the Ca and Ce crystal structure data (Gschneidner and Calderwood 1987) [25]

Phase	Composition at. % Ca	Pearson symbol	Space group	Strukturbericht designation	Prototype
α-Ce	0	*cF*4	$Fm\bar{3}m$	*A*1	Cu (FCC)
β-Ce	0	*hP*4	$P6_3/mmc$	*A*3’	α-La (DHCP)
γ-Ce	0	*cF*4	$Fm\bar{3}m$	*A1*	Cu (FCC)
δ-Ce	0	*cI*2	$Im\bar{3}m$	*A2*	W (BCC)
α-Ca	100	*cF*4	$Fm\bar{3}m$	*A*1	Cu (FCC)
β-Ca	100	*cI*2	$Im\bar{3}m$	*A*2	W (BCC)

Zverev[24] prepared the alloys by melting the starting materials (>99.5% for cerium, and >99.9% for calcium) in a sealed molybdenum bomb used as a container, and protected by a moisture-free argon / N_2 mixture. The materials were heated up and annealed at a series of temperatures from 1100-1200 ºC for 0.5-2 hours, and then quenched in water, followed by chemical and microscopic analysis. Methodology for the chemical analysis was not specified, although it was noted that the samples selected for analysis were microscopically checked to ensure the reflection of average compositions. Zverev reported that the liquid immiscibility range extends from ~1.5 to 99.4 at. % Ca at the monotectic temperature of 843 ºC. In addition, the eutectic reaction was determined at 801.8 ºC with a composition of ~ 0.3 at. % Ca (Fig. 10). Both temperatures were calculated results according to the Schroder rule, while the compositions were determined by experiments. In the study of Zverev, the melting points (T_m) of pure Ca and Ce were reported as 850 ºC and 804 ºC, respectively, while the accepted values are at 842 ºC and 798 ºC. It is noteworthy that Gschneidner and Calderwood, [25] for some reason, appears to have mistaken T_m (Ce) by Zverev for 795 ºC instead of the original 804 ºC, while inaccurately taking 792 ºC instead of the originally 801.8 ºC as the eutectic temperature determined by Zverev.

Based on the original data from Zverev, [24] the corrected eutectic temperature should be at 795.8ºC. Despite the misinformed data in their research, Gschneidner and Calderwood [25] happen to have canceled out the error, proposing a eutectic temperature at 795ºC, with a minor difference of only 0.8 ºC.

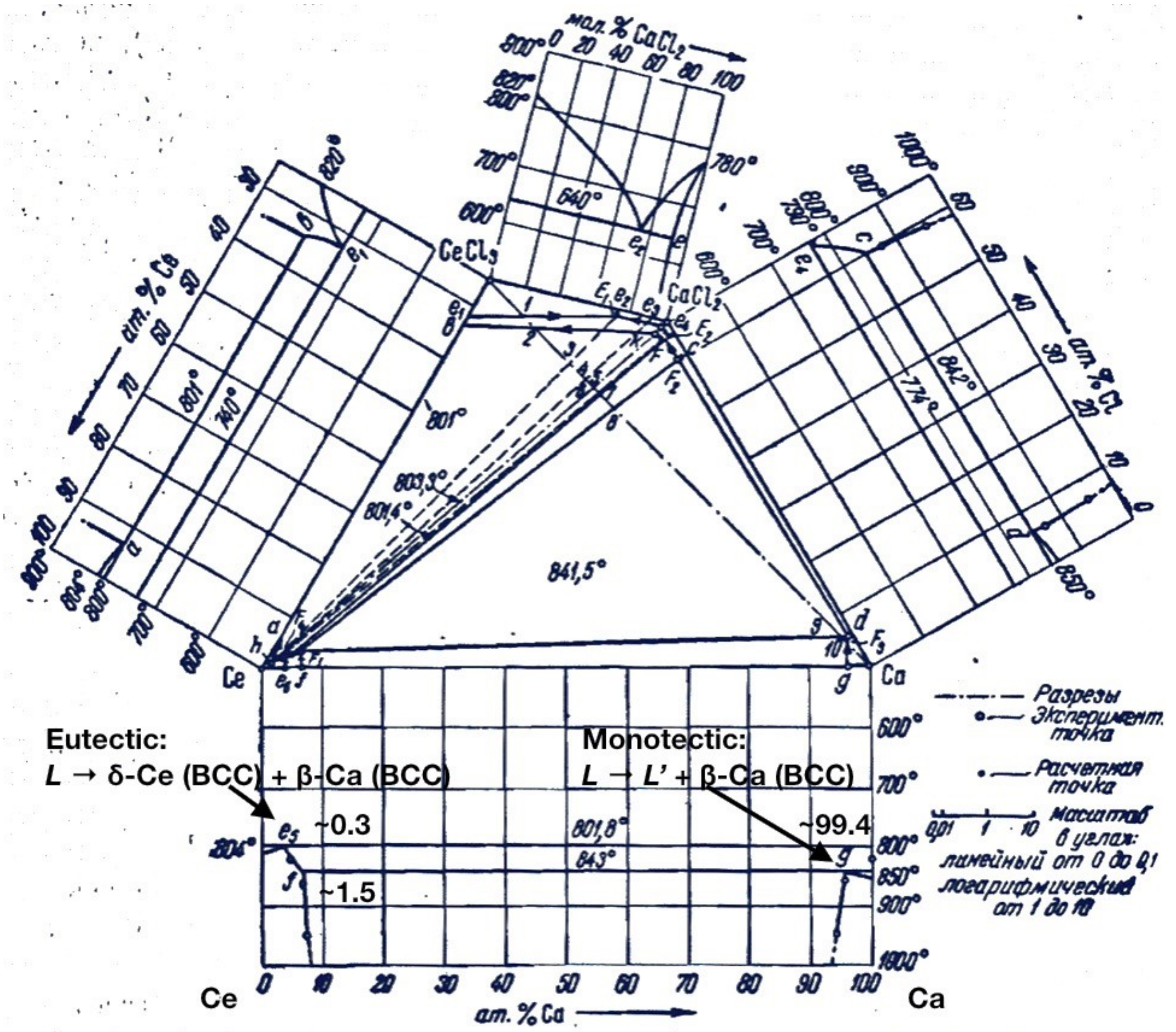

Рис. 1. Приближенная диаграмма плавкости системы Ce—Ca—Cl

Figure 10, Approximate melting diagram of the Ce - Ca - Cl system (Zverev 1955) [24]

am. %: atomic percent, at. %

3.4 OVERVIEW OF LITERATURE ON THE OTHER CA-RE SYSTEMS

Among all the rare earth elements, the body-centered cubic (BCC) structure appears in 13 out of a total of 17 rare earth elements. The hexagonal crystal family, including 11 cases of hexagonal close-packed (HCP) structure, 5 cases of double-hexagonal close-packed (DHCP) structure, as well as the α-Sm with its rhombohedral structure, is also highly predominant among rare earth elements. There are 4 appearances of face-centered cubic (FCC) structure: β-La, α-Ce, γ-Ce, and β-Yb. Table 4 summarizes the available crystal structure data of calcium and all RE elements (RE = Sc, Y, La, Ce, Pr, Nd, Pm, Sm, Eu, Gd, Tb, Dy, Ho, Er, Tm, Yb, and Lu). [15-19, 21-39]

The phase diagrams of the most binary Ca-RE systems have been determined, although the sources of data are usually scarce due to a combination of experimental difficulties and limited focus on these systems. Gschneidner and Calderwood [16, 19, 25, 28-34, 36] have conducted a comprehensive review and assessment on many Ca-RE systems, supplemented by the rather concise reviews by Predel. [17, 22, 27, 35, 38] Stroganova et al. [15, 18] made significant experimental contributions to a large number of the Ca-RE systems with fairly convincing methods of sample preparation and analysis. A brief summary of all available phase diagrams of the Ca-RE systems is presented below for systematic comparison (see Fig. 11). In total, only 7 binary systems (Ca-RE, RE=Y, La, Ce, Nd, Eu, Tm, Yb) among the 17 Ca-RE systems have been presented with a phase diagram. No experimental data is found for the Ca-Sc, Ca-Pr, Ca-Pm, Ca-Tb, Ca-Ho, and Ca-Lu systems. Gschneidner and Calderwood [30, 32-34] stated that liquid immiscibility is observed in the Ca-Sm, Ca-Gd, Ca-Dy, and Ca-Er systems. The solid solubility of Ca in RE is reported to be less than 0.2% for all five systems with unspecified unit.

Some similarities can be found in the five Ca-RE systems, the Ca-Y, Ca-La, Ca-Ce, Ca-Nd, and Ca-Tm systems. All five systems share a rather wide range of liquid immiscibility, with rather limited solid solution of RE in calcium. Solid solubility of Ca in RE varies, ranging from significant solid solubility in the case of Ca-La and Ca-Nd to moderate level of solubility of Ca in Tm, and then, in the case of Ca-Y and Ca-Ce, only minimal levels of solid solubility. [16, 17, 19, 22, 25, 28, 35]

Table 4, The summary of the Ca and RE crystal structure data [15-19, 21-39]

Phase	Pearson symbol	Space group	Strukturbericht designation	Prototype
α-Ca	*cF*4	$Fm\bar{3}m$	*A*1	Cu (FCC)
β-Ca	*cI*2	$Im\bar{3}m$	*A*2	W (BCC)
α-Sc	*hP*2	$P6_3/mmc$	*A*3	Mg (HCP)
β-Sc	*cI*2	$Im\bar{3}m$	*A*2	W (BCC)
α-Y	*hP*2	$P6_3/mmc$	*A*3	Mg (HCP)
β-Y	*cI*2	$Im\bar{3}m$	*A*2	W (BCC)
α-La	*hP*4	$P6_3/mmc$	*A*3’	α-La (DHCP)
β-La	*cF*4	$Fm\bar{3}m$	*A*1	Cu (FCC)
γ-La	*cI*2	$Im\bar{3}m$	*A*2	W (BCC)
α-Ce	*cF*4	$Fm\bar{3}m$	*A*1	Cu (FCC)
β-Ce	*hP*4	$P6_3/mmc$	*A*3’	α-La (DHCP)
γ-Ce	*cF*4	$Fm\bar{3}m$	*A*1	Cu (FCC)
δ-Ce	*cI*2	$Im\bar{3}m$	*A*2	W (BCC)
α-Pr	*hP*4	$P6_3/mmc$	*A*3’	α-La (DHCP)
β-Pr	*cI*2	$Im\bar{3}m$	*A*2	W (BCC)
α-Nd	*hP*4	$P6_3/mmc$	*A*3’	α-La (DHCP)
β-Nd	*cI*2	$Im\bar{3}m$	*A*2	W (BCC)
α-Pm	*hP*4	$P6_3/mmc$	*A*3’	α-La (DHCP)
β-Pm	*cI*2	$Im\bar{3}m$	*A*2	W (BCC)
α-Sm	*hR*3	$R\bar{3}m$	-	α-Sm, Rhombohedral
β-Sm	*hP*2	$P6_3/mmc$	*A*3	Mg (HCP)
Eu	*cI*2	$Im\bar{3}m$	*A*2	W (BCC)
α-Gd	*hP*2	$P6_3/mmc$	*A*3	Mg (HCP)
β-Gd	*cI*2	$Im\bar{3}m$	*A*2	W (BCC)
α-Tb	*hP*2	$P6_3/mmc$	*A*3	Mg (HCP)
β-Tb	*cI*2	$Im\bar{3}m$	*A*2	W (BCC)
α-Dy	*hP*2	$P6_3/mmc$	*A*3	Mg (HCP)
α’-Dy	(a)	-	Orthorhombic distortion, T≤86K	
β-Dy	*cI*2	$Im\bar{3}m$	*A*2	W (BCC)
α-Ho	*hP*2	$P6_3/mmc$	*A*3	Mg (HCP)
β-Ho	*cI*2	$Im\bar{3}m$	*A*2	W (BCC)
Er	*hP*2	$P6_3/mmc$	*A*3	Mg (HCP)
Tm	*hP*2	$P6_3/mmc$	*A*3	Mg (HCP)
α-Yb	*hP*2	$P6_3/mmc$	*A*3	Mg (HCP)
β-Yb	*cF*4	$Fm\bar{3}m$	*A*1	Cu (FCC)
γ-Yb	*cI*2	$Im\bar{3}m$	*A*2	W (BCC)
Lu	*hP*2	$P6_3/mmc$	*A*3	Mg (HCP)

The Ca-Eu and Ca-Yb systems display a rather different pattern in terms of the phase diagram. As well known, all RE elements present systematic changes in their physico-chemical properties with atomic number. The only two exceptions are Eu and Yb due to their electron configurations: the half-full electron configuration on the 4f orbitals in the case of Eu ([Xe] $4f^7$ $6s^2$), and in the case of Yb, having full 4f orbitals ([Xe] $4f^{14}$ $6s^2$). This may be the reason that complete solid solutions between Ca-Eu and Ca-Yb exist in these two binary systems, [31, 36] while other Ca-RE systems have limited solid solubility between Ca and RE and even repulsive interaction in the liquid solution.

It is also noteworthy that no compound between Ca and RE exists in any of the seven known Ca-RE systems. This indicates that the atomic interaction between Ca and RE is not strong enough to form intermetallic compounds in solid state.

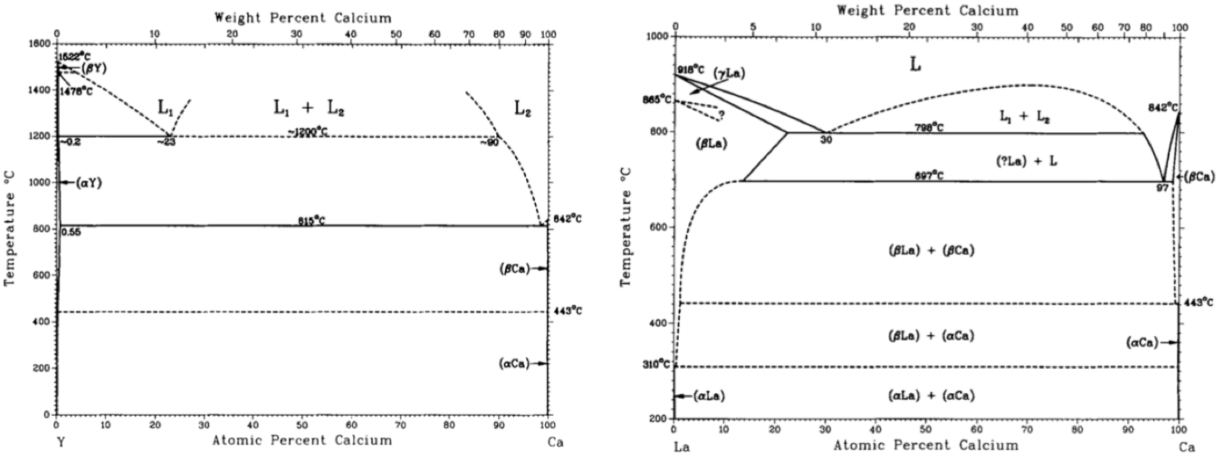

Y-Ca **La-Ca**

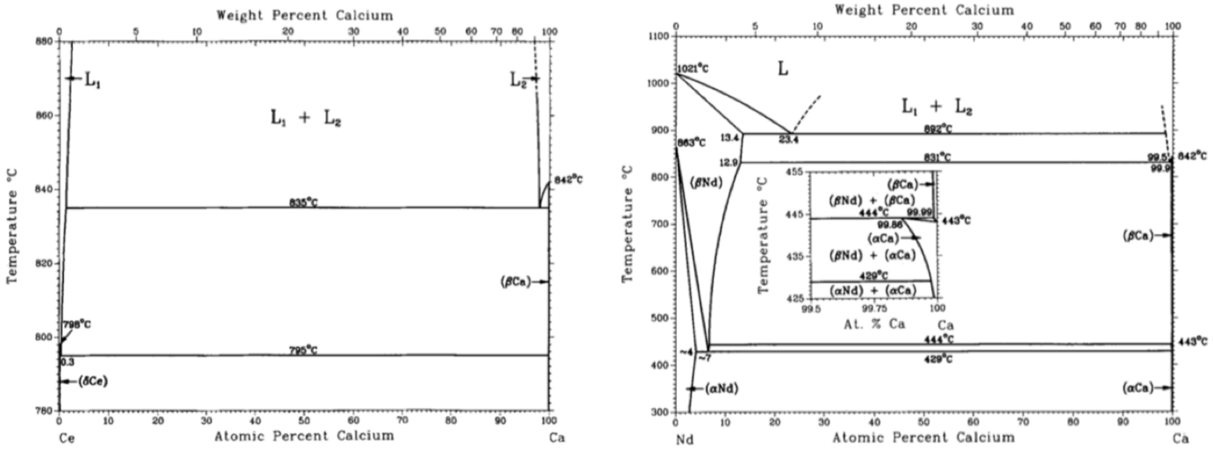

Ce-Ca **Nd-Ca**

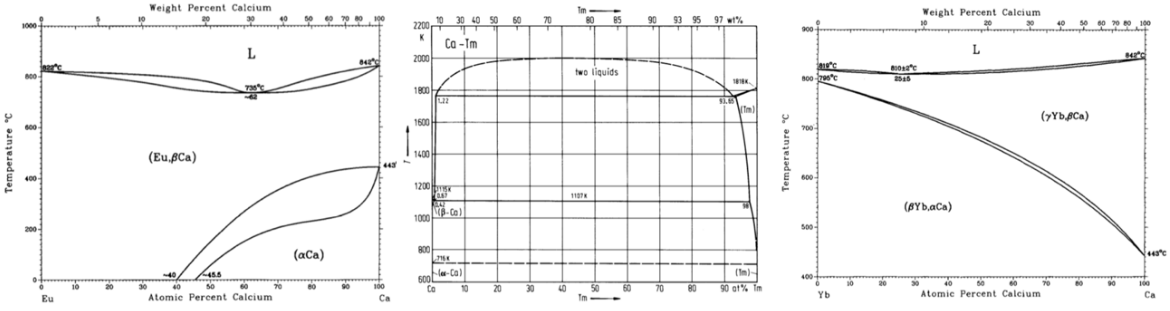

Eu-Ca **Ca-Tm** **Yb-Ca**

Figure 11, Summary of all available phase diagrams of the Ca-RE systems [16, 19, 25, 28, 31, 35, 36]

3.5 THE MAGNESIUM-CALCIUM-NEODYMIUM TERNARY SYSTEM

Fei et al. [40] studied the phase equilibria at 400 ºC in the Mg-rich corner of the Mg-Ca-Nd system. Samples were prepared from Mg-30%Nd and Mg-45%Ca master alloys (in wt.%), along with pure granular Mg (>99.99%), Ca (>99.9%), and Nd (>99.9%), presumably by weight percent. No detailed compositional analysis regarding the impurities in the master alloys was presented.

The raw materials were wrapped with tantalum foil and placed in sealed iron tubes, protected by an argon atmosphere. All tubes were kept at 800ºC for 4 hours, flipping every 45 minutes to promote homogenization, and subsequently water quenched. All equilibrated alloy samples were then subjected to 400ºC annealing for 1440 hours, or exactly 60 days.

Compositions of all 6 equilibrated alloy samples were determined by the chemical titration technique, with the phase constitutions examined by XRD, and the composition of each equilibrated phase analyzed by an electron probe microanalyzer (EPMA) at 20 kV. Results of the analyses were summarized in Table 5.

Some of the annealed samples were also analyzed using a heat flux differential scanning calorimeter (DSC), at a heating rate of 10 K/min. Fei was unable to perform multiple DSC runs due to the volatile nature of the alloys, and stated that only a single heating process was performed for each sample under a continuous argon flow. Result from alloy sample No. 2 was the only one presented in their research (Fig. 12), showing a eutectic transition $L \rightarrow \alpha\text{-Mg} + Mg_2Ca + Mg_{41}Nd_5$ at a temperature of 505.6 ºC. Although it was not specified in their description, they seem to have used open crucibles made of ceramics.

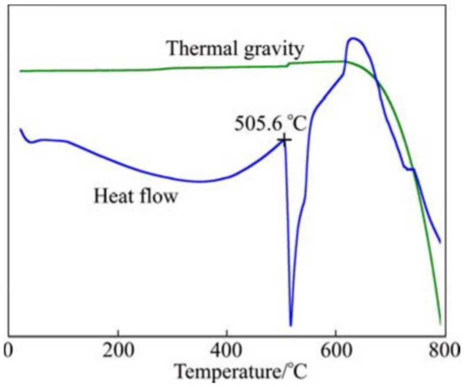

Figure 12, DSC curve of sample 2 in the Mg-Ca-Nd system after equilibrium treatment at 400 °C (Fei et al. 2012) [40]

Table 5, Equilibrium phase constituents in Mg-rich corner of Mg-Ca-Nd system at 400 °C (Fei et al. 2012) [40]

Sample No.	Starting composition (mol %)			Phase	Microprobe analysis (mol %)			Primary Crystal
	x(Mg)/%	x(Ca)/%	x(Nd)/%		x(Mg)/%	x(Ca)/%	x(Nd)/%	
1	94.32	2.87	2.81	α-Mg + Mg_2Ca + $Mg_{41}Nd_5$	99.48	0.34	0.18	α-Mg
					69.16	29.8	1.04	
					89.54	3.57	6.89	
2	91.37	5.7	2.93	α-Mg + Mg_2Ca + $Mg_{41}Nd_5$	99.89	0.06	0.05	Eutectic point
					69.41	29.8	0.79	
					90.25	3.32	6.43	
3	83.46	12.66	3.88	α-Mg + Mg_2Ca + $Mg_{41}Nd_5$	98.95	0.56	0.49	$Mg_{41}Nd_5$
					69.06	29.7	1.24	
					89.64	3.5	6.86	
4	71.34	24.76	3.9	Mg_2Ca + $Mg_{41}Nd_5$ + Mg_3Nd	69.99	29.01	1	Mg_2Ca
					89.47	3.1	7.43	
					74.89	0.24	24.87	
5	93.04	1.89	5.07	α-Mg + $Mg_{41}Nd_5$	99.82	0.08	0.1	α-Mg
					89.78	2.9	7.32	
6	86.15	1.81	12.04	Mg_3Nd + $Mg_{41}Nd_5$	75.32	0.13	24.55	$Mg_{41}Nd_5$
					89.46	2.11	8.43	

Based on the analytical results of the equilibrium phase constituents, Fei and his team have confirmed the existence of the three-phase regions α-Mg + Mg_2Ca + $Mg_{41}Nd_5$ and Mg_3Nd + Mg_2Ca + $Mg_{41}Nd_5$ in the Mg-rich corner for the Mg-Ca-Nd ternary system at its 400 ºC isothermal section. They also noted the rather broad two-phase regions of α-Mg + Mg_2Ca, α-Mg + $Mg_{41}Nd_5$, and Mg_3Nd + $Mg_{41}Nd_5$.

The solubility of Nd in Mg_2Ca at 400ºC is reported as 1.24 at. %, while the solubility of Ca in $Mg_{41}Nd_5$ reaches 3.57 at. %. They have also pointed out that based on the analyses of alloy No. 5, where α-Mg and $Mg_{41}Nd_5$ reaches a two-phase equilibrium with the latter dissolving 2.9 at. % Ca, it could be confirmed that an $Mg_{41}Nd_5$-based semi-continuous solid solution phase exists in the Mg-Ca-Nd system, while the possibility of a ternary compound is ruled out.

The proposed phase diagram for the Mg-Ca-Nd system in the Mg-rich corner at 400ºC is shown in Fig. 13.

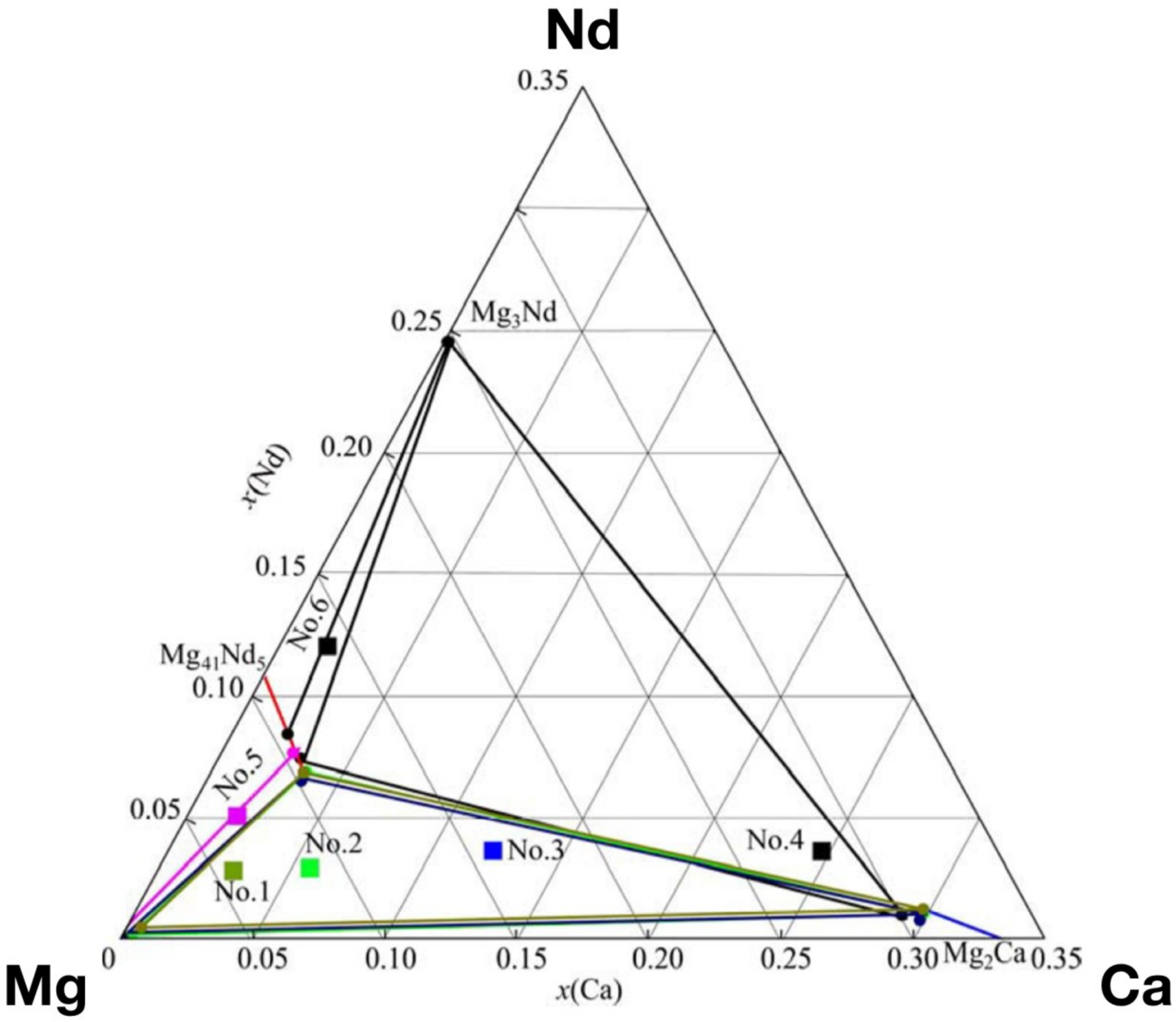

Figure 13, Phase diagram of Mg-rich corner in Mg-Ca-Nd system at 400 °C (Fei et al. 2012) [40]

4 EXPERIMENTAL PROCEDURES

4.1 PREPARATION OF THE HOMOGENIZED ALLOYS

In order to further investigate the phase diagram of the Mg-Ca-Nd ternary system, preparation of the homogenized Mg-Ca-Nd alloy would be the prerequisite for any further analytical attempts. The starting materials are Mg ingot (> 99.9 wt. % pure), Ca granules (> 99.5 wt. % pure), Nd ingot (> 99.9 wt. % pure), and Mg-Nd master alloy ingot (39.2 wt. % Nd, > 99.9 wt. % pure, determined by EPMA at multiple spots).

To minimize the evaporation and oxidation during the experiment, phase diagram experiment with sealed capsules can be a good option, and several phase diagram experiments have been carried out in our research group previously. In the present study, iron capsules are employed for the Mg-Ca-Nd alloys to minimize oxidation and evaporation. Besides the moderate strength under high temperature as well as its availability, Fe was chosen as the capsule material due to its very limited reactivity with the involved elements, especially for the case of Mg and Ca, with which no compound is present, and the solid solubility remains at minimal levels.

The capsules are made from iron tubes that were pinched together on the ends with the starting materials loaded and filled with argon, then sealed hermetically by welding both ends using a PUK U4 micro-welder (Lampert, Germany) (Fig. 14). The welding quality, as well as the overall integrity of the capsules, was carefully examined under the stereomicroscope, which was equipped alongside the micro-welder.

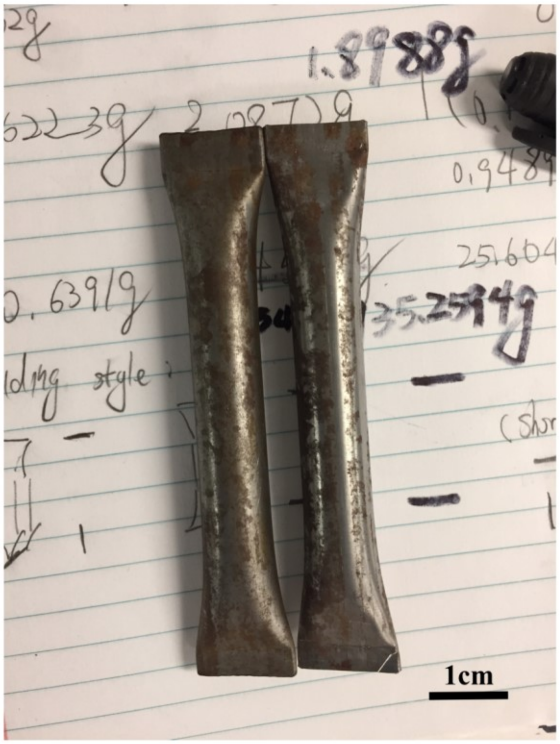

Figure 14, Iron capsules used in the present experiments

Melting and homogenization of the alloys in Fe capsules were achieved using an ST-1700C box furnace (Sentro Tech, USA; inner dimensions: 10 cm × 10 cm × 20 cm), equipped with MoSi2 heating elements. The capsules were loaded into the furnace on alumina foams and in vertical positions, kept at 800 ºC or 900 ºC according to the composition for a duration of 2.5 hours in order to melt the samples, and then water-quenched. This melting ensured the homogenization of starting samples. Initial attempts also involved turning over the capsules every 45 minutes to facilitate homogenization, but the idea was later dropped due to the tendency to introduce flaws such as bubbles and unmelted starting materials, which likely resulted from the sudden drop in temperature while performing this procedure.

Using this method, samples for all 5 designed compositions were successfully prepared. Compositions of the sample alloys are illustrated in Fig. 15 and detailed in Table 6.

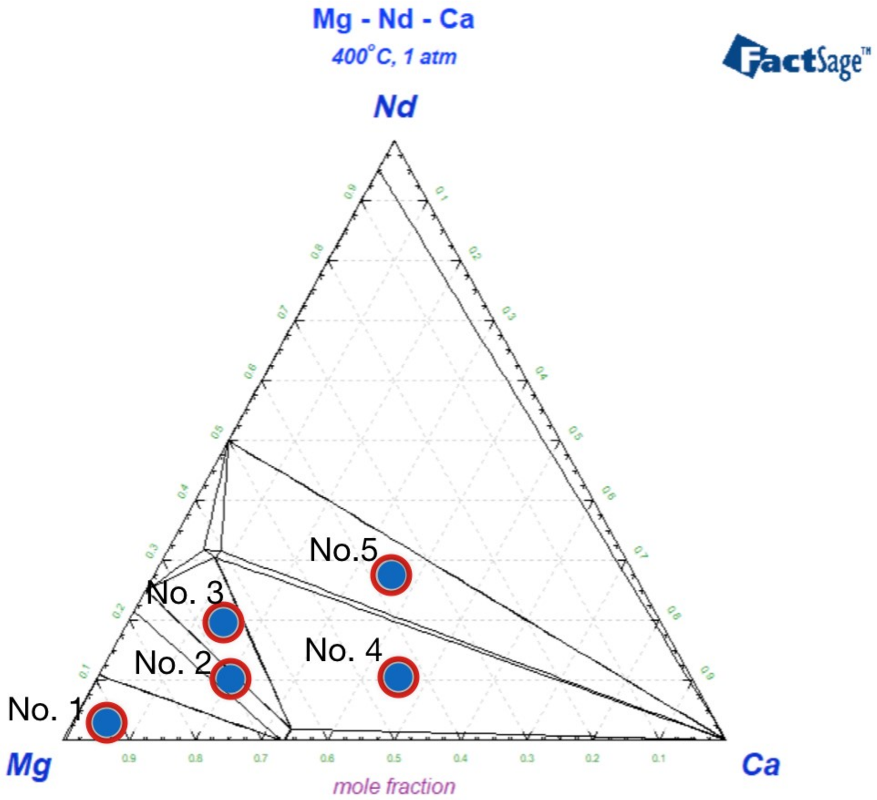

Figure 15, Compositions of the sample alloys projected on the phase diagram at 400 ^{o}C calculated from FTLite database

Table 6, Designed alloy compositions for the samples in mole fraction

Sample No.	x(Mg)	x(Ca)	x(Nd)
1	0.9110	0.060	0.0290
2	0.7000	0.2000	0.1000
3	0.6716	0.1368	0.1916
4	0.4215	0.4702	0.1083
5	0.3680	0.3603	0.2717

Homogeneity of the sample alloys is verified using a Hitachi SU-3500 SEM-EDS to be consistent with the designed composition within a tolerance of 1-3 at. %. Table 7 shows the analytical results from the first batch of homogenized samples, which are of slightly different design in the vicinity of composition No. 2 and No. 3. Compositional designs are later rectified in line with Table 6, with consistent levels of homogeneity.

Table 7, EDS verification of alloy homogeneity in mole %

	Designed	Measured	Designed	Measured
% Mg	67.1	66.6-67.0	75.0	76.8-77.5
% Ca	19.2	19.9-20.5	20.1	18.2-18.9
% Nd	13.7	12.5-13.2	4.9	4.3-4.5

4.2 CHARACTERIZATION OF SAMPLES

In order to investigate the phase diagram of the Mg-Ca-Nd ternary system, two different approaches were employed as shown in Fig. 16: equilibration/quenching technique and thermal analysis technique.

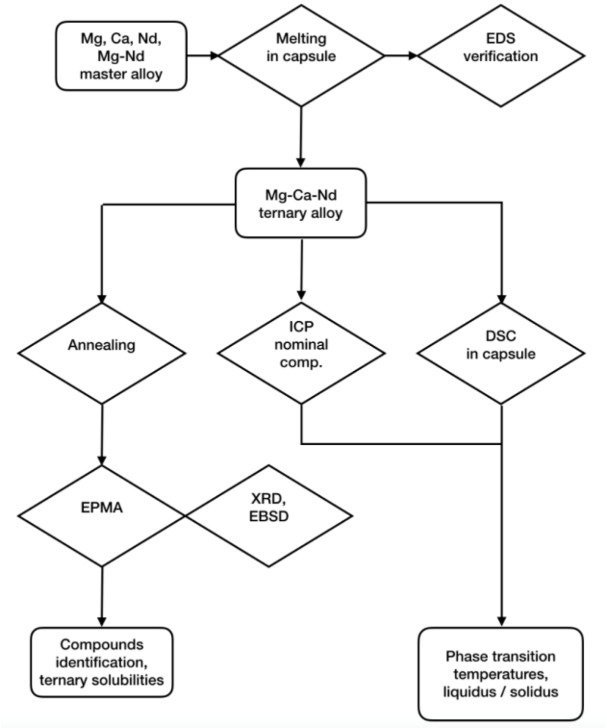

Figure 16, Proposed strategy for investigating the phase diagram of the Mg-Ca-Nd system

For the equilibration and quenching approach, alloy samples were equilibrated at 450 ºC in Fe capsules and quenched into water. Then, equilibrated samples were polished for the EPMA and XRD analysis. Unfortunately, despite heavy investments into preparing over 10 equilibrated samples for the Mg-Ca-Nd system, the sensitivity of the samples to air or moisture severely hampered the efforts, especially in the process of grinding and polishing the EPMA samples. Various lubricants were attempted, ranging from deionized water, denatured ethanol, pure ethanol, cyclohexane, mineral oil as well as DP-Lubricant Brown from Struers, along with various techniques to minimize exposure time. None has succeeded in producing the level of surface quality sufficient for EPMA analysis. This could be attributed to the significantly higher Ca and Nd content in the majority of the present alloy samples, compared to the alloys by Fei et al. [40] Therefore, no phase diagram data were obtained from equilibration and quenching experiments.

To overcome the problem of volatility and oxidation of alloy samples, a new type of Fe capsule has been successfully developed (see Fig. 17) for DSC experiments. Fabrication of the capsule involves welding both ends of a section from a small-diameter iron tube, forming cylindrical confinement for 100-200 mg of tightly packed sample alloy. The capsules fit nicely into alumina crucibles. The flat bottom of sealed Fe capsule offers a large contact area, providing ample thermal conductivity to ensure reliable measurements.

Figure 17, Cylindrical Fe capsules containing alloy samples for DSC analysis

Capsules containing samples with all 5 compositions listed in Table 8 were successfully analyzed using a Jupiter STA 449 F3 thermal analyzer (NETZSCH Instruments, Germany) under its DSC-TG configuration. Calibration on the sensitivity and temperature reading of the instrument-sample holder-crucible combination was conducted prior to the analysis, referencing the melting point or polymorphic transition temperatures, as well as enthalpy of transition, of the following standards: biphenyl ($C_{12}H_{10}$), benzoic acid ($C_7H_6O_2$), rubidium nitride ($RbNO_3$), potassium perchlorate ($KClO_4$), cesium chloride (CsCl), potassium chromate (K_2CrO_4), barium carbonate ($BaCO_3$), and diopside ($CaMgSi_2O_6$).

The analysis protocol involves a total of 5 heating sessions and 4 cooling sessions to ensure consistent results. Samples were heated from room temperature to 750 ºC and cooled to 100 ºC for each cycle at 10 K/min heating and cooling rate. The analysis ended after reaching the 750 ºC target in the fifth heating session. Throughout the analysis, a constant flow of argon gas at a rate of 20 mL/min ensures a protective environment. Correction runs were performed on empty Fe capsules in order to cancel out the heat signal generated by the capsule materials.

DSC results for five samples and blank Fe crucible are summarized in Table 9 and the DSC curves are presented in Figs. 18 to 22. Y-axis for the figures represents the DSC signal (µV/mg) in relative scale.

Table 8, Designed compositions of DSC samples in mole fraction. Actual compositions are within 1-3 at. % error range

Sample No.	x(Mg)	x(Ca)	x(Nd)
1	0.9110	0.060	0.0290
2	0.7000	0.2000	0.1000
3	0.6716	0.1368	0.1916
4	0.4215	0.4702	0.1083
5	0.3680	0.3603	0.2717

Table 9, Summary of the DSC results in the present study

Sample	Type	Average / °C	Min. / °C	Max. / °C
Empty Fe capsule	Heating	576.0	574.8	577.7
1	Heating	507.3, 530.7	505.3, 526.6	508.7, 532.8
	Cooling	508.9, 520.6	508.7, 519.2	509.1, 523.0
2	Heating	546.7, 708.1	542.6, 703.8	549.0, 712.1
	Cooling	518.2, 549.1, 718.7	512.1, 541.3, 717.7	524.6, 554.3, 719.4
3	Heating	735.0	733.9	736.1
4	Heating	466.5	464.6	468.1
	Cooling	463.8	463.6	463.9
5	Heating	454.3	452.0	460.8
	Cooling	455.1	454.8	455.5

Results of the blank sample (Fe crucible) is given in Fig. 18. The curves from the individual heating or cooling cycles were presented from bottom to top. The y-axes were presented in relative scales. As can be seen, an exothermic transition occurs at about 576 ºC in the heating curves, but no such transition is recorded in the cooling curves. Trindade et al. [41] have studied the high-temperature oxidation behavior of pure Fe and 2.25Cr1Mo low-alloy steel at 550 ºC, confirming that significant oxidation could occur at similar temperatures, typically around 500-600 ºC for pure iron or common low-alloy steels. In the current DSC measurements, traces of oxygen still exist as a result of the imperfect sealing, and the Fe capsules were indeed slightly oxidized after undergoing 5 heating cycles. Furthermore, Trindade et al. [41] have also observed that the kinetics of the exothermic oxidation process greatly accelerates upon thermal cycling. The phenomenon was attributed to the cracking of the oxide scales during cooling, which permits better access of oxygen to the iron substrate during subsequent heating cycles. This also concurs with the increase in the exothermic peak area for the later heating cycles. In the calibration, this peak by Fe crucible was removed for the DSC analysis of alloy samples.

As can be seen in Figs. 19 to 23, there have been a few occurrences of small irregular peaks in the DSC curves, and are ignored in the present DSC analysis. According to a dedicated technical guideline by Thomas at TA Instruments, [42] a number of factors might have contributed to the irregular peaks. First of all, the release of residual stress during the recovery process might have resulted in unexpected endothermic transitions, while the recrystallization process could have contributed to minor exothermic peaks. Because the sample alloys were quenched after homogenization, the accumulation of thermal stress, as well as the formation of columnar grains were to be expected. This could be compounded by other experimental phenomena, such as the release or absorption of the minute amount of oxygen and other gas molecules that were chemically bonded or physically attached to the sample surface. It is also noteworthy that the cancellation of the thermal signals generated by the Fe crucibles might be affected by under or overcompensation, as the complex thermal impact from the crucibles, each varying slightly in the surface area and the degree of oxidation from welding, could not be perfectly represented by extrapolations based on the empty Fe crucible.

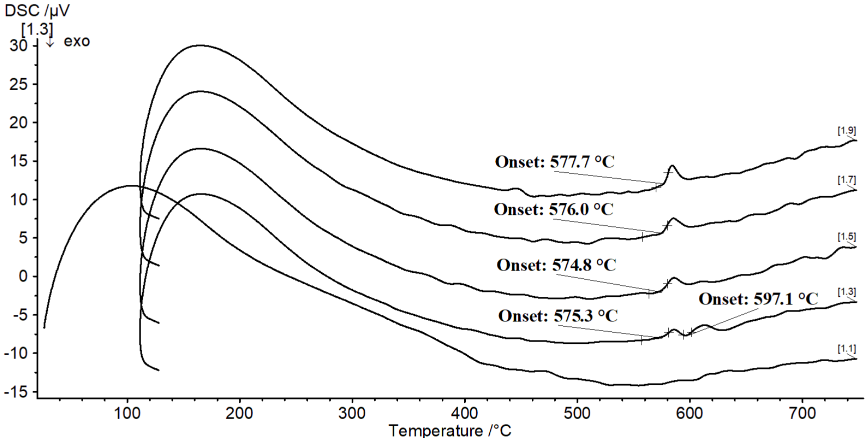

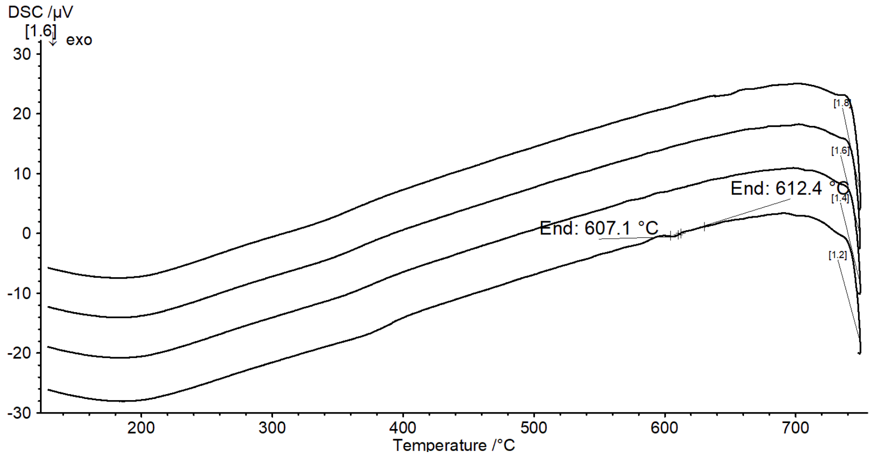

Figure 18, DSC curves of an empty Fe capsule (heating and cooling curves)

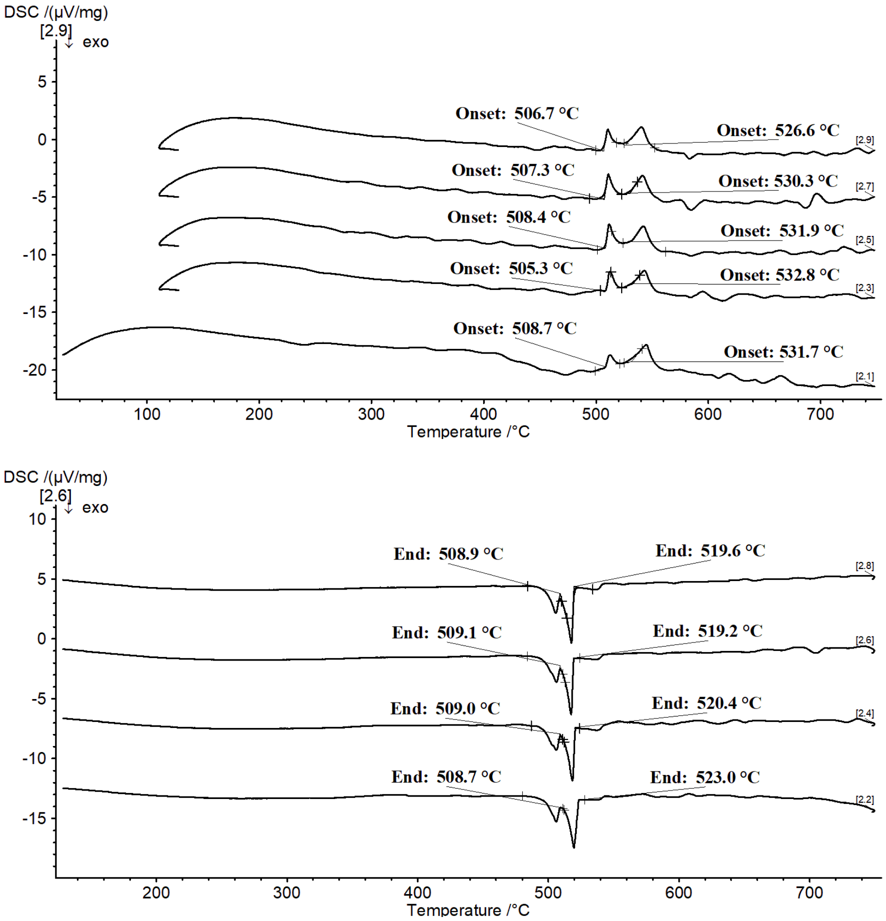

Figure 19, DSC curves of sample No. 1 (heating and cooling curves)

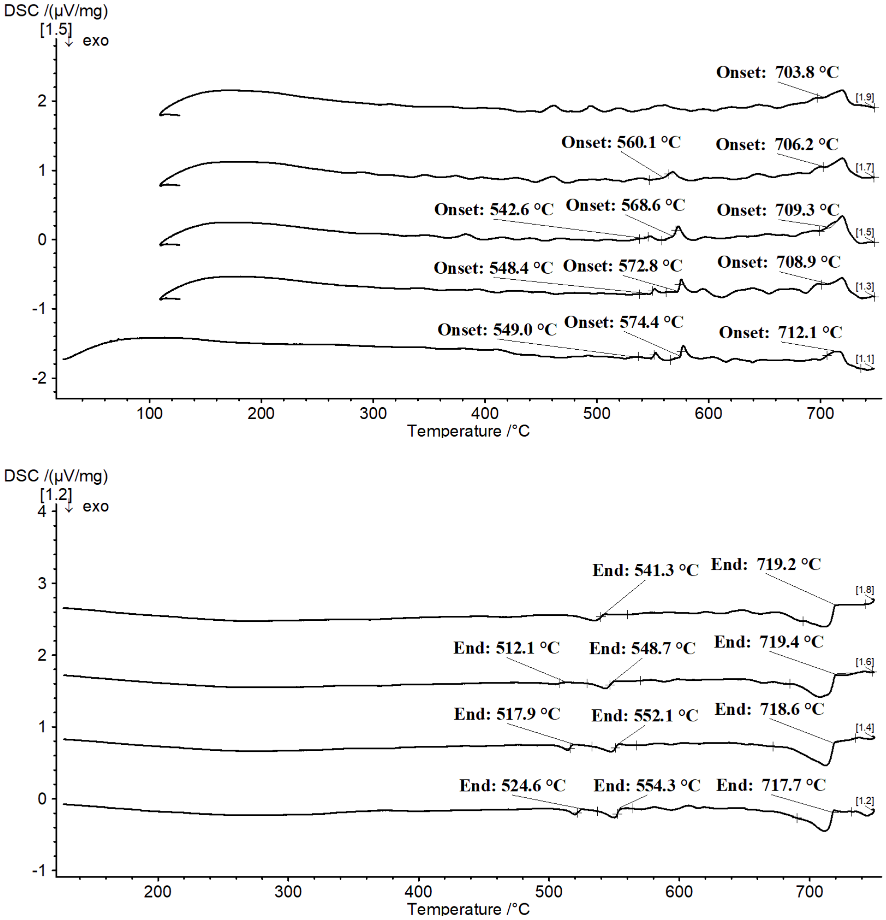

Figure 20, DSC curves of sample No. 2 (heating and cooling curves)

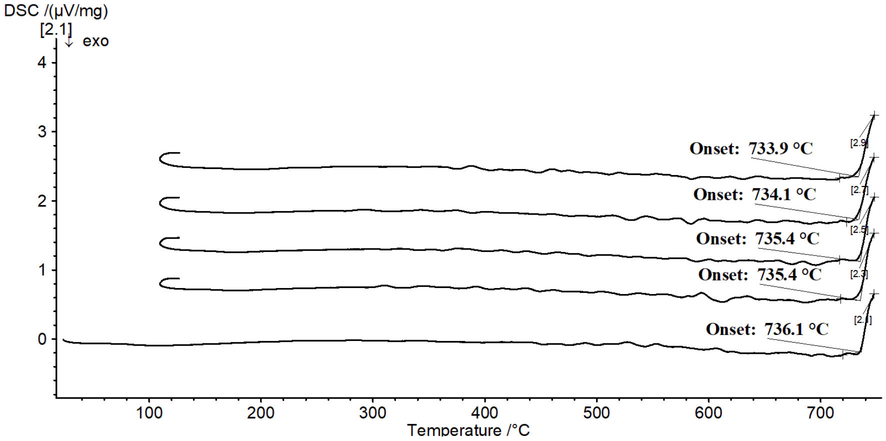

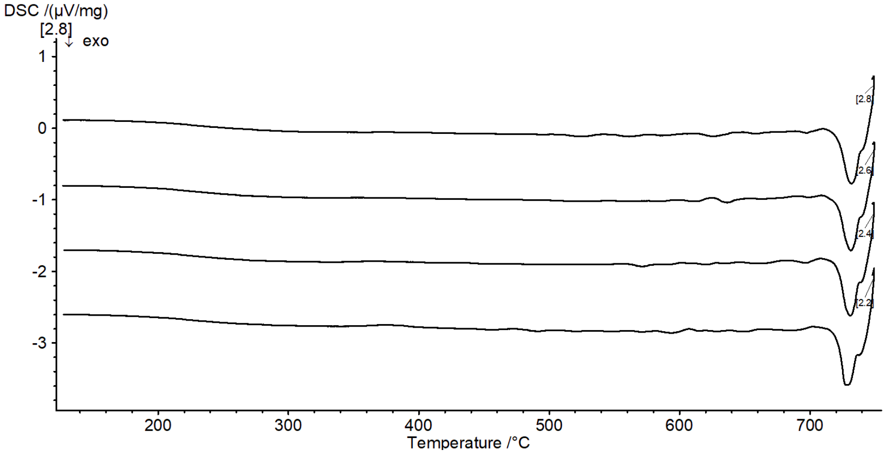

Figure 21, DSC curves of sample No. 3 (heating and cooling curves)

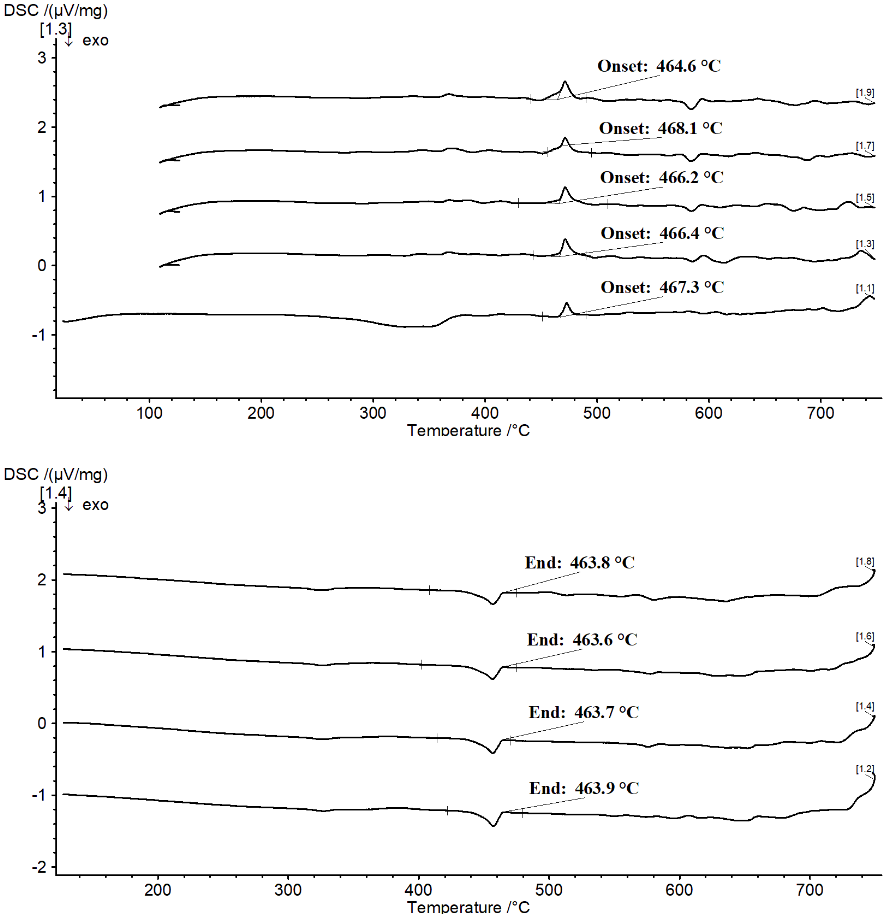

Figure 22, DSC curves of sample No. 4 (heating and cooling curves)

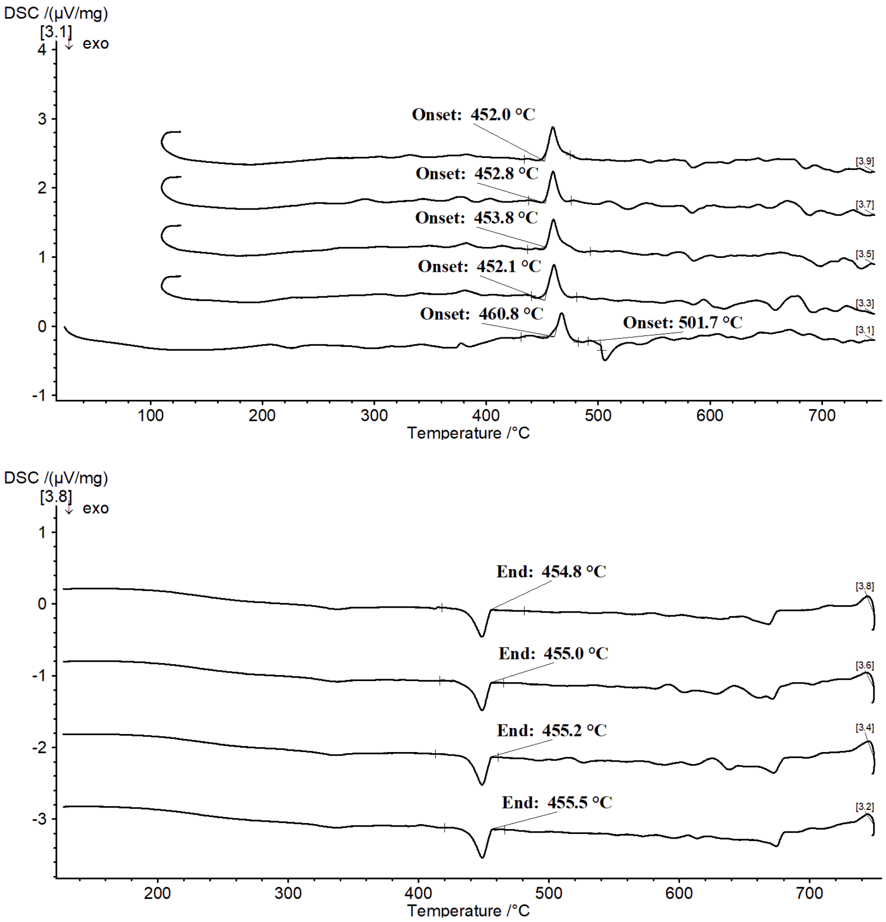

Figure 23, DSC curves of sample No. 5 (heating and cooling curves)

After the DSC experiments, Fe capsules were cut and the samples were observed under SEM. As can be seen in Fig. 24, for example, the samples are in good contact with Fe crucible and no severe evaporation or oxidation of alloys inside Fe capsule was found. So, it can be said that the signals detected in the DSC experiments are reliable.

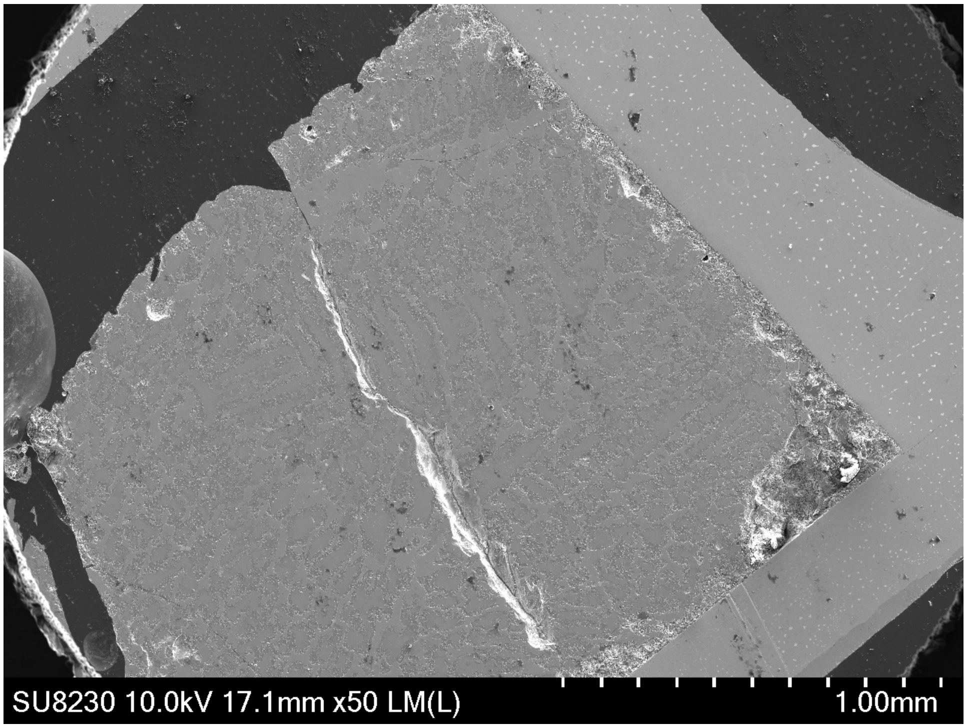

Figure 24, SEM image of a DSC capsule after analysis (Sample No. 1)

5 RESULTS AND DISCUSSIONS

5.1 OPTIMIZATION OF THE CA-ND SYSTEM

As reviewed in section 3.1, there is very limited amount of experimental data in the Ca-Nd system. The present thermodynamic optimization was based on the phase diagram of the Ca-Nd system proposed by Gschneidner and Calderwood [16] who built the diagram mainly using the data of Stroganova et al. [15] Stroganova et al. obtained the phase diagram information using differential thermal analysis (DTA) and metallographic methods. The optimized phase diagram in the present study is calculated in Fig. 25.

It should be noted that the liquidus of the system in the Ca-rich region is still undetermined and the shape of the miscibility gap is unknown. A rather simple set of MQM parameters were used for the liquid solution to construct the miscibility gap in the Ca-rich side. As no short-range ordering is found in this binary solution, the coordination numbers of species for the MQM model were all set to the default value, 6. That is, $Z_{Ca,Nd}^{Ca} = Z_{Ca,Nd}^{Nd} = Z_{Ca,Ca}^{Ca} = Z_{Nd,Nd}^{Nd} = 6$. The solubility of Ca in BCC and DHCP Nd is noticeable. On the other hand, the solubility of Nd in FCC and BCC Ca is negligible. In order to reproduce these solubility limits, the parameters for the solid solutions were optimized with CEF. All the optimized parameters are summarized in Table 10. All the phase diagram experimental data by Stroganova et al. [15] are well reproduced. The most noticeable difference between the present optimized diagram and the previous diagram by Gschneidner and Calderwood [16] is the eutectoid reaction of BCC (Nd-rich) → FCC (Ca-rich) + DHCP (Nd-rich), which was reported at 429ºC. Reproducing the drastic impact of Ca on the β ↔ α transformation temperature of Nd appears to necessitate the use of model parameters beyond reasonable limits. Considering that the accurate determination of phase equilibria at such low temperatures can also be challenging due to the slow kinetics, the feature is omitted in favor of the current optimization.

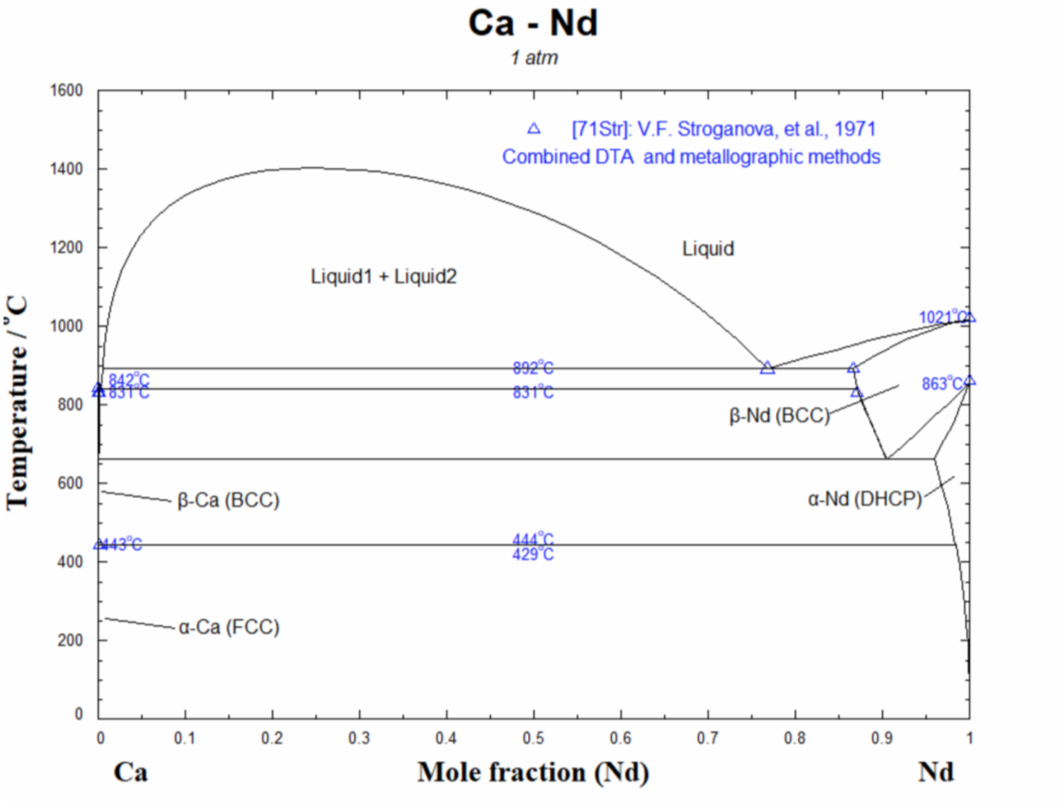

Figure 25, Optimized phase diagram for the Ca-Nd system in the present study

5.2 OPTIMIZATION OF THE CA-Y SYSTEM

The optimization of the Ca-Y system was based primarily on the experimental data by Stroganova et al. [18] using DTA, XRD and other physico-chemical approaches, combined with the re-assessed diagram by Dzhuraev et al. [21] through systematic calculations. The Ca-Y phase diagram calculated in the present study is presented in Fig. 26.

The monotectic reaction, L_1 (~77 mol % Y) → L_2 (~10 mol % Y) + β-Y (BCC) (~99.8 mol % Y) at 1180 ºC is reported by Stroganova et al. [18] Therefore, in the present study, the liquid MQM parameters were determined in order to reproduce the liquid miscibility gap. The coordination numbers for the MQM model were set to $Z^{Ca}_{Ca,Y} = Z^{Y}_{Ca,Y} = Z^{Ca}_{Ca,Ca} = Z^{Y}_{Y,Y} = 6$. The parameters for solid solutions, HCP, BCC and FCC, were determined to reproduce the limited solubility. The optimized parameters are listed in Table 10.

It should be noted that the present phase diagram differs from the previous diagram from Predel [22] in the solubility of Ca in HCP Y-rich solid solution, which is stated to reach 5.25 mol % Ca, or 2.44 wt. % Ca, based on the calculations by Dzhuraev et al. [21] This, however, was not substantiated by the experimental work of Stroganova et al., [18] which involved repeated DTA analysis on the Y-rich side beyond 1200ºC, as well as other physico-chemical analysis on multiple Y-rich compositions that would likely reveal such levels of solid solubility. Furthermore, Stroganova et al. [18] have stated specifically that "the solubility of the elements in each other at a eutectic temperature of 825 °C (1098 K) is negligible", in stark contrast to the diagram proposed by Predel. [22]

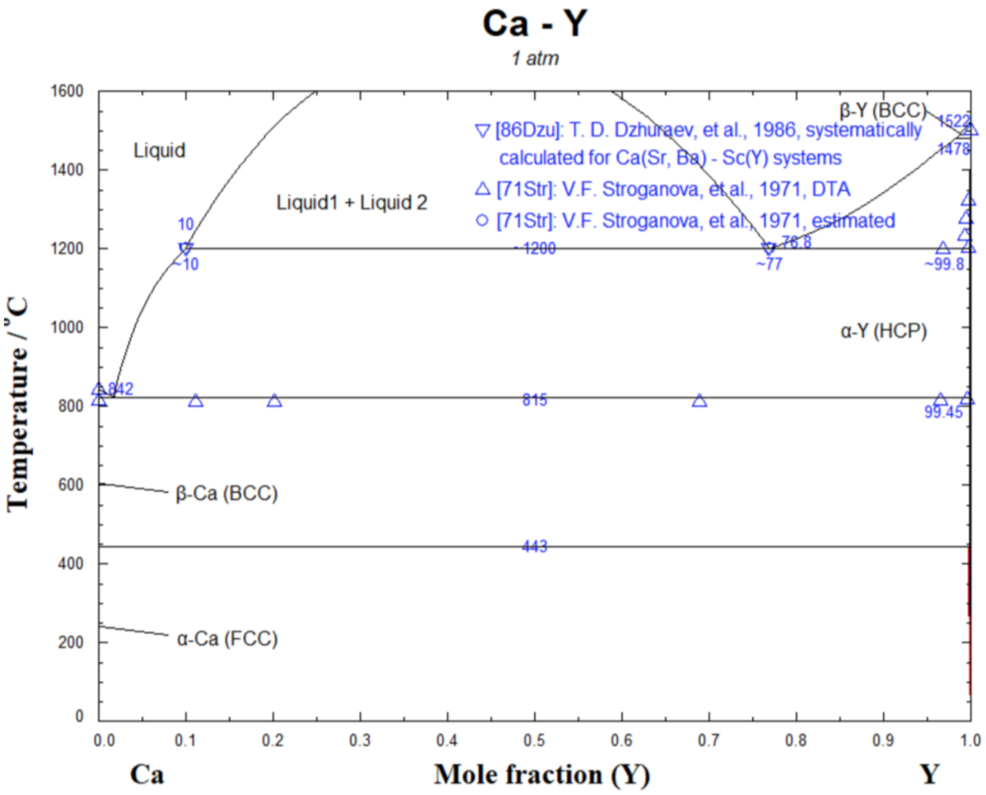

Figure 26, Optimized phase diagram for the Ca-Y system in the present study

5.3 Optimization of the Ca-Ce System

The experimental phase diagram data in the Ca-Ce system are only limited to the liquid miscibility gap by Zverev. [21] In the present thermodynamic optimization, the MQM parameters for the liquid solution were determined to reproduce the miscibility gap. The coordination numbers for the MQM model were set to $Z^{Ca}_{Ca,Ce} = Z^{Ce}_{Ca,Ce} = Z^{Ca}_{Ca,Ca} = Z^{Ce}_{Ce,Ce} = 6$. No solid solubility data were reported in solid states. But considering the similarity with other Ca-RE systems, the very limited mutual solubility can be assumed. The Ca-Y phase diagram calculated in the present study is presented in Fig. 27.

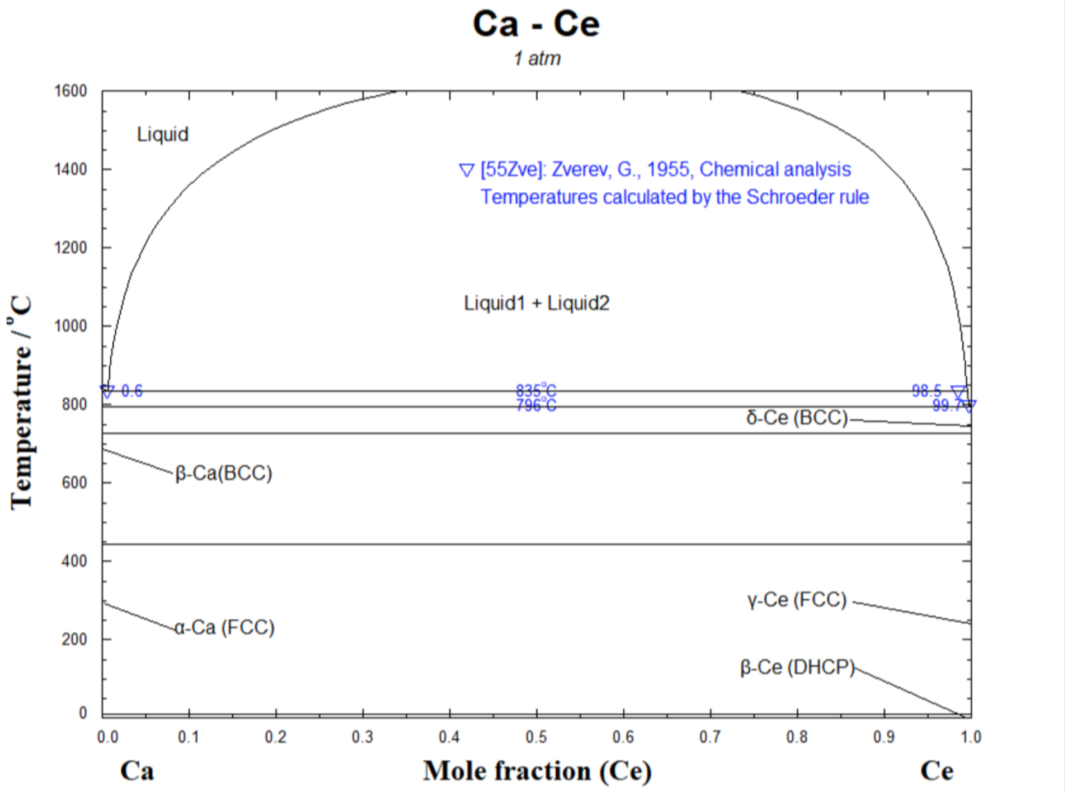

Figure 27, Optimized phase diagram for the Ca-Ce system in the present study

Table 10, Optimized thermodynamic model parameters of the Ca-RE (RE = Nd, Y, Ce) systems

Phase name	Model	Parameters (J / mole atoms)
Ca-Nd liquid	MQM	Δg_{CaNd} = 7178 + (19665-8.37 T) x_{CaCa} – 962 x_{NdNd}
Ca-Y liquid	MQM	Δg_{CaY} = 13841 – 2807 x_{CaCa} – 7791 x_{YY}
Ca-Ce liquid	MQM	Δg_{CaCe} = 20751 – 4.18 T + 962 x_{CeCe}
Ca-Nd HCP	CEF	$L^0_{Ca,Nd}$ = 16736
Ca-Y HCP	CEF	$L^0_{Ca,Y}$ = 8996 + 41.84 T
Ca-Ce HCP	CEF	$L^0_{Ca,Ce}$ = 16736
Ca-Nd BCC	CEF	$L^0_{Ca,Nd}$ = 28870 + 4.18 T
		$L^1_{Ca,Nd}$ = -19246
		$L^2_{Ca,Nd}$ = 4184
Ca-Y BCC	CEF	$L^0_{Ca,Y}$ = 83680
Ca-Ce BCC	CEF	$L^0_{Ca,Ce}$ = 83680
Ca-Nd DHCP	CEF	$G^{\text{o}}_{Ca(DHCP)} = G^{\text{o}}_{Ca(HCP)}$ + 2092; $L^0_{Ca,Nd}$ = 19288 + 4.18 T
Ca-Nd FCC	CEF	$L^0_{Ca,Nd}$ = 62760
Ca-Y FCC	CEF	$L^0_{Ca,Y}$ = 50208
Ca-Ce FCC	CEF	$L^0_{Ca,Ce}$ = 75312

5.4 OPTIMIZATION OF THE MG-CA-ND TERNARY SYSTEM

The thermodynamic descriptions of the binary Mg-Nd and Mg-Ca systems were taken from the previous studies by Kang et al. [43] and Wang [44], respectively. It should be noted that the same model parameters are stored in the FTlite database in FactSage 7.2. As the thermodynamic database do accurately describe all available and reliable thermodynamic properties and phase diagram data of these two systems, the previous thermodynamic descriptions were taken without any modification. The phase diagrams of Mg-Nd and Mg-Ca system calculated from the previous database are presented in Fig. 28 and Fig. 29.

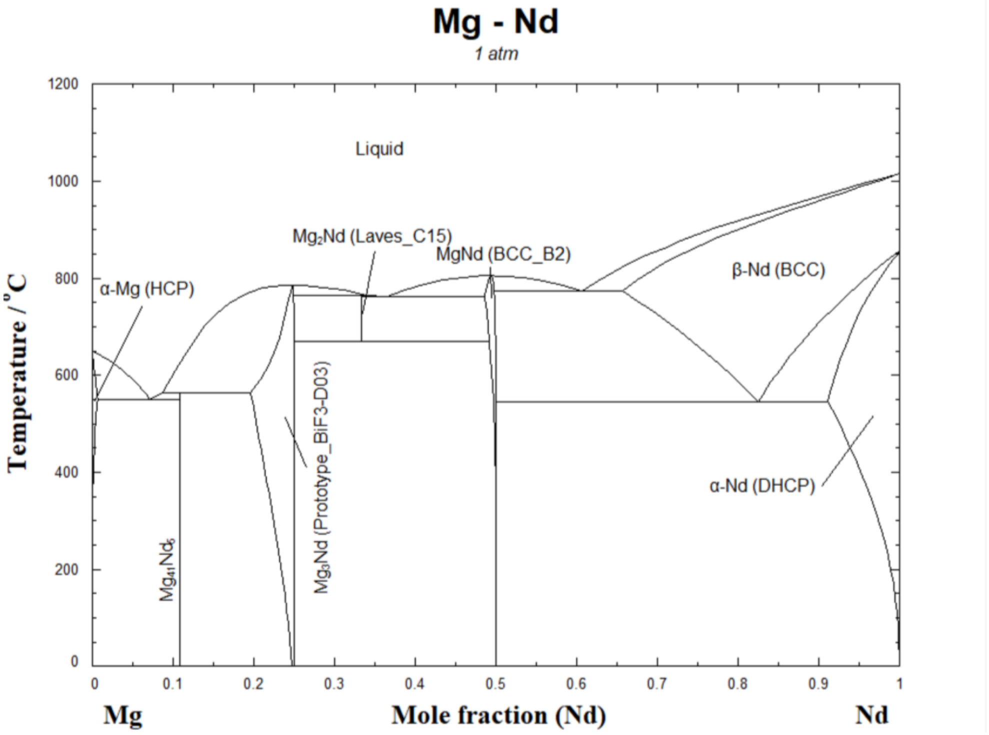

Figure 28, Phase diagram for the Mg-Nd system based on optimizations by Kang et al. [43]

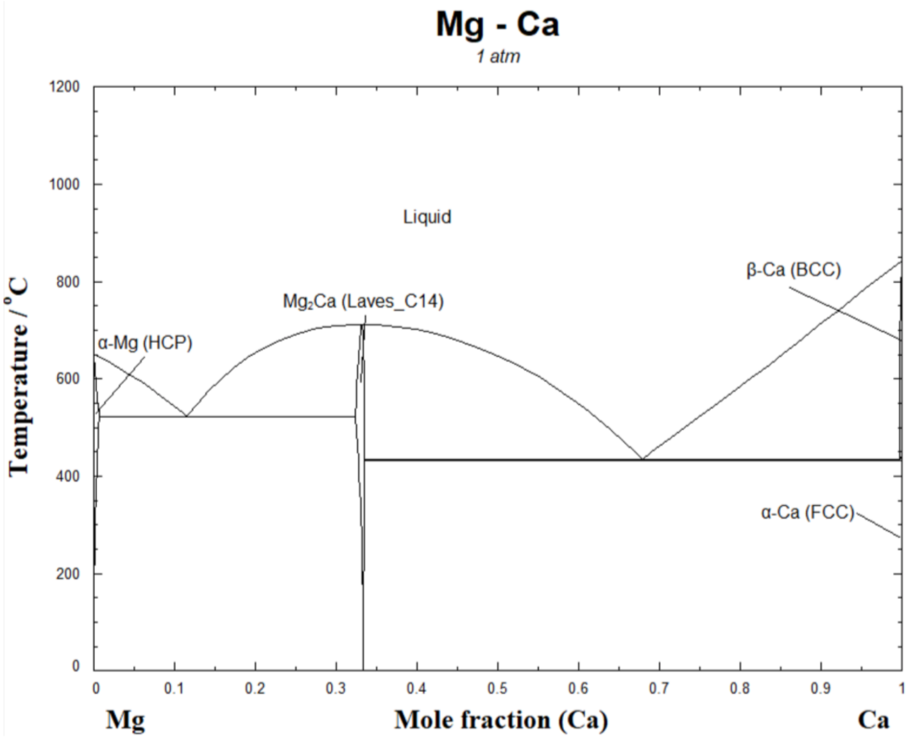

Figure 29, Phase diagram for the Mg-Ca system based on optimizations by Wang [44]

The experimental data by Fei et al. [40] and the present experimental data were used in the optimization for the ternary Mg-Ca-Nd system. No thermodynamic properties data are available in the ternary system. It should be also noted that no ternary compound in the ternary system was reported. In the optimization, previous optimization results of the Mg-Nd and Mg-Ca systems, and the present Ca-Nd optimization results were first combined to produce the preliminary prediction of the ternary Mg-Ca-Nd system. Additional model parameters were then introduced to reproduce the ternary phase diagram experimental data. The optimized model parameters for liquid and solid solutions are listed in Table 11.

As can be seen in Fig. 30, Fei et al. [40] reported the ternary solubility of Ca in the compound $Mg_{41}Nd_5$, and Nd in the compound Mg_2Ca. In order to describe these ternary solid solutions, the structures of solid solutions were assumed to be $Mg_{41}(Nd, Ca)_5$, and $(Mg, Ca, Nd)_2(Mg, Ca, Nd)$ (Laves C14 phase), respectively, and CEF was used to describe their Gibbs energies. As the ternary solubilities (3.57 at. % Ca in $Mg_{41}Nd_5$, and 1.24 at. % Nd in Mg_2Ca at 400 ºC) in the solutions are very small, the Gibbs energies of pseudo end-members, $Mg_{41}Ca_5$, and Mg_2Nd, were optimized to reproduce the phase diagram information in this system without any excess interaction parameters. As can be seen in Fig. 30, the reported solubilities are well reproduced.

The Gibbs energy of ternary Mg-Ca-Nd solution was calculated from three constituent binary solutions using the Toop interpolation technique with Mg as an asymmetric component. [45] This choice of the interpolation technique is based on the fact that the enthalpies of mixing for the Mg-Ca and Mg-Nd liquid solutions are significantly negative, while the enthalpy of mixing for the Ca-Nd system is very positive. In this kind of asymmetric liquid solution, it is well known that the Toop interpolation technique can offer a better prediction for the Gibbs energy of the ternary solution. In order to improve the accuracy of the liquidus of the ternary system, one small positive ternary model parameter was also introduced in the final optimization.

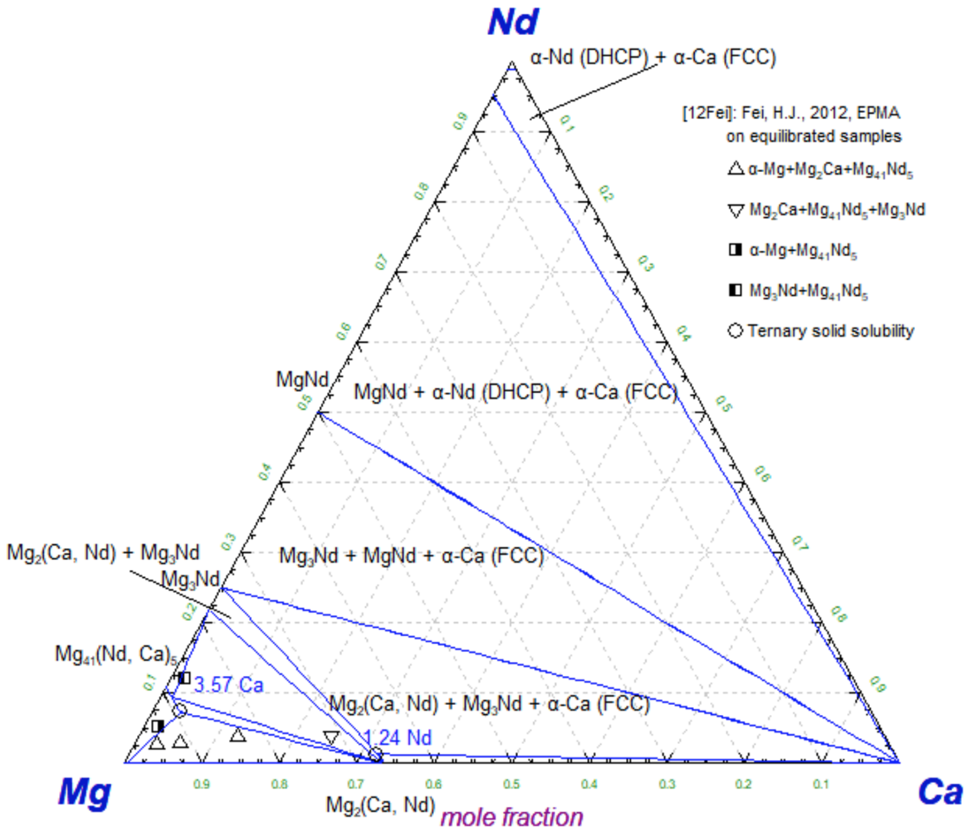

Figure 30, Optimized phase diagram for the Mg-Ca-Nd ternary system at 400 ºC along with the experimental data by Fei et al. [40]

Table 11, Optimized thermodynamic model parameters of the Mg-Ca-Nd ternary system

Phase name	Model	Parameters / (J / mole atoms)
Mg-Ca-Nd liquid	MQM	Δg_{CaNd} = 7178 + (19665-8.37 T) x_{CaCa} – 962 x_{NdNd}
		Δg_{MgCa} = -9916 + 6.50 T + (-3054+0.40 T) x_{MgMg} + (3661-4.60 T) x_{CaCa} – 0.60 T x_{CaCa}^2
		Δg_{MgNd} = -15899 + 7.43 T + (-9623+2.51 T) x_{MgMg} – 8368 x_{NdNd}
		Ternary parameter $q_{Ca,Nd,(Mg)}^{001}$ = 13807
$Mg_{41}Ca_5$	$Mg_{41}(Nd, Ca)_5$, CEF	$G_{Mg:Ca}^{\circ,Mg41Ca5}$ = (41 $G_{Mg(HCP)}^{\circ}$ + 5 $G_{Ca(FCC)}^{\circ}$)/46 – 3039 + 0.88 T
		$G_{Mg:Nd}^{\circ,Mg41Nd5}$ = (41 $G_{Mg(HCP)}^{\circ}$ + 5 $G_{Nd(DHCP)}^{\circ}$)/46 – 8186 + 2.51 T
Mg_2(Nd, Ca) (Laves C14)	(Mg, Ca, Nd)$_2$ (Mg, Ca, Nd), CEF	$G_{Mg:Nd}^{\circ,Mg2Nd}$ = (2 $G_{Mg(HCP)}^{\circ}$ + $G_{Nd(DHCP)}^{\circ}$)/3 – 11314 + 5.30 T
		$G_{Mg:Mg}^{\circ,Mg2Mg}$ = $G_{Mg(HCP)}^{\circ}$ + 7791
		$G_{Nd:Mg}^{\circ,Nd2Mg}$ = (2 $G_{Nd(DHCP)}^{\circ}$ + $G_{Mg(HCP)}^{\circ}$)/3 + 13947
		$G_{Nd:Nd}^{\circ,Nd2Nd}$ = $G_{Nd(DHCP)}^{\circ}$ + 62760
		$G_{Mg:Ca}^{\circ,Mg2Ca}$ = -11333 + 32.92 T
		$G_{Ca:Mg}^{\circ,Ca2Mg}$ = (2 $G_{Ca(FCC)}^{\circ}$ + $G_{Mg(HCP)}^{\circ}$)/3 + 26855
		$G_{Ca:Ca}^{\circ,Ca2Ca}$ = $G_{Ca(FCC)}^{\circ}$ + 8177 + 20.92 T
		$G_{Nd:Ca}^{\circ,Nd2Ca}$ = (2 $G_{Nd(DHCP)}^{\circ}$ + $G_{Ca(FCC)}^{\circ}$)/3 + 139467
		$G_{Ca:Nd}^{\circ,Ca2Nd}$ = (2 $G_{Ca(FCC)}^{\circ}$ + $G_{Nd(DHCP)}^{\circ}$)/3 + 139467

Several isopleths were calculated in Figs. 31-34 from the present study and compared with the present DSC data and results by Fei et al. [40] The calculated results match well with the DSC results for sample No. 1, No. 2 and No. 3 well within ±10 ºC. The DSC analyses on sample No. 4 and No. 5 display slightly larger discrepancy. From thermodynamic calculation results, it is believed that these strong signal at about 455~465ºC seems to correspond to the eutectic reaction, $L \rightarrow$ β-Ca + Mg_3Nd. The calculated results are about 25ºC lower than DSC measurements. It should be also noted that the phase transition reaction cannot be exactly identified in the present experiments because no equilibration/quenching experiments were successfully performed. In general, the phase transitions by the present experiments are well described in the present optimization.

By using the present thermodynamic optimization results, any phase diagram sections and thermodynamic properties can be calculated. For example, liquidus projection is predicted in Fig. 35. As expected from the miscibility gap in the Ca-Nd system, a large ternary miscibility gap is located in the low Mg region. The primary phase regions of α-Mg, Mg_3Nd, and the BCC solid solution with mainly Mg, Nd, and traces of Ca occupy a wide range of area. The liquidus projection in the Mg-rich region is calculated in Fig. 36. From this diagram, the solidification behavior of Mg alloy containing Ca and Nd can be understood. The isothermal phase diagrams at 200, 300, 400, 500, 600, 700 ºC for the Mg-Ca-Nd system are calculated in Fig. 37. The isothermal sections in the Mg-rich region from 200-600 ºC are also predicted in Fig. 38. The calculated phase diagrams could provide insight for designing Mg alloys that simultaneously contain Ca and Nd as alloying elements.

The phase distributions of several Mg-Ca-Nd alloys with temperature can be also calculated using the database built in this study. For example, Mg alloys containing 1 wt.% of (Nd+Ca) can be considered as possible Mg wrought alloy. The phase distributions of the Mg-1wt.%Nd, Mg-0.8wt.%Nd-0.2wt.%Ca, Mg-0.5wt.%Nd-0.5wt.%Ca, Mg-0.2wt.%Nd-0.8wt.%Ca, and Mg-1wt.%Ca alloy with temperature are calculated in Fig. 39. The predicted precipitation phases consist of $Mg_{41}(Nd, Ca)_5$, and Mg_2Ca in the form of Laves C14 phase. At 1 wt.% of (Nd+Ca) content, roughly 2.0-2.5 wt.% of the precipitates would be formed in total during equilibrium cooling. In the case of the Mg-0.5wt.%Nd-0.5wt.%Ca alloy, all Ca and Nd are dissolved into the Mg matrix beyond 410ºC, the lowest among the proposed compositions. This might prove beneficial in the solution treatment process. The gradual formation of precipitates might lead to favorable effects in terms of grain refinement through mechanisms such as the solution drag effects on grain boundaries and dislocations, while the high saturation of Nd in the Mg matrix aligns with the optimal conditions for texture weakening, based on the study by Jung et al. [9] When the content of Ca is increased by replacing Nd, a greater quantity of Mg_2Ca precipitate can be produced. However, due to the high precipitation temperature of Mg_2Ca, it would prove difficult to homogenize the Mg-Ca-Nd alloy, which is less favorable for wrought Mg alloy.

As both Nd and Ca can form stable intermetallic phases in Mg alloy, the Mg-Ca-Nd system can also be considered for cast alloy. For this purpose, Mg alloys containing 3wt.% of (Nd+Ca) are considered as the model alloy in this study. The phase distributions for Mg-3wt.%Nd, Mg-2wt.%Nd-1wt.%Ca, Mg-1.5wt.%Nd-1.5wt.%Ca, Mg-1wt.%Nd-2wt.%Ca alloys in equilibrium cooling are calculated in Fig. 40. $Mg_{41}(Nd, Ca)_5$ and Mg_2Ca remain as the predicted precipitation phases. At the proposed level of 3wt.% of (Nd+Ca), a total of roughly 6.5-7.5 wt.% precipitates are formed during equilibrium cooling, in a manner rather similar to the previous case with 1 wt.% of (Nd+Ca). With a greater level of Nd and Ca, the precipitation phases $Mg_{41}(Nd, Ca)_5$ and Mg_2Ca start to form at higher temperatures. This might create challenges for attempts to fully dissolve the Nd and Ca into the Mg matrix through heat treatment. Nevertheless, the expanded temperature region of their gradual formation, combined with the greater amounts for both precipitates, might further facilitate the desirable effects for grain refinement. Furthermore, the phase distributions for the proposed compositions under the Scheil-Gulliver cooling conditions could also be readily calculated based on the optimized database, offering insights to cooling scenarios with rapid cooling rates which are commonly found among processes such as the die-casting. The precipitation phases found under the Scheil-Gulliver cooling conditions remain identical, while the ultimate amount of precipitates formed decreases slightly. Both precipitates tend to form at higher temperatures, at around 500-550ºC. Due to the basic assumptions of the Scheil-Gulliver cooling, the formation of precipitates is abrupt, rather than the gradual formation observed in the equilibrium cooling scenarios. The actual cooling scenarios usually lie in between the results predicted by equilibrium and Scheil-Gulliver cooling calculations, with greater semblance to equilibrium cooling at lower rates of cooling, and get closer to the Scheil-Gulliver cooling results the higher the cooling rates are.

The calculated phase diagrams and phase distribution results in Figs. 35 to 40 can provide insight for designing Mg alloys that simultaneously contain Ca and Nd as alloying elements.

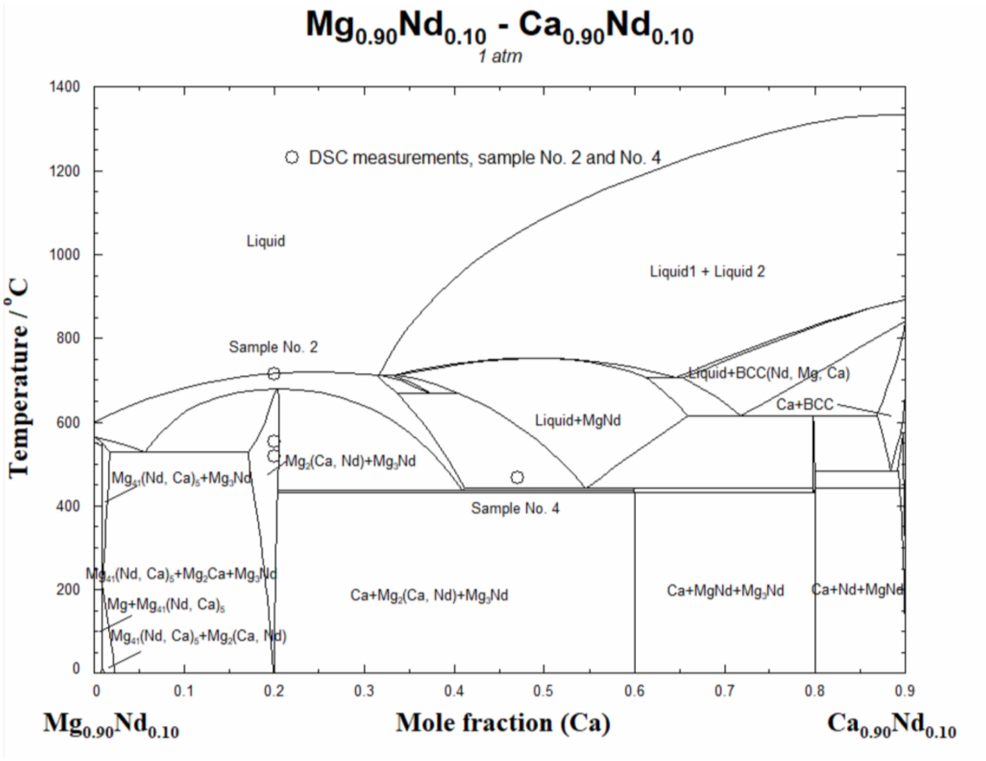

Figure 31, Isopleth of $Mg_{0.90}Nd_{0.10}$-$Ca_{0.90}Nd_{0.10}$ calculated from the present study along with experimental data

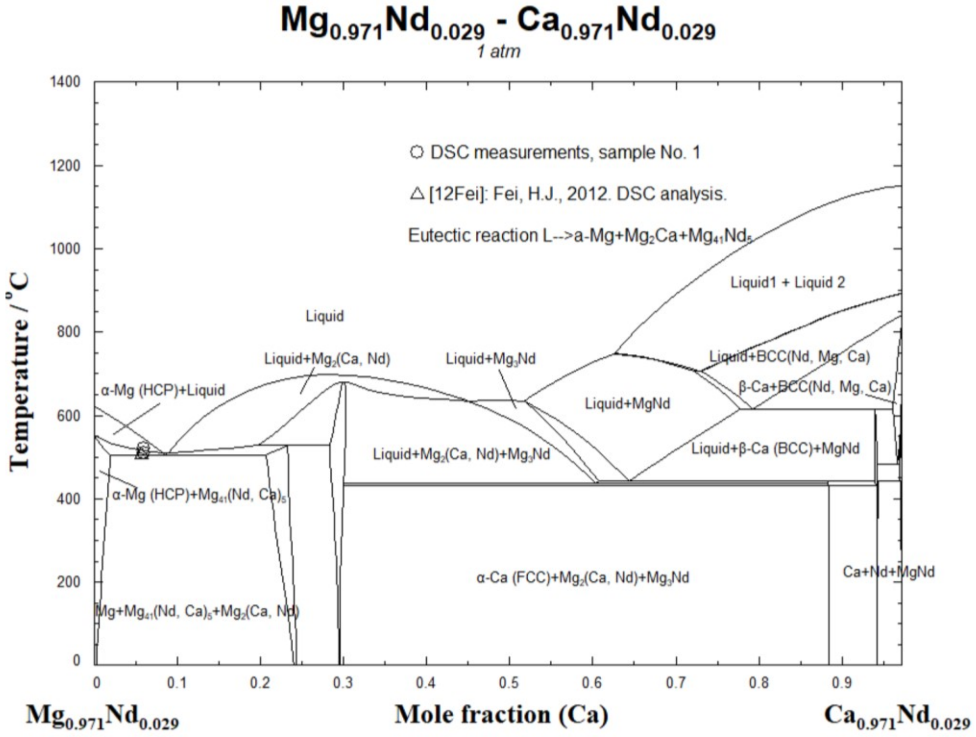

Figure 32, Isopleth of $Mg_{0.971}Nd_{0.029}$-$Ca_{0.971}Nd_{0.029}$ calculated from the present study along with experimental data

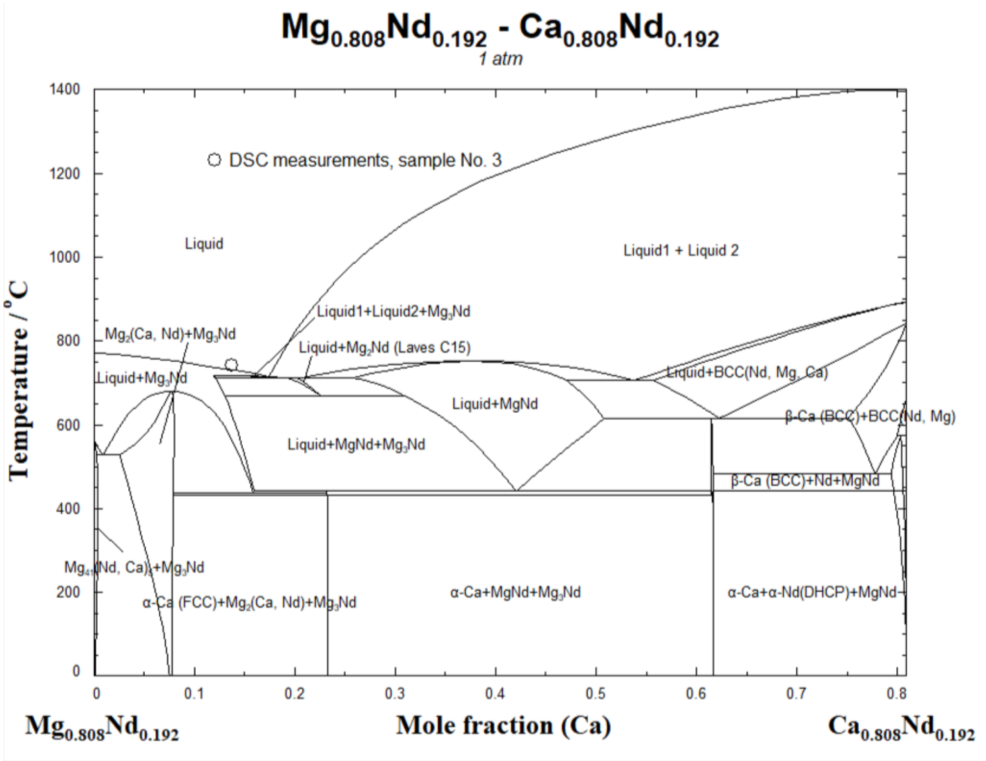

Figure 33, Isopleth of $Mg_{0.808}Nd_{0.192}$-$Ca_{0.808}Nd_{0.192}$ calculated from the present study along with experimental data

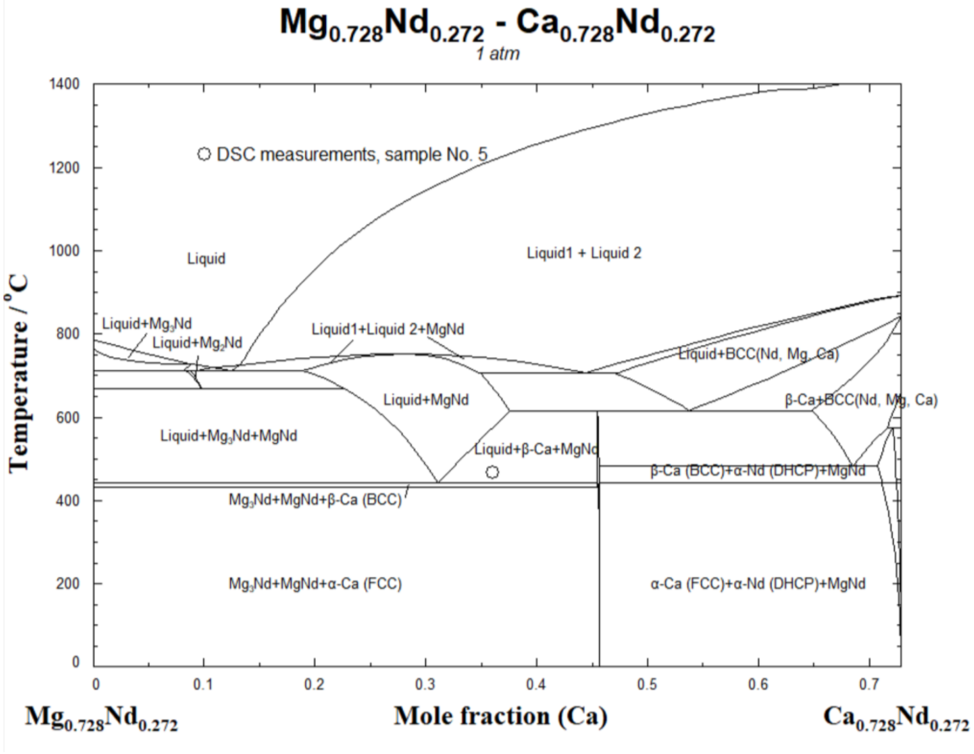

Figure 34, Isopleth of $Mg_{0.728}Nd_{0.272}$-$Ca_{0.728}Nd_{0.272}$ calculated from the present study along with experimental data

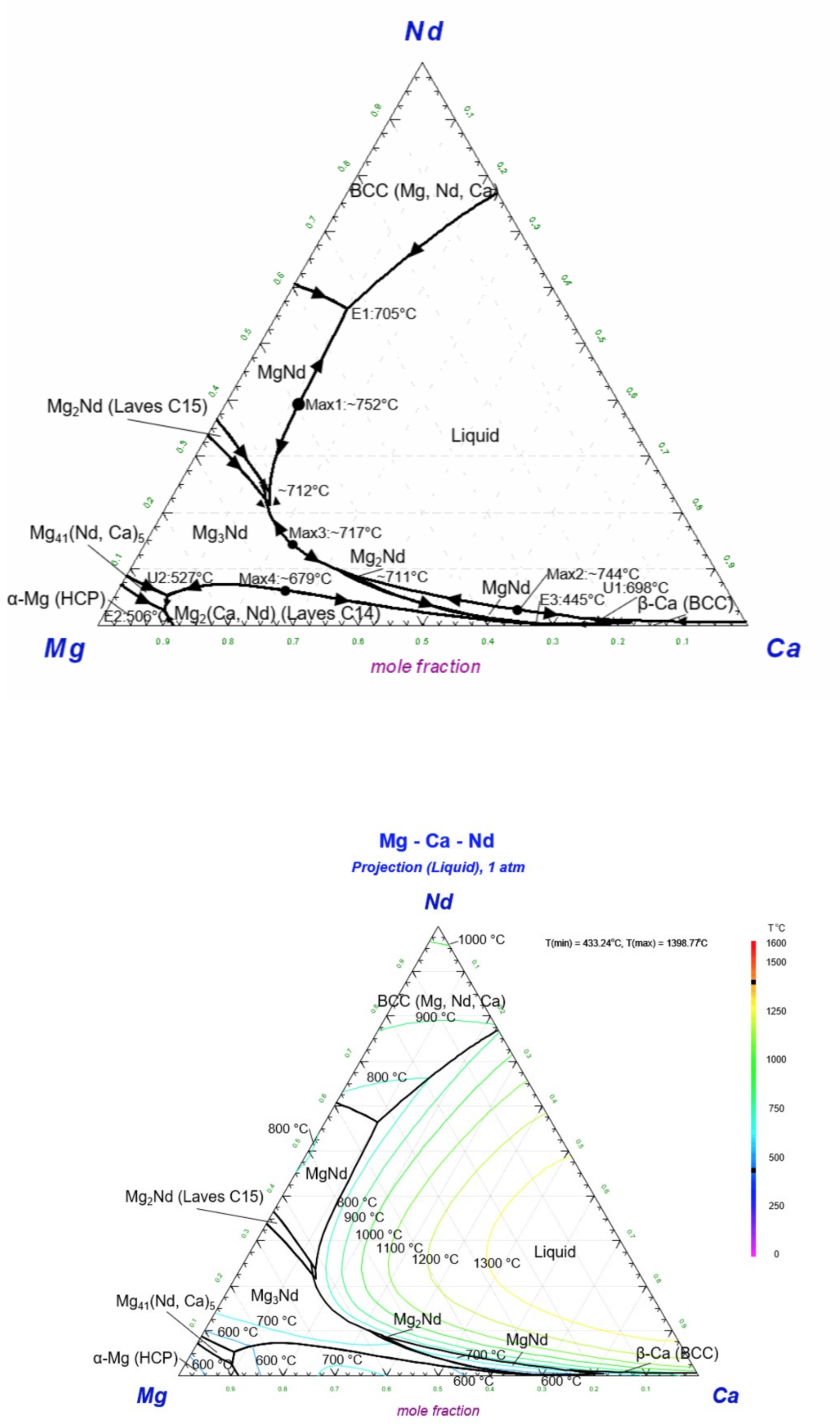

Figure 35, Liquidus projection for the Mg-Ca-Nd ternary system predicted in the present study

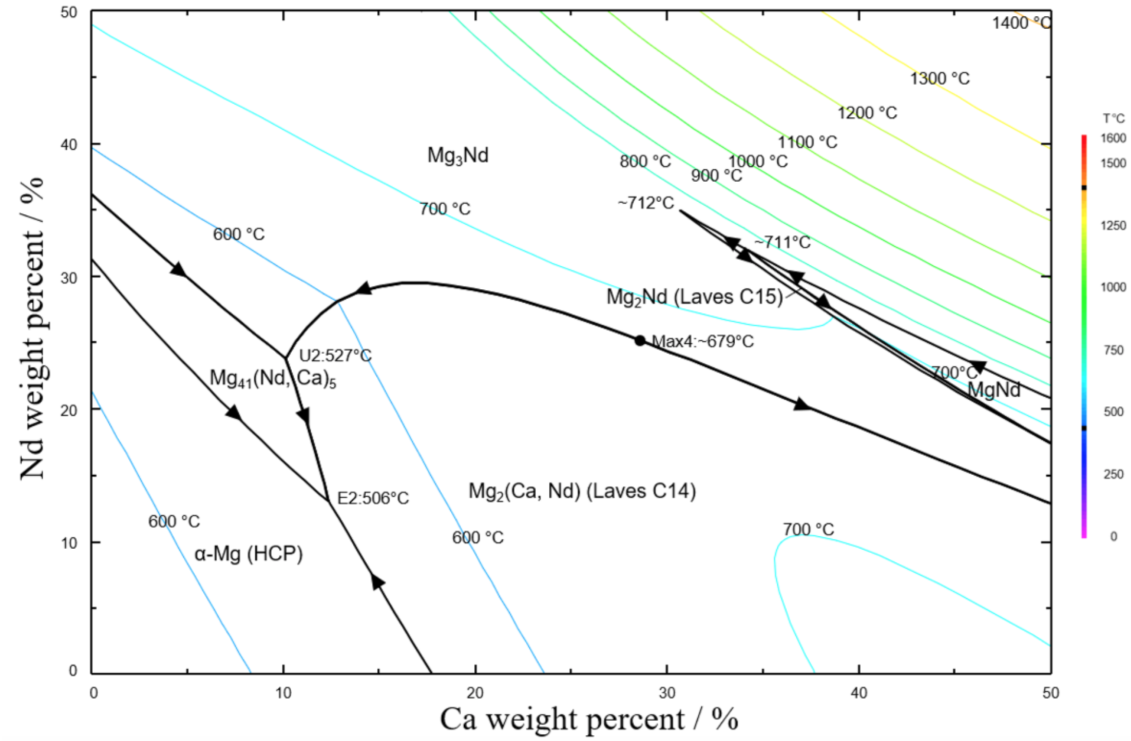

Figure 36, Liquidus projection in the Mg-rich region for the Mg-Ca-Nd system predicted in the present study

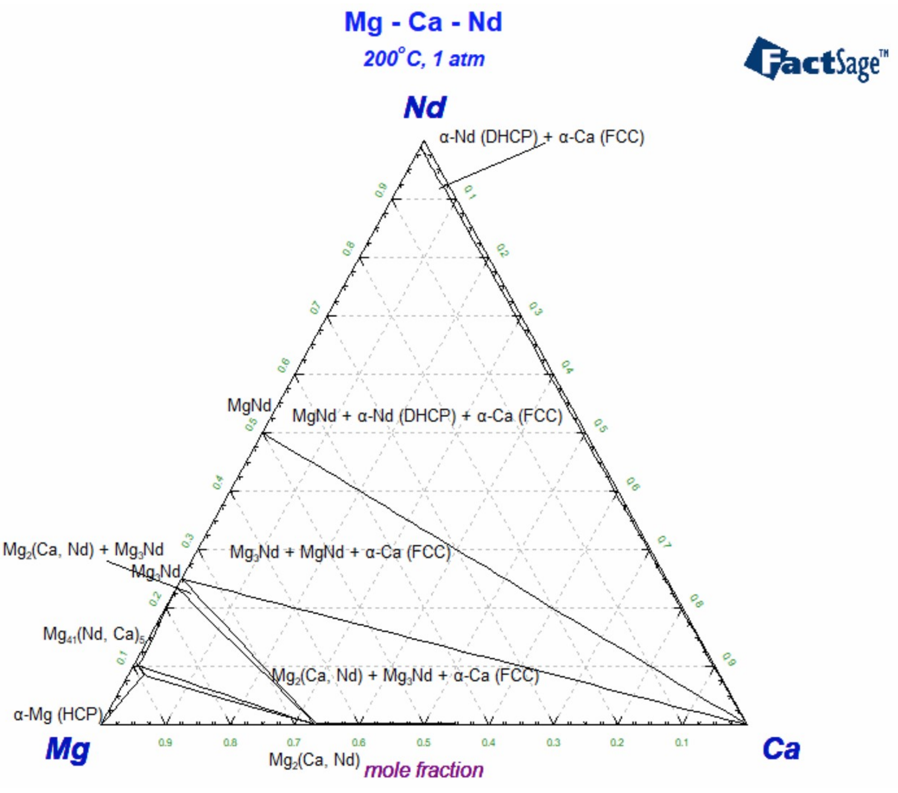

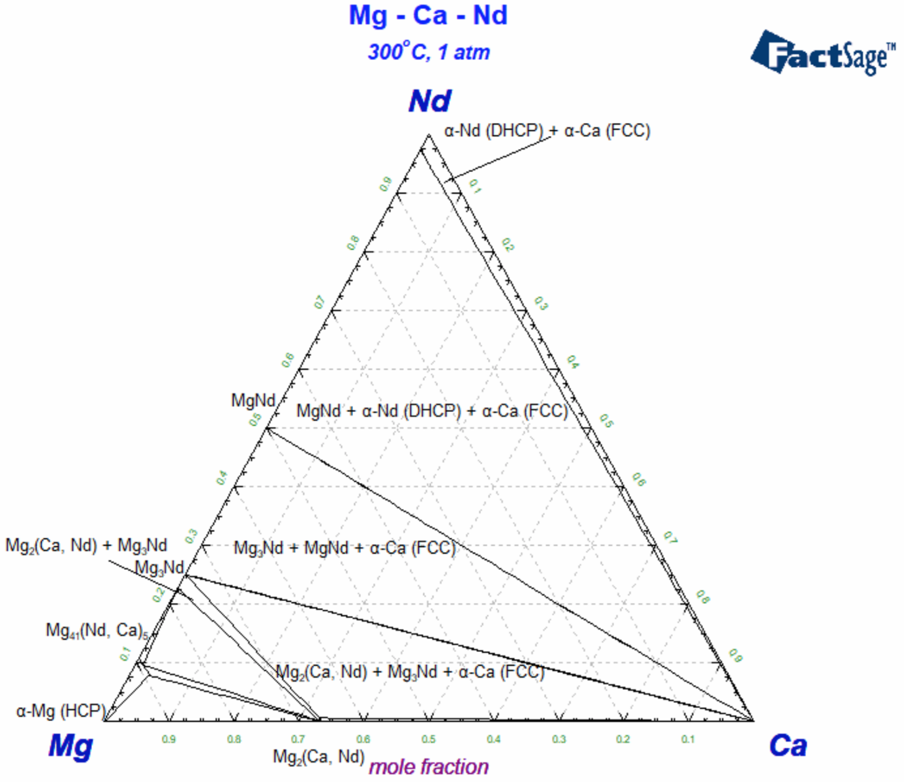
Mg - Ca - Nd
300°C, 1 atm
Nd
α-Nd (DHCP) + α-Ca (FCC)
MgNd
MgNd + α-Nd (DHCP) + α-Ca (FCC)
Mg_2(Ca, Nd) + Mg_3Nd
Mg_3Nd
Mg_3Nd + MgNd + α-Ca (FCC)
Mg_{41}(Nd, Ca)$_5$
Mg_2(Ca, Nd) + Mg_3Nd + α-Ca (FCC)
α-Mg (HCP)
Mg
Ca
0.9
0.8
0.7
0.6
0.5
0.4
0.3
0.2
0.1
Mg_2(Ca, Nd)
mole fraction

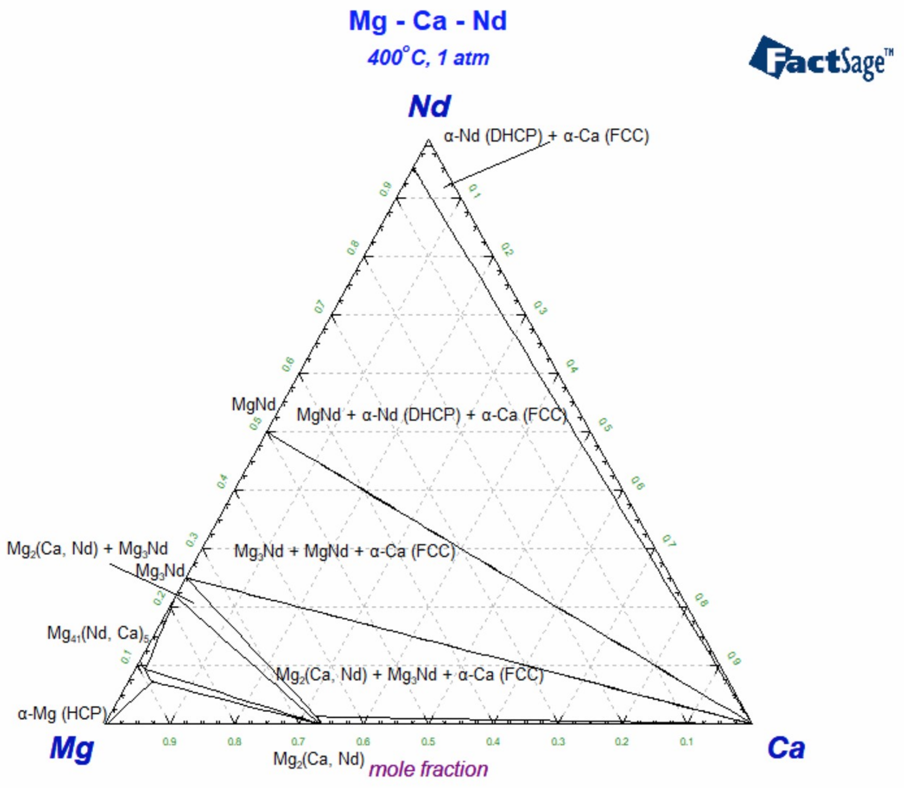
Mg - Ca - Nd
400°C, 1 atm
Nd
α-Nd (DHCP) + α-Ca (FCC)
MgNd
MgNd + α-Nd (DHCP) + α-Ca (FCC)
Mg_2(Ca, Nd) + Mg_3Nd
Mg_3Nd
Mg_3Nd + MgNd + α-Ca (FCC)
Mg_{41}(Nd, Ca)$_5$
Mg_2(Ca, Nd) + Mg_3Nd + α-Ca (FCC)
α-Mg (HCP)
Mg
Ca
0.9
0.8
0.7
0.6
0.5
0.4
0.3
0.2
0.1
Mg_2(Ca, Nd)
mole fraction

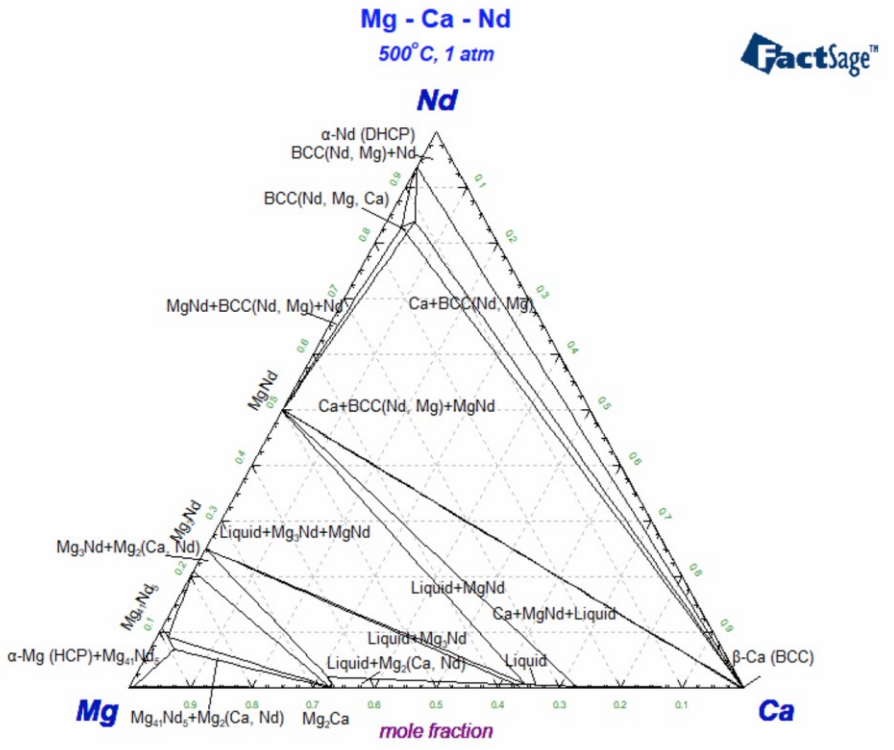
Mg - Ca - Nd
500°C, 1 atm
FactSage™
Nd
α-Nd (DHCP)
BCC(Nd, Mg)+Nd
BCC(Nd, Mg, Ca)
MgNd+BCC(Nd, Mg)+Nd
Ca+BCC(Nd, Mg)
MgNd
Ca+BCC(Nd, Mg)+MgNd
Mg3Nd
Liquid+Mg3Nd+MgNd
Mg3Nd+Mg2(Ca, Nd)
Mg41Nd5
Liquid+MgNd
Ca+MgNd+Liquid
Liquid+Mg3Nd
α-Mg (HCP)+Mg41Nd5
Liquid+Mg2(Ca, Nd)
Liquid
β-Ca (BCC)
Mg
Mg41Nd5+Mg2(Ca, Nd)
Mg2Ca
mole fraction
Ca

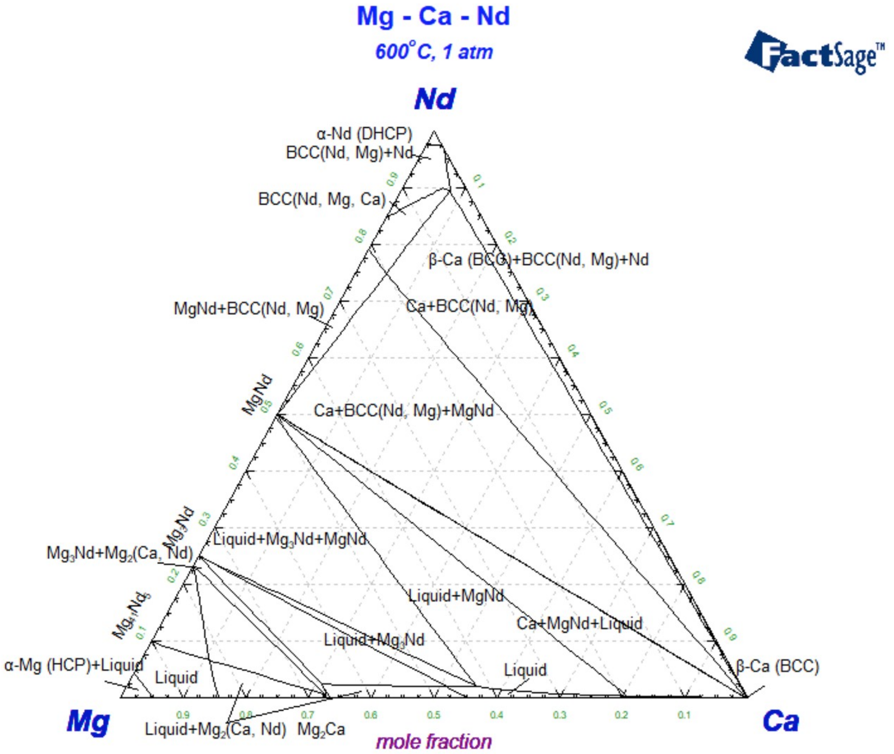
Mg - Ca - Nd
600°C, 1 atm
FactSage™
Nd
α-Nd (DHCP)
BCC(Nd, Mg)+Nd
BCC(Nd, Mg, Ca)
β-Ca (BCC)+BCC(Nd, Mg)+Nd
MgNd+BCC(Nd, Mg)
Ca+BCC(Nd, Mg)
MgNd
Ca+BCC(Nd, Mg)+MgNd
Mg3Nd
Liquid+Mg3Nd+MgNd
Mg3Nd+Mg2(Ca, Nd)
Liquid+MgNd
Mg41Nd5
Ca+MgNd+Liquid
Liquid+Mg3Nd
α-Mg (HCP)+Liquid
Liquid
Liquid
β-Ca (BCC)
Mg
Liquid+Mg2(Ca, Nd)
Mg2Ca
mole fraction
Ca

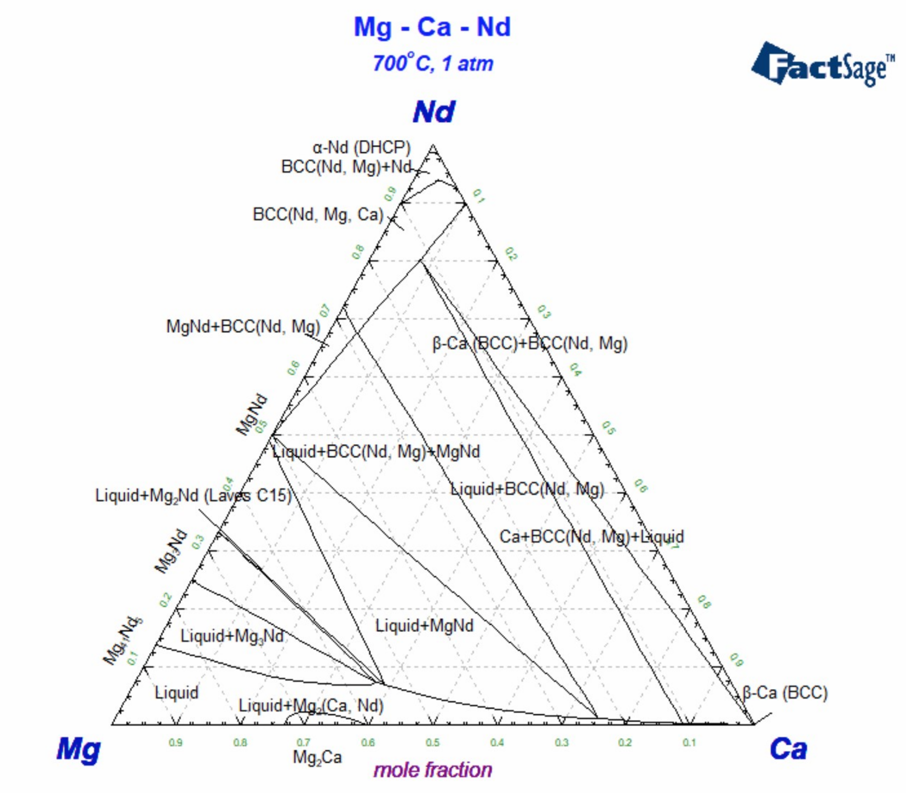

Figure 37, Isothermal sections of the Mg-Ca-Nd ternary system at 200-700ºC

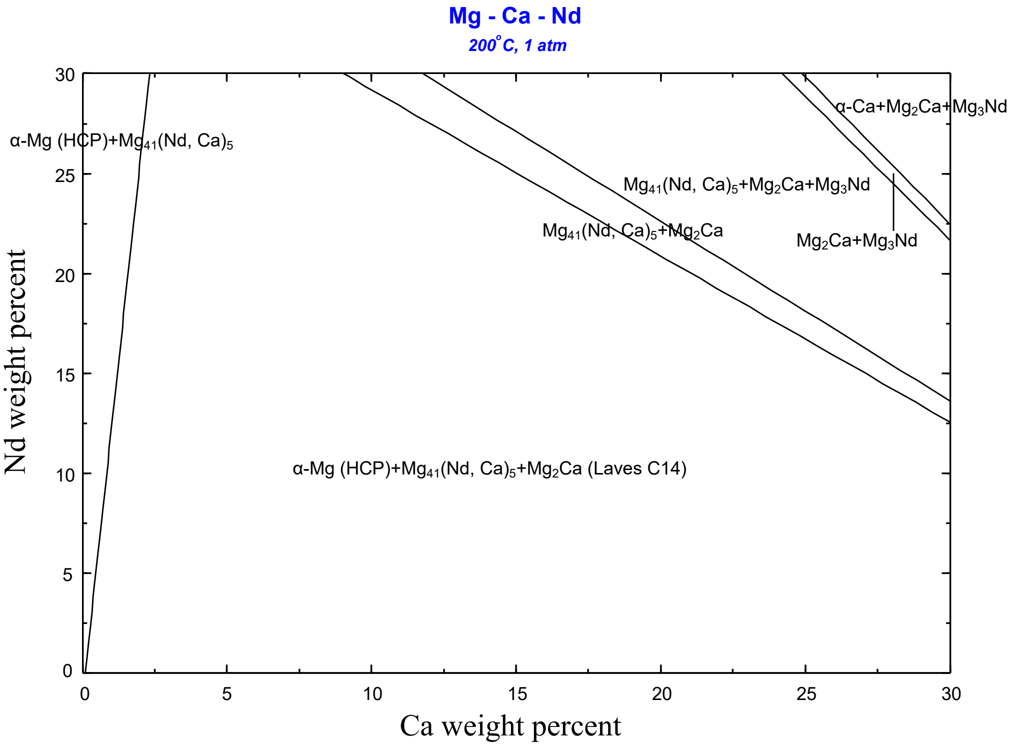

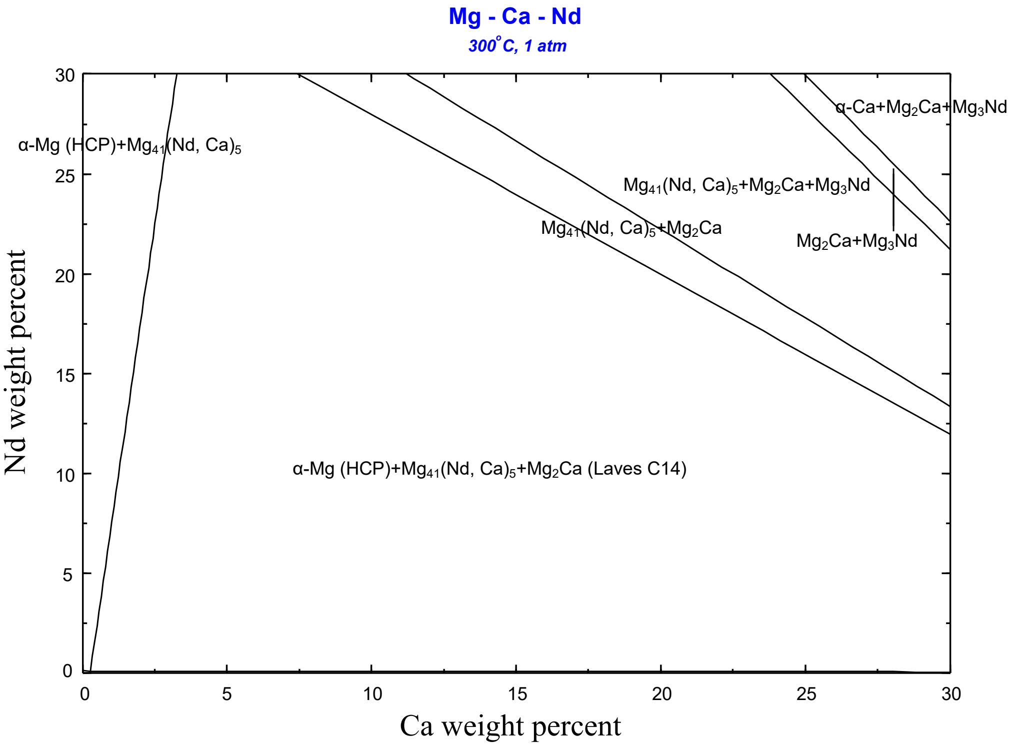
Mg - Ca - Nd
300°C, 1 atm
α-Mg (HCP)+Mg41(Nd, Ca)5
α-Ca+Mg2Ca+Mg3Nd
Mg41(Nd, Ca)5+Mg2Ca+Mg3Nd
Mg41(Nd, Ca)5+Mg2Ca
Mg2Ca+Mg3Nd
α-Mg (HCP)+Mg41(Nd, Ca)5+Mg2Ca (Laves C14)
Nd weight percent
Ca weight percent
0
5
10
15
20
25
30

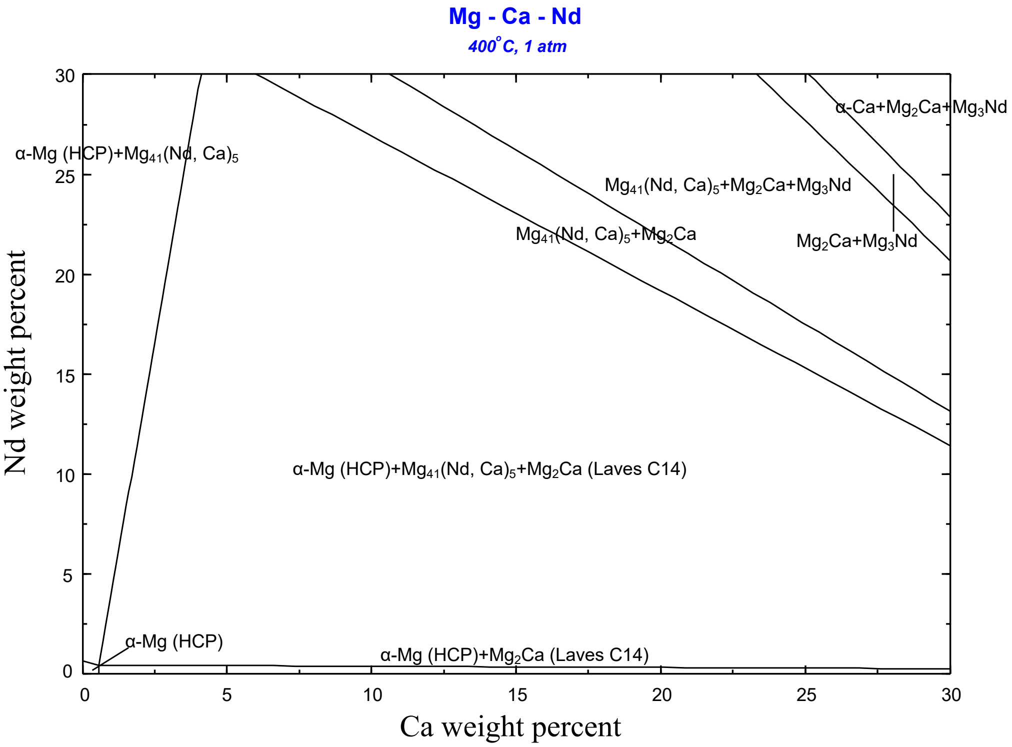
Mg - Ca - Nd
400°C, 1 atm
α-Mg (HCP)+Mg41(Nd, Ca)5
α-Ca+Mg2Ca+Mg3Nd
Mg41(Nd, Ca)5+Mg2Ca+Mg3Nd
Mg41(Nd, Ca)5+Mg2Ca
Mg2Ca+Mg3Nd
α-Mg (HCP)+Mg41(Nd, Ca)5+Mg2Ca (Laves C14)
α-Mg (HCP)
α-Mg (HCP)+Mg2Ca (Laves C14)
Nd weight percent
Ca weight percent
0
5
10
15
20
25
30

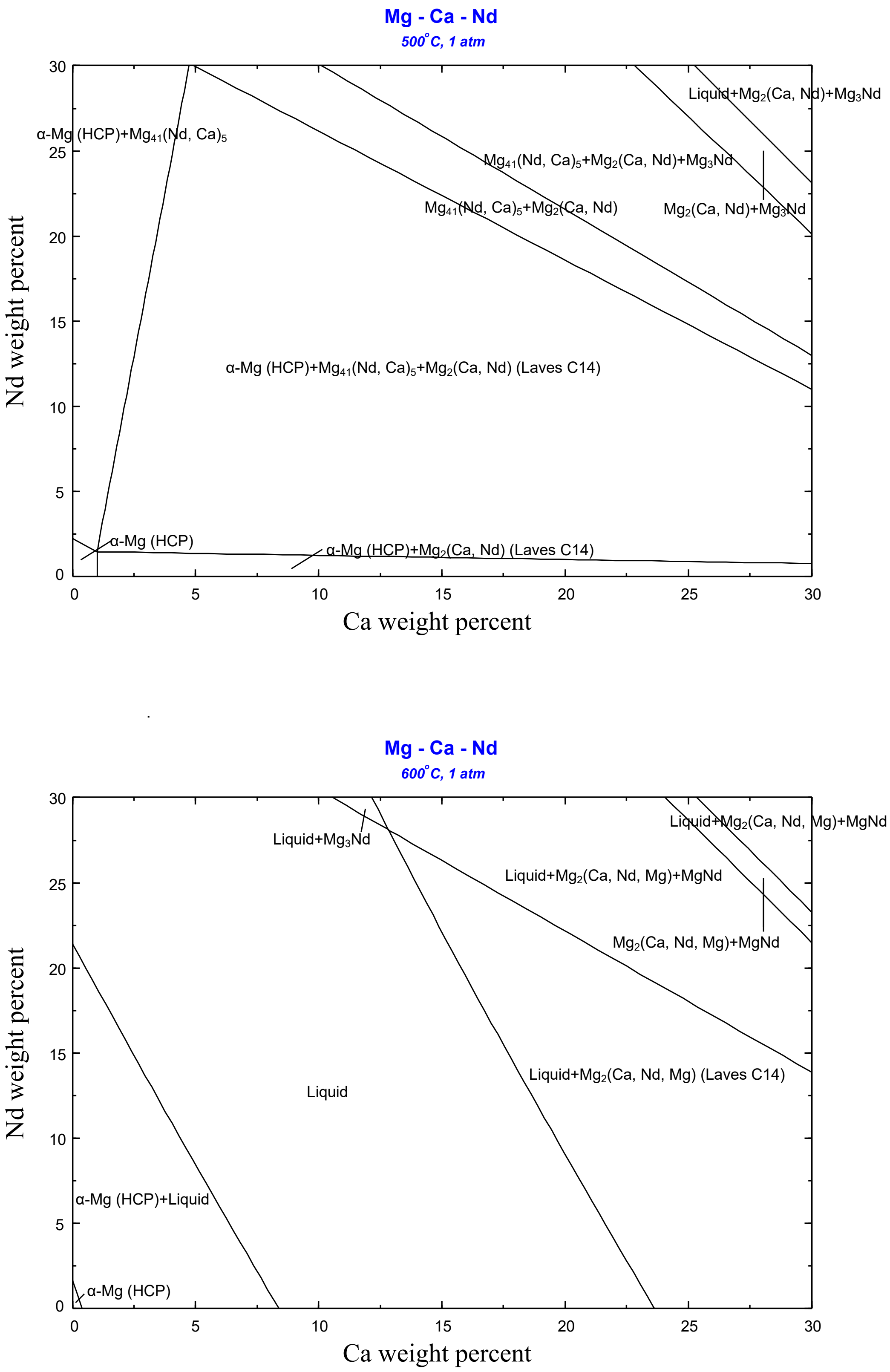

Figure 38, Isothermal sections of the Mg-Ca-Nd system in the Mg-rich region at 200-600℃

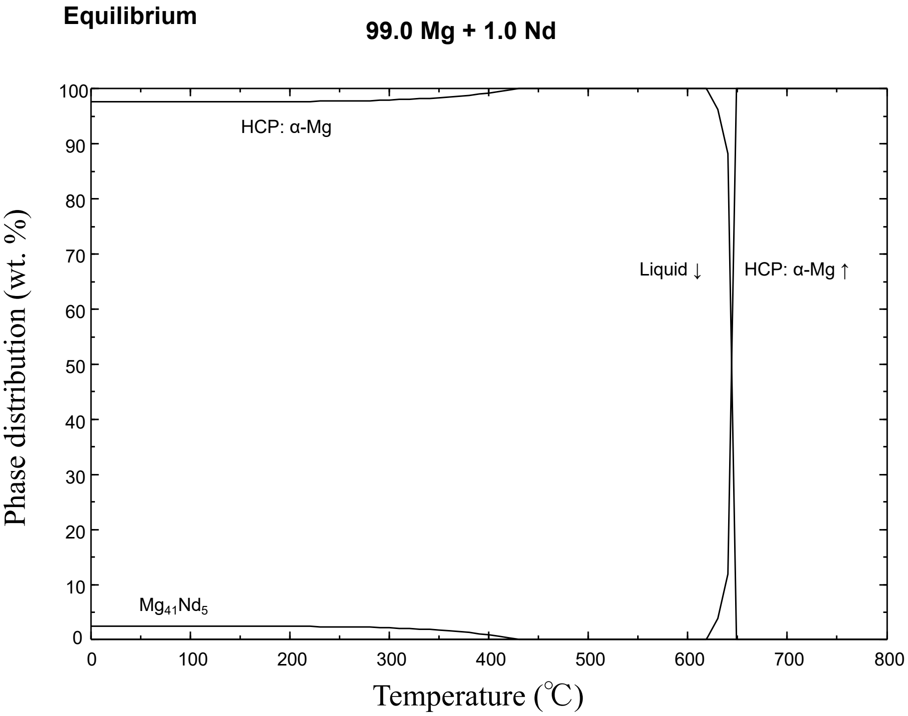
Equilibrium
99.0 Mg + 1.0 Nd
Phase distribution (wt. %)
0
10
20
30
40
50
60
70
80
90
100
Temperature (℃)
0
100
200
300
400
500
600
700
800
HCP: α-Mg
Mg41Nd5
Liquid ↓
HCP: α-Mg ↑

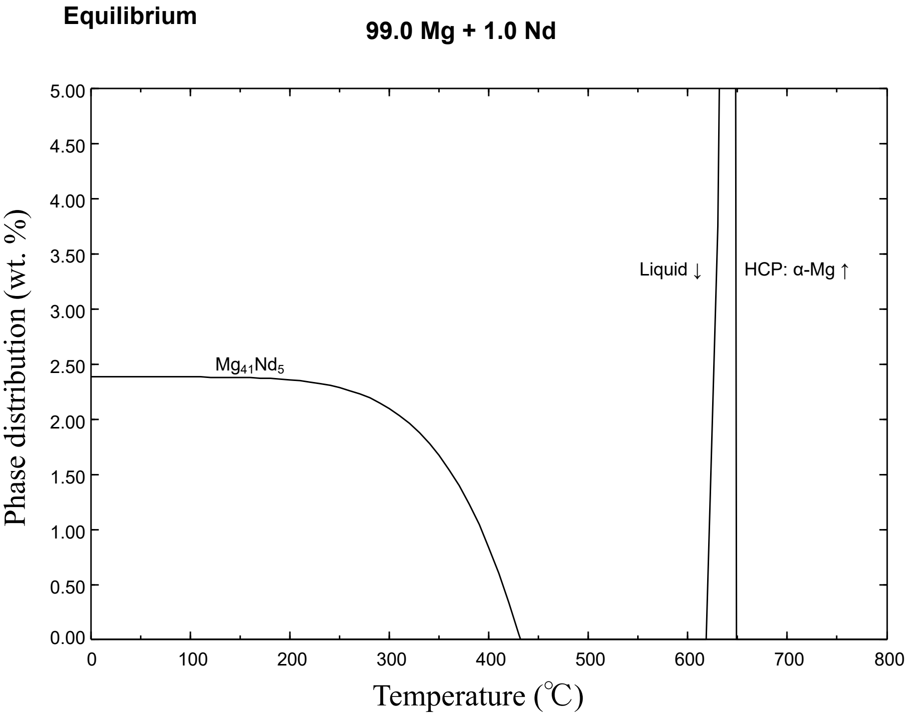
Equilibrium
99.0 Mg + 1.0 Nd
Phase distribution (wt. %)
0.00
0.50
1.00
1.50
2.00
2.50
3.00
3.50
4.00
4.50
5.00
Temperature (℃)
0
100
200
300
400
500
600
700
800
Mg41Nd5
Liquid ↓
HCP: α-Mg ↑

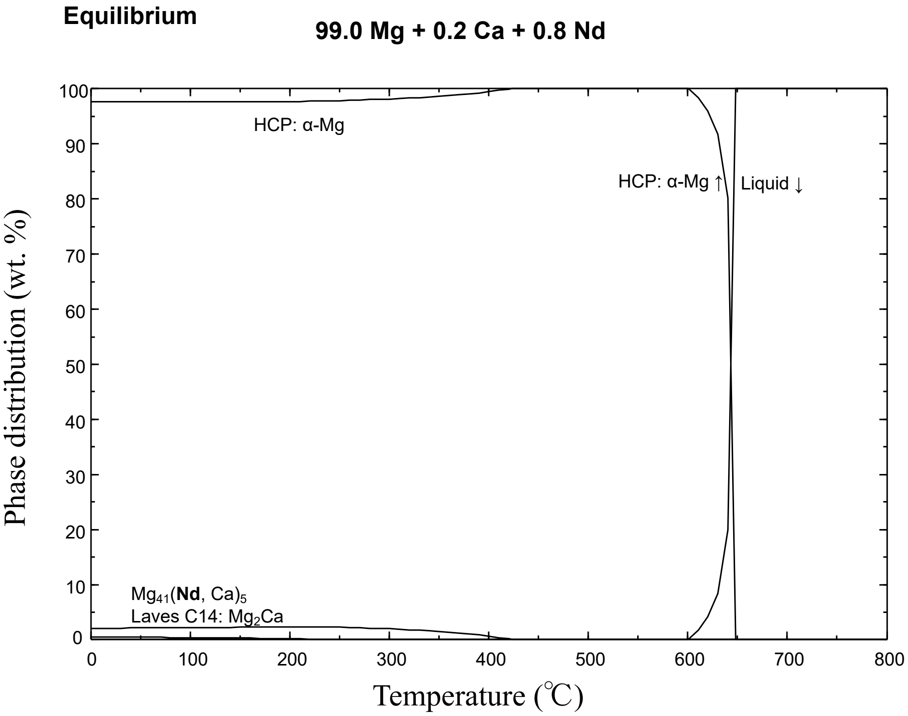
Equilibrium
99.0 Mg + 0.2 Ca + 0.8 Nd
HCP: α-Mg
HCP: α-Mg ↑
Liquid ↓
Mg_{41}(**Nd**, Ca)$_5$
Laves C14: Mg_2Ca
Phase distribution (wt. %)
0
10
20
30
40
50
60
70
80
90
100
Temperature (℃)
0
100
200
300
400
500
600
700
800

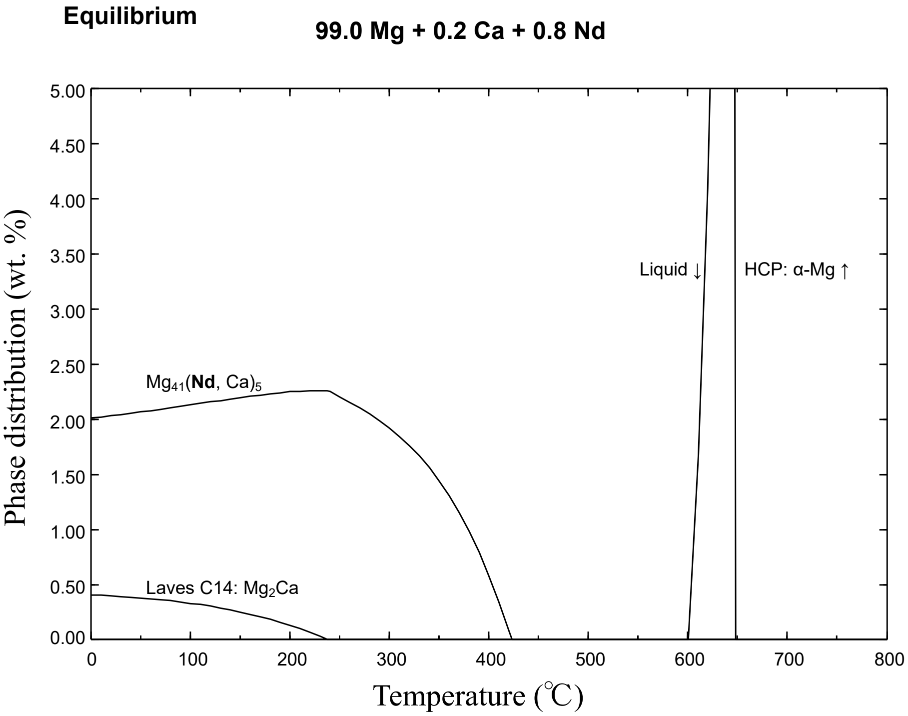
Equilibrium
99.0 Mg + 0.2 Ca + 0.8 Nd
Liquid ↓
HCP: α-Mg ↑
Mg_{41}(**Nd**, Ca)$_5$
Laves C14: Mg_2Ca
Phase distribution (wt. %)
0.00
0.50
1.00
1.50
2.00
2.50
3.00
3.50
4.00
4.50
5.00
Temperature (℃)
0
100
200
300
400
500
600
700
800

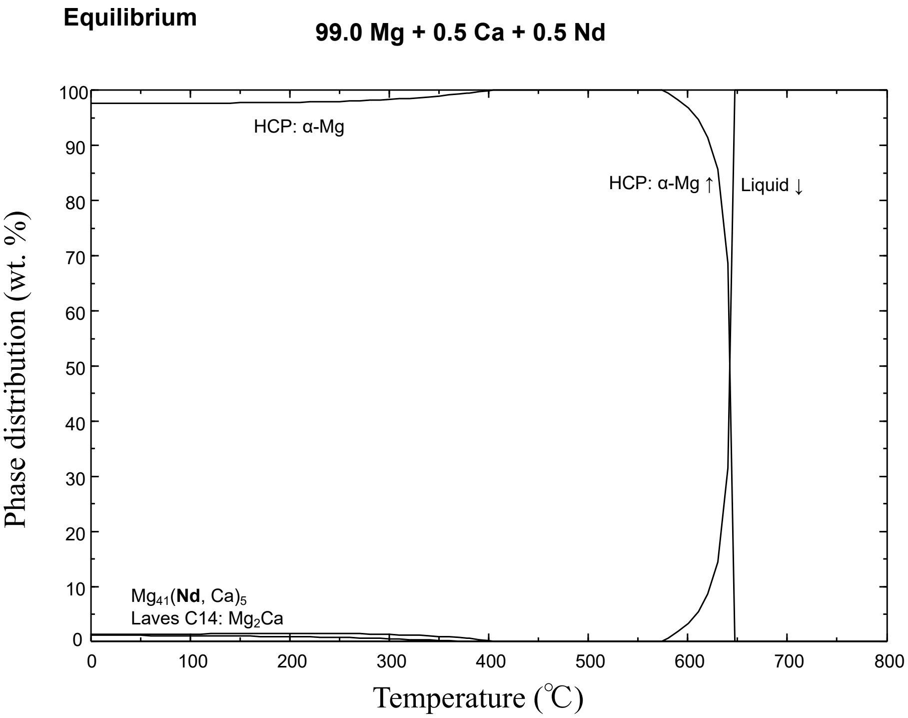
Equilibrium
99.0 Mg + 0.5 Ca + 0.5 Nd
HCP: α-Mg
HCP: α-Mg ↑
Liquid ↓
Mg_{41}(**Nd**, Ca)$_5$
Laves C14: Mg_2Ca
Phase distribution (wt. %)
0
10
20
30
40
50
60
70
80
90
100
0
100
200
300
400
500
600
700
800
Temperature (℃)

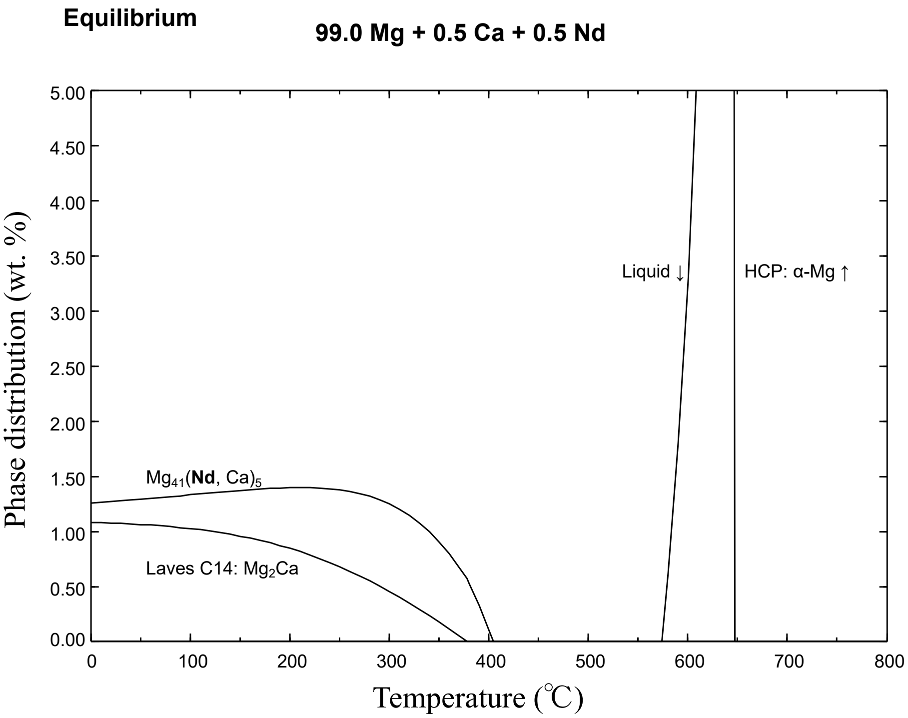
Equilibrium
99.0 Mg + 0.5 Ca + 0.5 Nd
Liquid ↓
HCP: α-Mg ↑
Mg_{41}(**Nd**, Ca)$_5$
Laves C14: Mg_2Ca
Phase distribution (wt. %)
0.00
0.50
1.00
1.50
2.00
2.50
3.00
3.50
4.00
4.50
5.00
0
100
200
300
400
500
600
700
800
Temperature (℃)

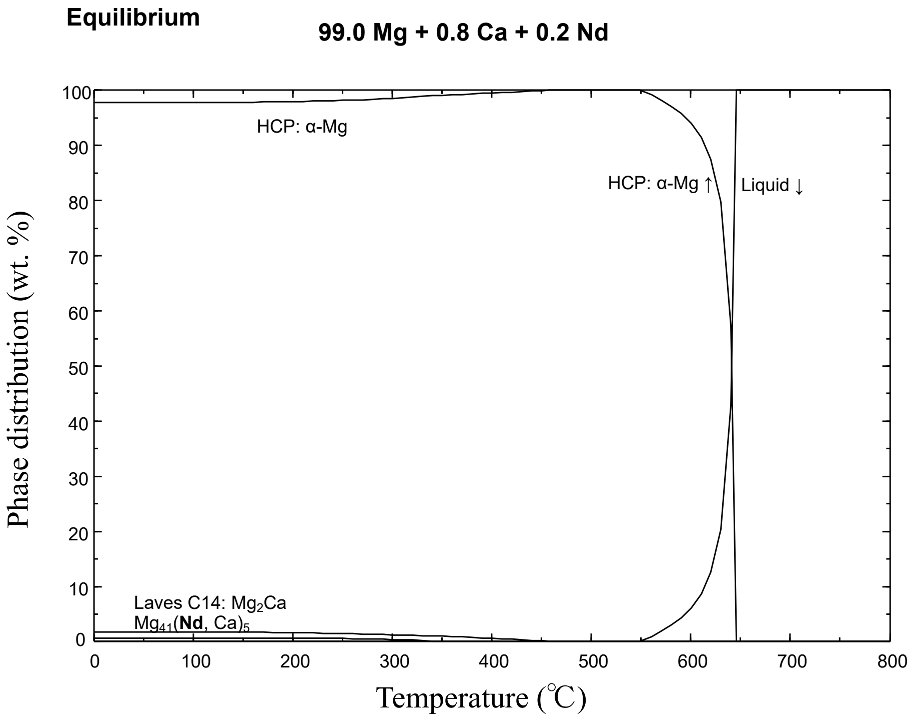
Equilibrium
99.0 Mg + 0.8 Ca + 0.2 Nd
HCP: α-Mg
HCP: α-Mg ↑
Liquid ↓
Laves C14: Mg_2Ca
Mg_{41}(**Nd**, Ca)$_5$
Phase distribution (wt. %)
0
10
20
30
40
50
60
70
80
90
100
Temperature (℃)
0
100
200
300
400
500
600
700
800

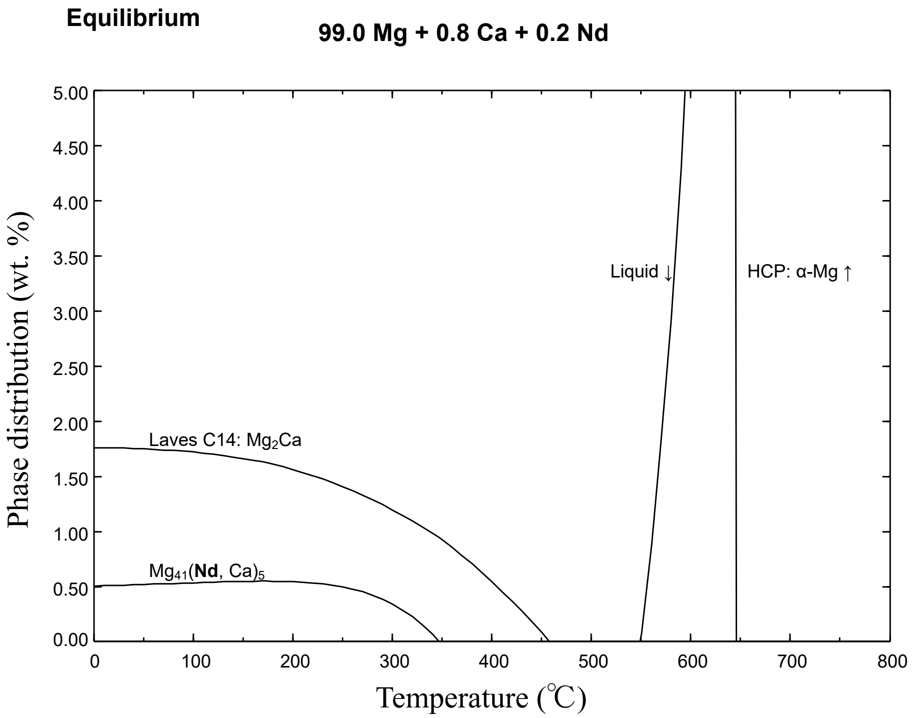
Equilibrium
99.0 Mg + 0.8 Ca + 0.2 Nd
Liquid ↓
HCP: α-Mg ↑
Laves C14: Mg_2Ca
Mg_{41}(**Nd**, Ca)$_5$
Phase distribution (wt. %)
0.00
0.50
1.00
1.50
2.00
2.50
3.00
3.50
4.00
4.50
5.00
Temperature (℃)
0
100
200
300
400
500
600
700
800

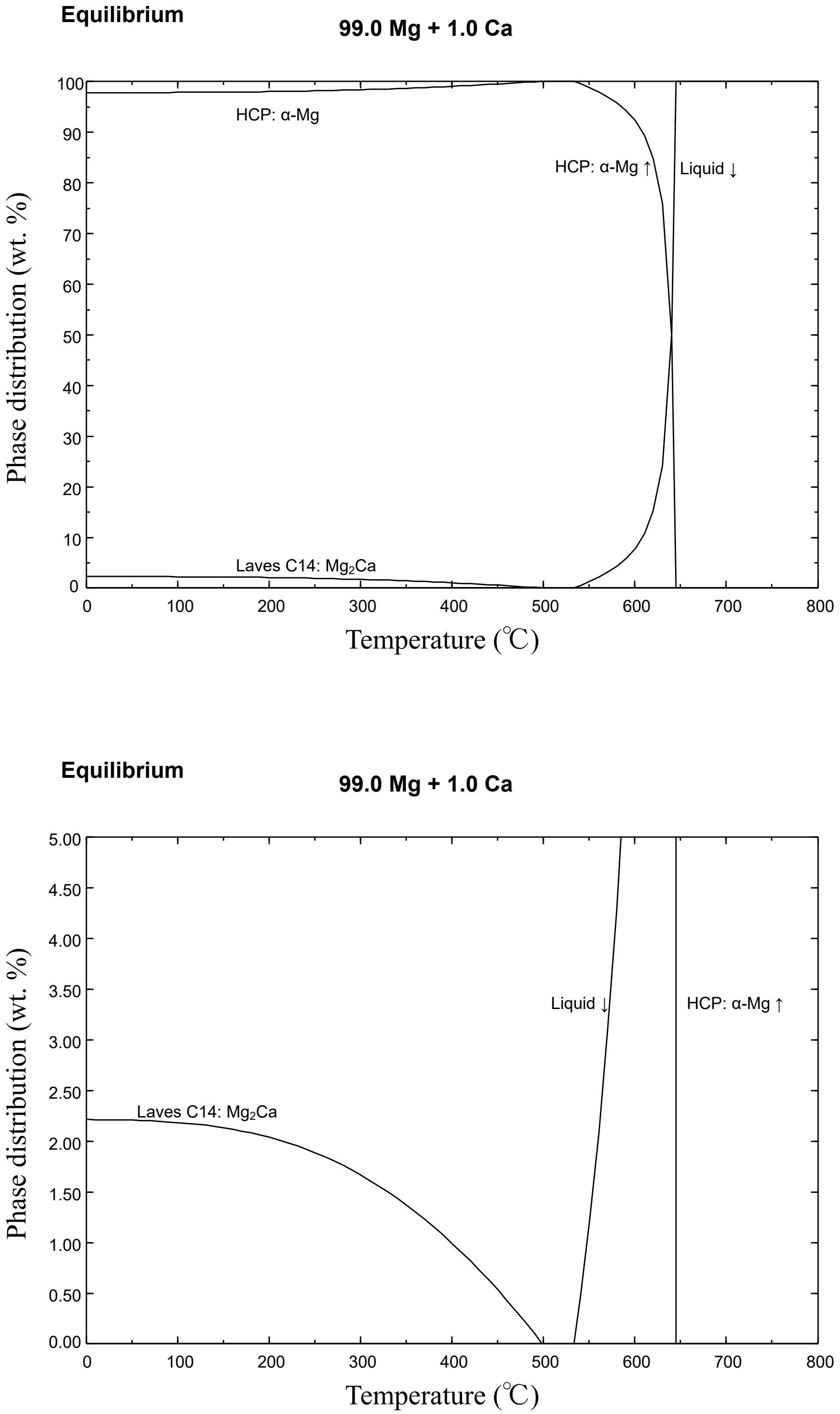

Figure 39, Calculated phase distributions for Mg-Ca-Nd alloys as potential Mg wrought alloys

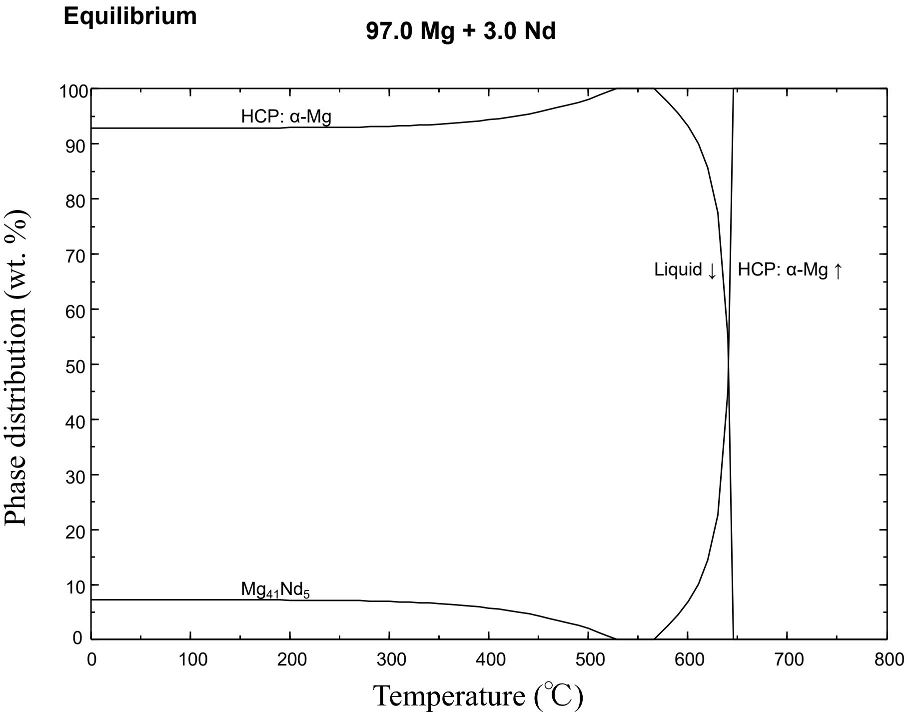
Equilibrium
97.0 Mg + 3.0 Nd
HCP: α-Mg
Mg41Nd5
Liquid ↓
HCP: α-Mg ↑
Phase distribution (wt. %)
Temperature (℃)
0
10
20
30
40
50
60
70
80
90
100
0
100
200
300
400
500
600
700
800

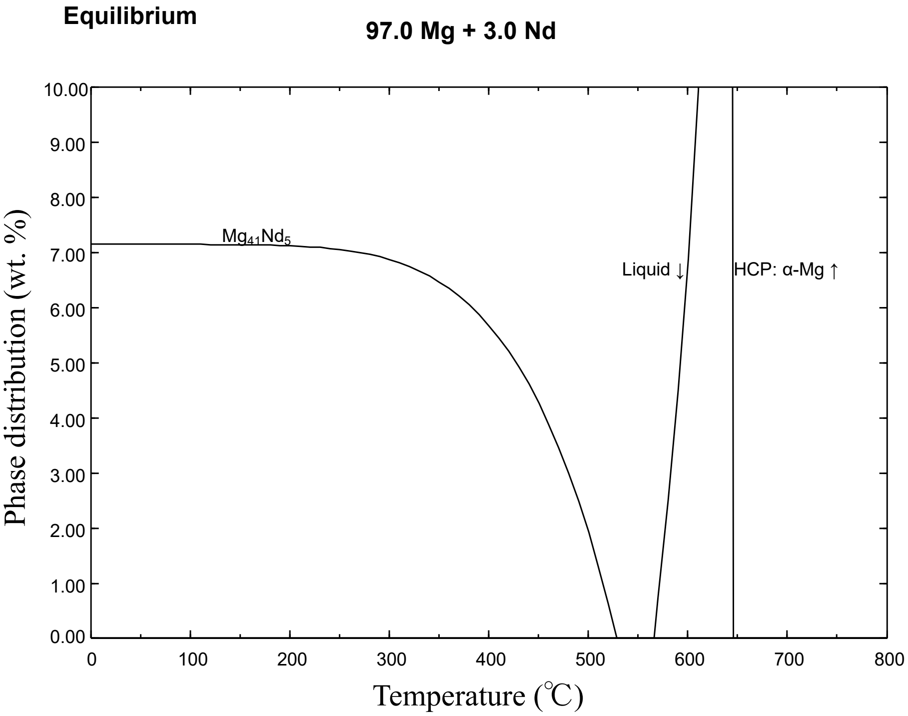
Equilibrium
97.0 Mg + 3.0 Nd
Mg41Nd5
Liquid ↓
HCP: α-Mg ↑
Phase distribution (wt. %)
Temperature (℃)
0.00
1.00
2.00
3.00
4.00
5.00
6.00
7.00
8.00
9.00
10.00
0
100
200
300
400
500
600
700
800

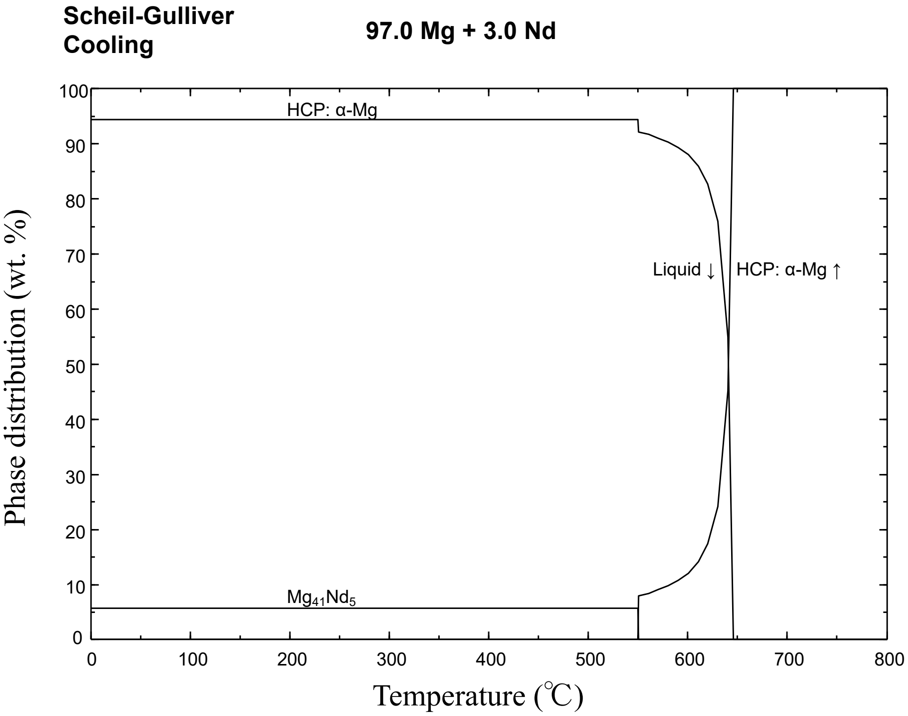
Scheil-Gulliver
Cooling
97.0 Mg + 3.0 Nd
HCP: α-Mg
Liquid ↓
HCP: α-Mg ↑
Mg41Nd5
Phase distribution (wt. %)
100
90
80
70
60
50
40
30
20
10
0
0
100
200
300
400
500
600
700
800
Temperature (℃)

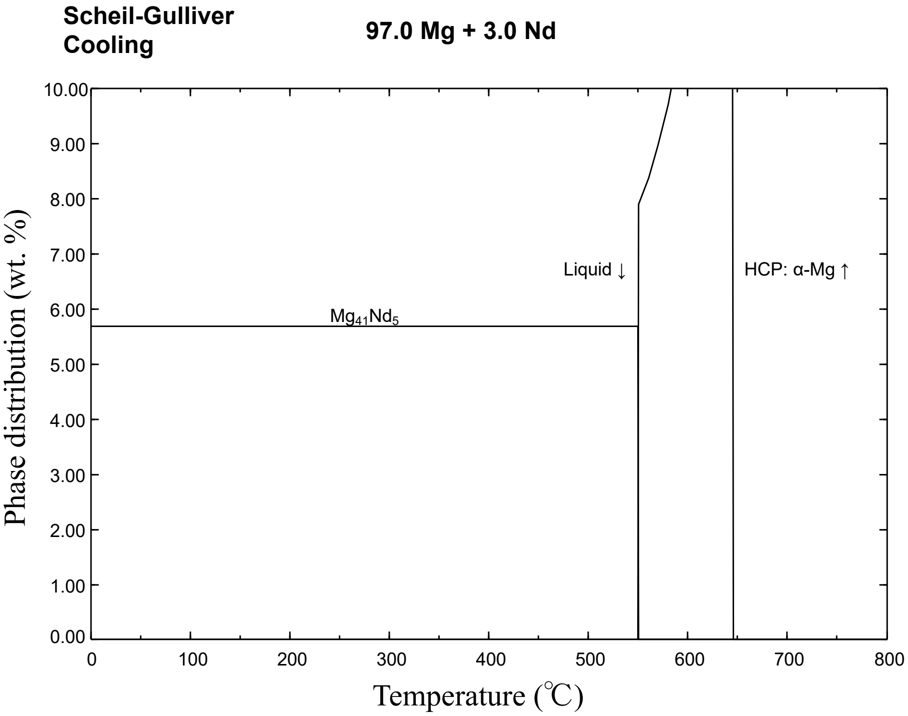
Scheil-Gulliver
Cooling
97.0 Mg + 3.0 Nd
Liquid ↓
HCP: α-Mg ↑
Mg41Nd5
Phase distribution (wt. %)
10.00
9.00
8.00
7.00
6.00
5.00
4.00
3.00
2.00
1.00
0.00
0
100
200
300
400
500
600
700
800
Temperature (℃)

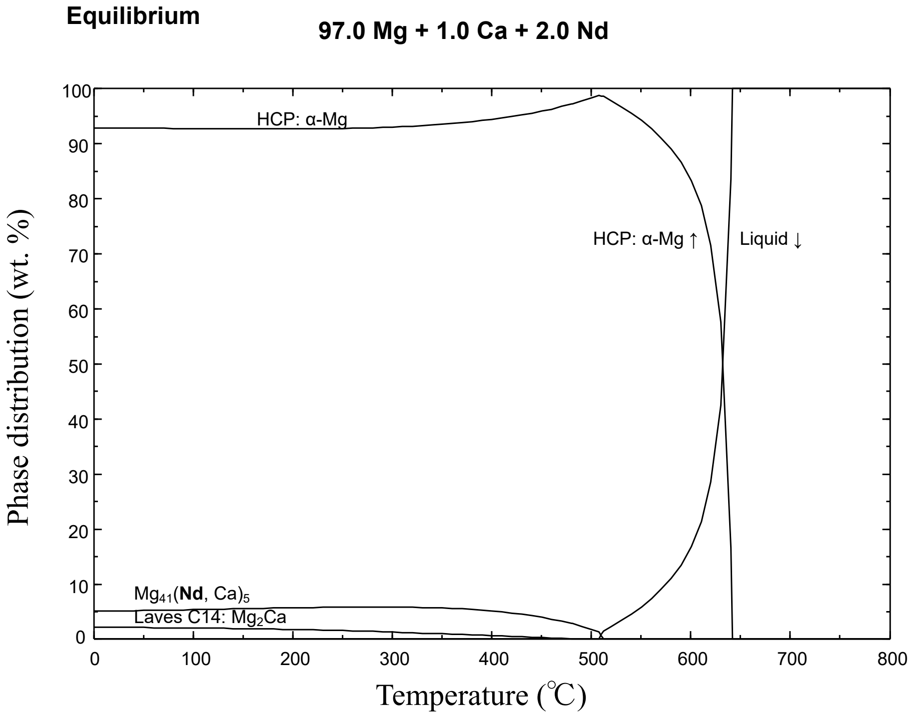
Equilibrium
97.0 Mg + 1.0 Ca + 2.0 Nd
HCP: α-Mg
HCP: α-Mg ↑
Liquid ↓
Mg_{41}(**Nd**, Ca)$_5$
Laves C14: Mg_2Ca
Phase distribution (wt. %)
Temperature (℃)
0
10
20
30
40
50
60
70
80
90
100
0
100
200
300
400
500
600
700
800

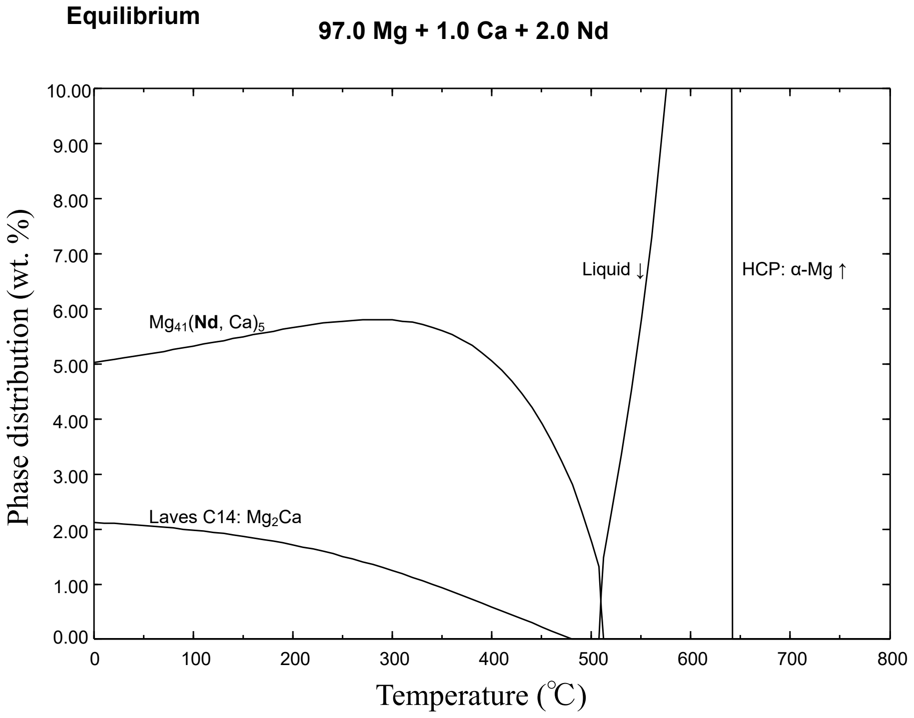
Equilibrium
97.0 Mg + 1.0 Ca + 2.0 Nd
Liquid ↓
HCP: α-Mg ↑
Mg_{41}(**Nd**, Ca)$_5$
Laves C14: Mg_2Ca
Phase distribution (wt. %)
Temperature (℃)
0.00
1.00
2.00
3.00
4.00
5.00
6.00
7.00
8.00
9.00
10.00
0
100
200
300
400
500
600
700
800

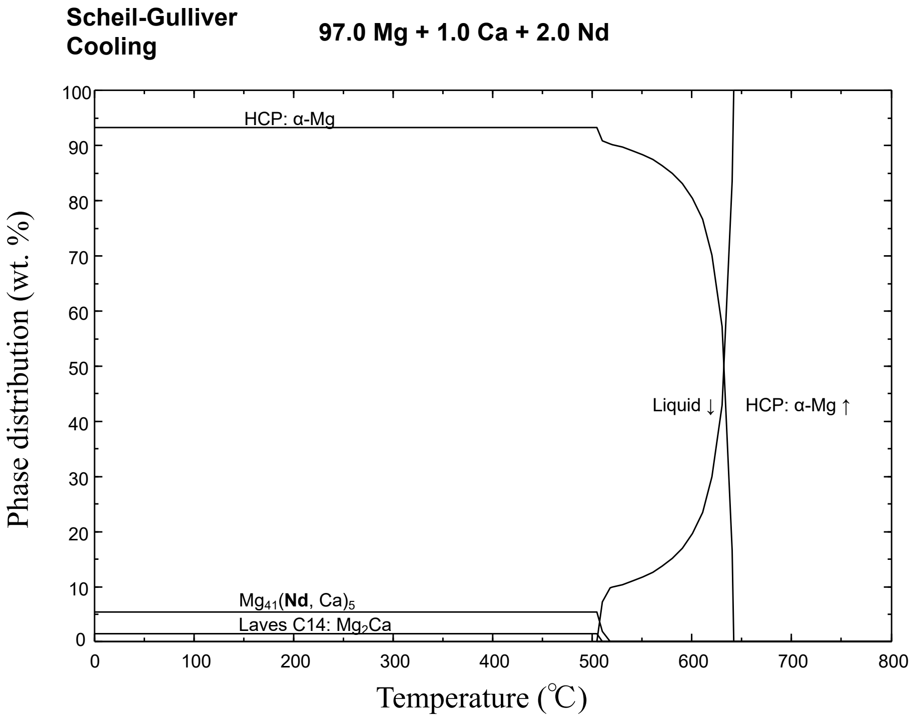
Scheil-Gulliver Cooling
97.0 Mg + 1.0 Ca + 2.0 Nd
Phase distribution (wt. %)
Temperature (℃)
HCP: α-Mg
Liquid ↓
HCP: α-Mg ↑
Mg41(Nd, Ca)5
Laves C14: Mg2Ca
0
10
20
30
40
50
60
70
80
90
100
0
100
200
300
400
500
600
700
800

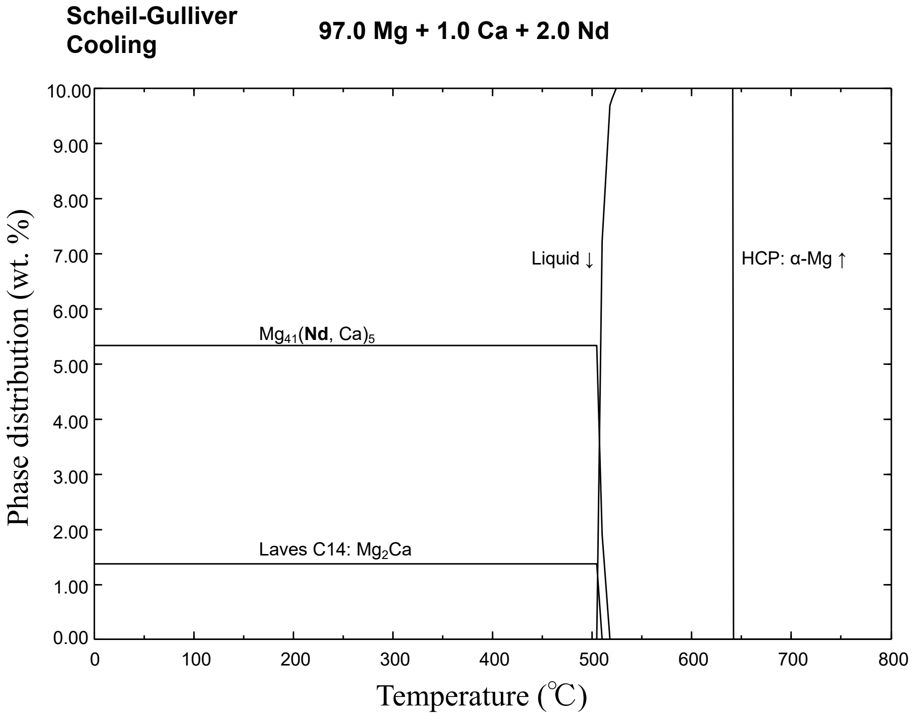
Scheil-Gulliver Cooling
97.0 Mg + 1.0 Ca + 2.0 Nd
Phase distribution (wt. %)
Temperature (℃)
Liquid ↓
HCP: α-Mg ↑
Mg41(Nd, Ca)5
Laves C14: Mg2Ca
0.00
1.00
2.00
3.00
4.00
5.00
6.00
7.00
8.00
9.00
10.00
0
100
200
300
400
500
600
700
800

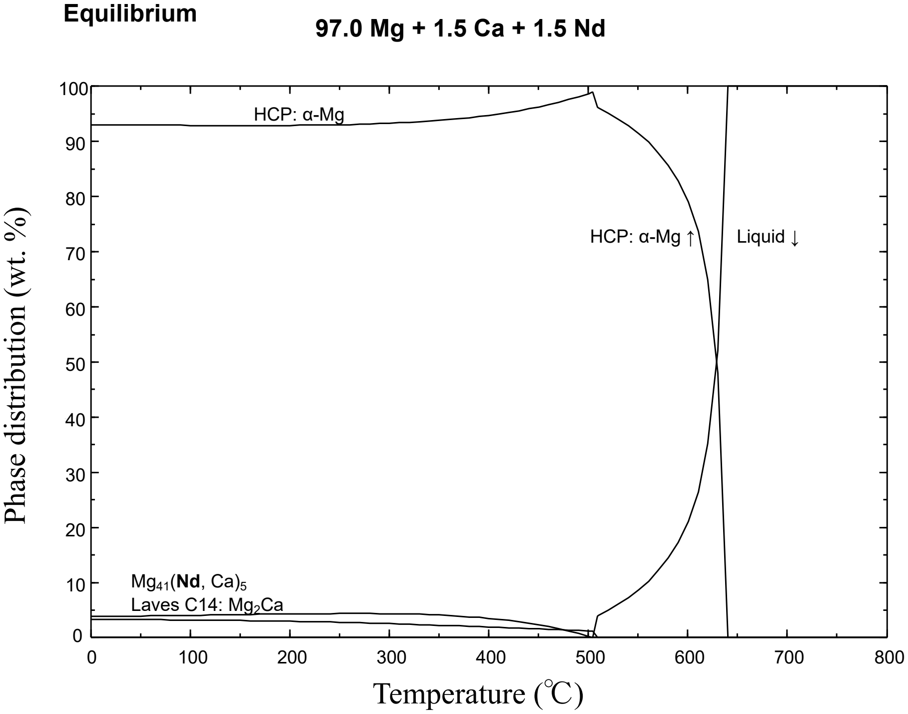
Equilibrium
97.0 Mg + 1.5 Ca + 1.5 Nd
HCP: α-Mg
HCP: α-Mg ↑
Liquid ↓
Mg41(Nd, Ca)5
Laves C14: Mg2Ca
Phase distribution (wt. %)
Temperature (℃)
0
10
20
30
40
50
60
70
80
90
100
0
100
200
300
400
500
600
700
800

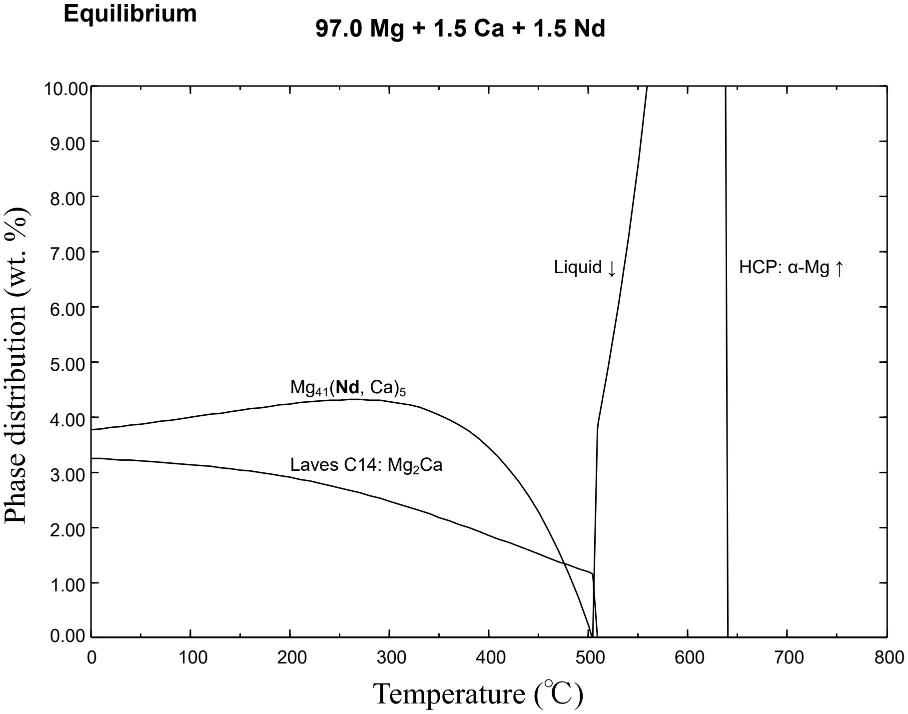
Equilibrium
97.0 Mg + 1.5 Ca + 1.5 Nd
Liquid ↓
HCP: α-Mg ↑
Mg41(Nd, Ca)5
Laves C14: Mg2Ca
Phase distribution (wt. %)
Temperature (℃)
0.00
1.00
2.00
3.00
4.00
5.00
6.00
7.00
8.00
9.00
10.00
0
100
200
300
400
500
600
700
800

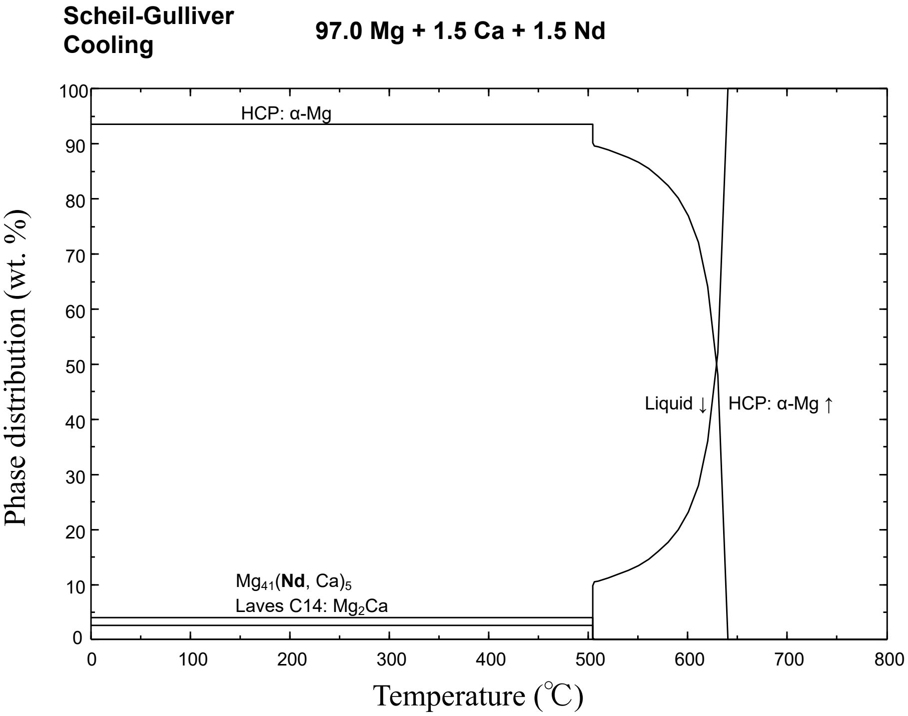
Scheil-Gulliver
Cooling
97.0 Mg + 1.5 Ca + 1.5 Nd
HCP: α-Mg
Liquid ↓
HCP: α-Mg ↑
Mg_{41}(**Nd**, Ca)$_5$
Laves C14: Mg_2Ca
Phase distribution (wt. %)
Temperature (℃)
0
10
20
30
40
50
60
70
80
90
100
0
100
200
300
400
500
600
700
800

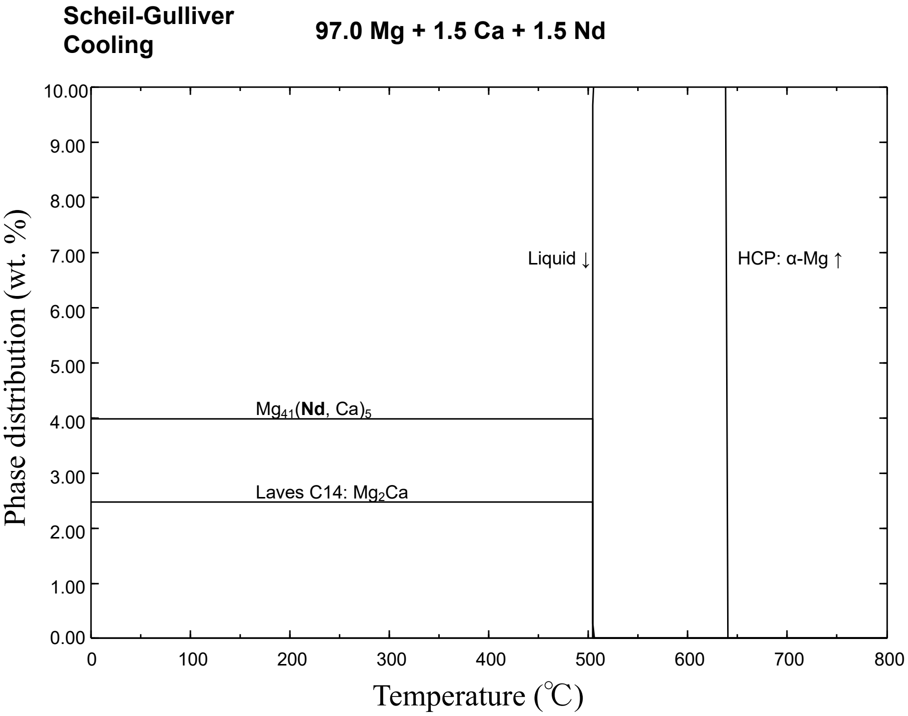
Scheil-Gulliver
Cooling
97.0 Mg + 1.5 Ca + 1.5 Nd
Liquid ↓
HCP: α-Mg ↑
Mg_{41}(**Nd**, Ca)$_5$
Laves C14: Mg_2Ca
Phase distribution (wt. %)
Temperature (℃)
0.00
1.00
2.00
3.00
4.00
5.00
6.00
7.00
8.00
9.00
10.00
0
100
200
300
400
500
600
700
800

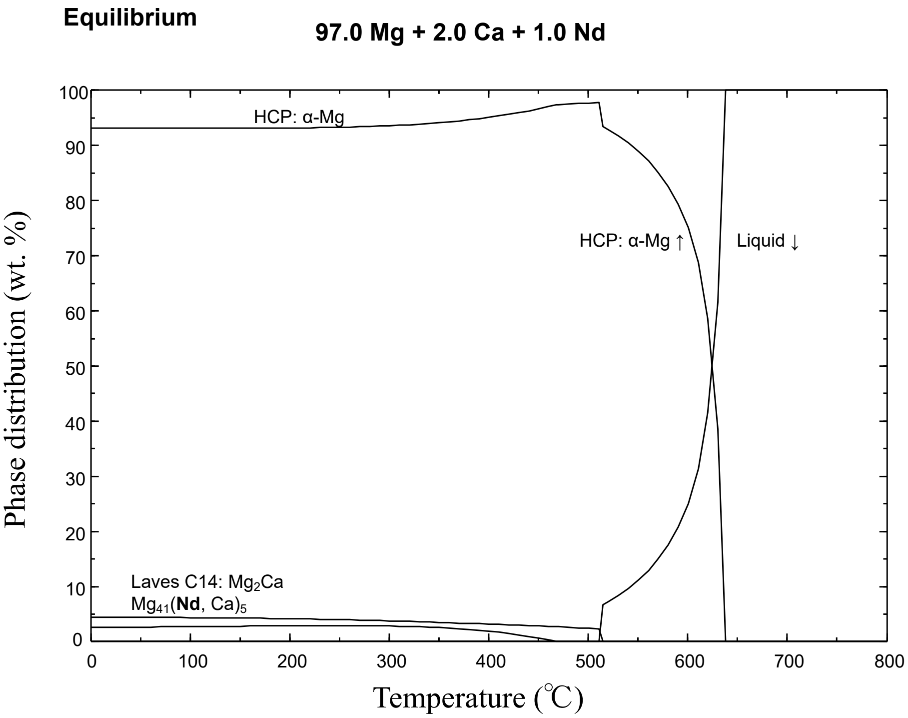
Equilibrium
97.0 Mg + 2.0 Ca + 1.0 Nd
HCP: α-Mg
HCP: α-Mg ↑
Liquid ↓
Laves C14: Mg₂Ca
Mg₄₁(Nd, Ca)₅
Phase distribution (wt. %)
0
10
20
30
40
50
60
70
80
90
100
Temperature (℃)
0
100
200
300
400
500
600
700
800

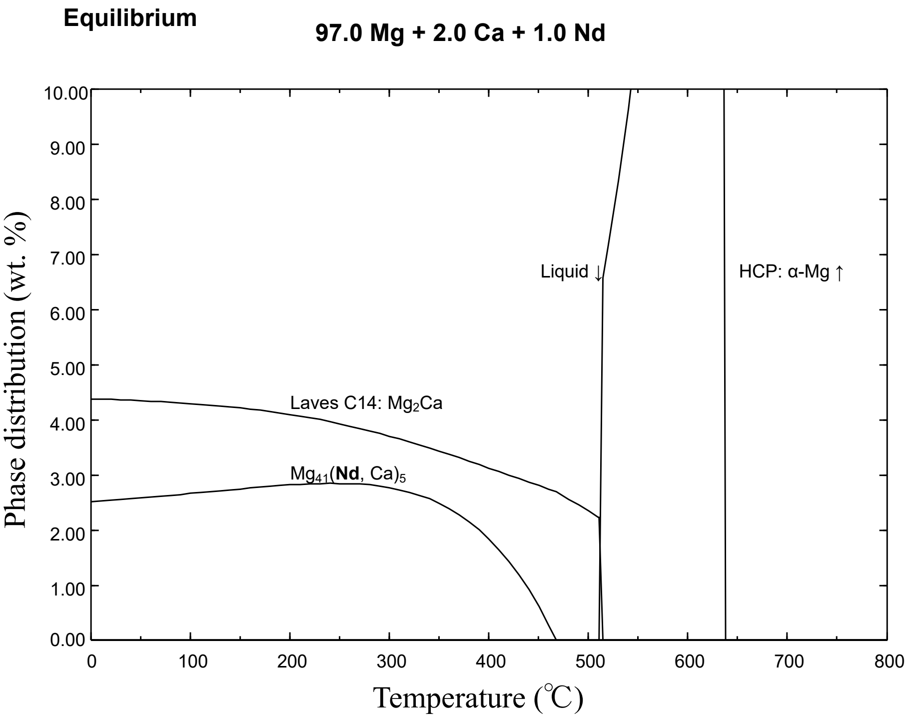
Equilibrium
97.0 Mg + 2.0 Ca + 1.0 Nd
Liquid ↓
HCP: α-Mg ↑
Laves C14: Mg₂Ca
Mg₄₁(Nd, Ca)₅
Phase distribution (wt. %)
0.00
1.00
2.00
3.00
4.00
5.00
6.00
7.00
8.00
9.00
10.00
Temperature (℃)
0
100
200
300
400
500
600
700
800

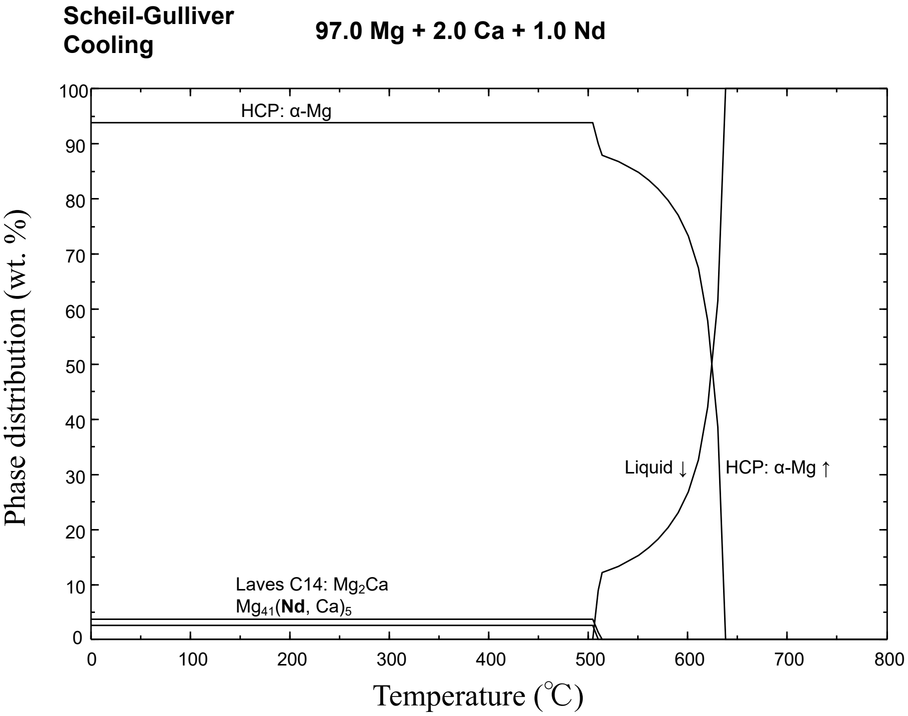

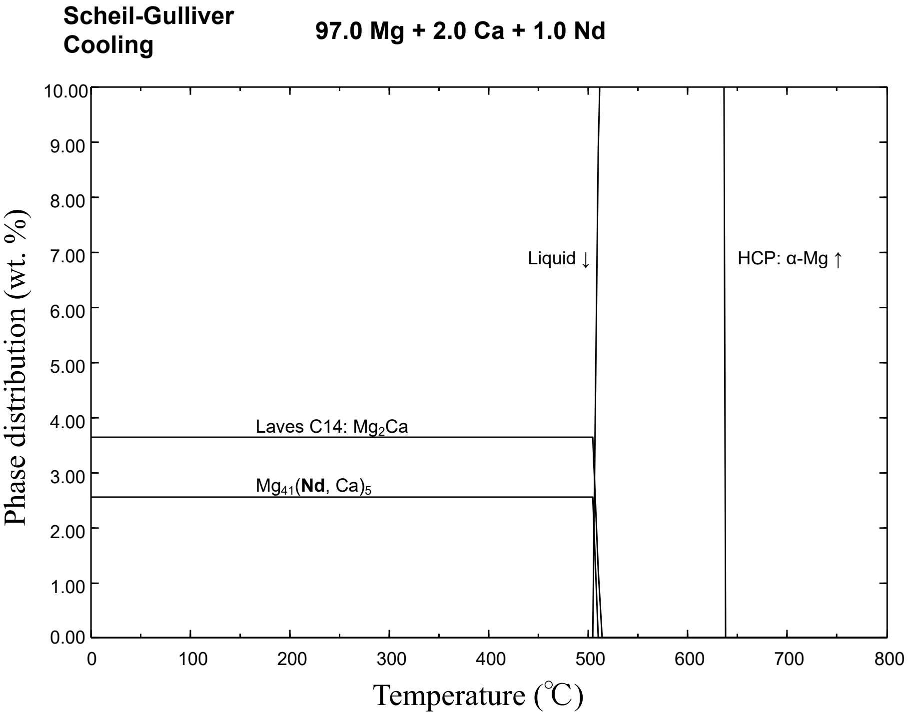

Figure 40, Calculated phase distributions for Mg-Ca-Nd alloys as potential Mg cast alloys in equilibrium and Scheil-Gulliver cooling

6 CONCLUSION

- Thermodynamic optimizations of the binary Ca-RE (RE=Nd, Y, Ce) systems were performed based on assessed literature data. The Modified Quasichemical Model (MQM) and Compound Energy Formalism (CEF) were employed to describe the liquid solutions and solid solutions, respectively.
- DSC experiments for five ternary Mg-Ca-Nd alloys were successfully carried out with sealed Fe capsule. By employing Fe capsule, the oxidation and volatilization of the alloys were successfully eliminated, and experimental results were obtained with good consistency and reliability. This study marks the first time of investigating the phase equilibria up to 40 mol % of Ca and 30 mol % of Nd in this ternary system.
- Thermodynamic optimization on the ternary Mg-Ca-Nd system was performed, and the available experimental results were successfully reproduced. Based on the optimization results, the isothermal phase diagrams and liquidus projection of the ternary system were accurately predicted for the first time.
- The optimized thermodynamic model parameters can be integrated with the available database for Mg alloys and utilized for the design of Mg alloy containing Ca and Nd.

7 REFERENCES

1. Kulekci, Mustafa Kemal. "Magnesium and its alloys applications in automotive industry." *The International Journal of Advanced Manufacturing Technology* 39.9-10 (2008): 851-865.

2. Polmear, I. J. "Magnesium alloys and applications." *Materials science and technology* 10.1 (1994): 1-16.

3. Cole, G. S. "Magnesium vision 2020-a North American automotive strategic vision for magnesium." *IMA-Proceedings*. International Magnesium Association, 2007.

4. Bernard, André, and Analytical Studies Branch. *Recent Trends in Canadian Automotive Industries*. Statistics Canada, 2013.

5. Mordike, B. L., and Tü Ebert. "Magnesium: properties—applications—potential." *Materials Science and Engineering: A* 302.1 (2001): 37-45.

6. Pekguleryuz, Mihriban O., and Jean Renaud. "Creep Resistance in Mg-Al-Ca Casting Alloys." *Magnesium Technology* (2000): 279-284.

7. Zhou, Wei, Naing Naing Aung, and Yangshan Sun. "Effect of antimony, bismuth and calcium addition on corrosion and electrochemical behaviour of AZ91 magnesium alloy." *Corrosion Science* 51.2 (2009): 403-408.

8. Stanford, Nicole. "The effect of calcium on the texture, microstructure and mechanical properties of extruded Mg–Mn–Ca alloys." *Materials Science and Engineering:* A 528.1 (2010): 314-322.

9. Jung, In-Ho, Mehdi Sanjari, Junghwan Kim, and Stephen Yue. "Role of RE in the deformation and recrystallization of Mg alloy and a new alloy design concept for Mg–RE alloys." *Scripta Materialia* 102 (2015): 1-6.

10. Kaufman, Larry, and Harvey Nesor. "Theoretical approaches to the determination of phase diagrams." *Annual Review of Materials Science* 3.1 (1973): 1-30.

11. Kroupa, Ales. "Modelling of phase diagrams and thermodynamic properties using Calphad method–Development of thermodynamic databases." *Computational Materials Science* 66 (2013): 3-13.

12. Saunders, Nigel, and A. Peter Miodownik, eds. *CALPHAD (calculation of phase diagrams): a comprehensive guide*. Vol. 1. Elsevier, 1998.

13. Pelton, A. D., S. A. Degterov, G. Eriksson, C. Robelin, and Y. Dessureault. "The modified quasichemical model I—binary solutions." *Metallurgical and Materials Transactions B* 31.4 (2000): 651-659.

14. Hillert, Mats. "The compound energy formalism." *Journal of Alloys and Compounds* 320.2 (2001): 161-176.

15. Stroganova, V. F., V. F. Terekhova, and E. M. Savitskii. *Diagrammy Sostoyaniya Metallicheskikh Sistem (Constitutional Diagrams of Metallic Systems)*, N.V. Ageev and O.S. Ivanov, Ed., Izdat. Nauka, Moscow. (1971) in Russian.

16. Gschneidner, K. A., and F. W. Calderwood. "The Ca−Nd (Calcium-Neodymium) system." *Bulletin of Alloy Phase Diagrams* 8.6 (1987): 517-518.

17. Predel, B. "Ca-Nd (Calcium-Neodymium)." *Ca-Cd–Co-Zr*. Springer Berlin Heidelberg, 1993. 1-2.

18. Stroganova, V. F., V. F. Terekhova, and E. M. Savitskii. *Redkozemel'nye metally in splavy (Rare Earth Metals and Alloys),* E.M. Savitskii and V.F. Terekhova, Ed., Izdat. Nauka, Moscow, 51 (1971) in Russian.

19. Gschneidner, K. A., and F. W. Calderwood. "The Ca−Y (Calcium-Yttrium) system." *Bulletin of Alloy Phase Diagrams* 8.6 (1987): 519-520.

20. Haynes, William M. *CRC handbook of chemistry and physics*. CRC Press, 2014.

21. Dzuraev, T. D., and R.A. Altynbaev. "Ca-Y (Calcium-Yttrium) Untitled." *Dokl. Akad. Nauk, Tadzh*. SSR 29 (1986): 472. Print.

22. Predel, B. "Ca-Y (Calcium-Yttrium)." *Ca-Cd–Co-Zr*. Springer Berlin Heidelberg, 1993. 1-1.

23. Moffatt, W.G. "Binary Phase Diagrams Handbook", Schenectady, N.Y. General Electric Comp., (1989).

24. Zverev, G. L. "The Ternary Cerium-Calcium-Chlorine System." *Turkdogan, ET and Maddocks, WR* 3290 (1955).

25. Gschneidner, K. A., and F. W. Calderwood. "The Ca−Ce (Calcium-Cerium) system." *Journal of Phase Equilibria* 8.6 (1987): 511-512.

26. Young, David A. *Phase diagrams of the elements*. Univ of California Press, 1991.

27. Predel, Bruno, Hans Landolt, and Richard Börnstein. *Phase equilibria, crystallographic and thermodynamic data of binary alloys*. Vol. 5. Berlin, Heidelberg: Springer, 1991.

28. Gschneidner, K. A., and F. W. Calderwood. The Ca−La (Calcium-Lanthanum) system. *Journal of Phase Equilibria*, 8.6 (1987): 515-516.

29. Gschneidner, K. A., and F. W. Calderwood. The Ca−Pr (Calcium-Praseodymium) system. *Journal of Phase Equilibria*, 8.6 (1987): 518-519.

30. Gschneidner, K. A., and F. W. Calderwood. The Ca−Sm (Calcium-Samarium) system. *Journal of Phase Equilibria*, 8.6 (1987): 519.

31. Gschneidner, K. A., and F. W. Calderwood. The Ca−Eu (Calcium-Europium) system. *Journal of Phase Equilibria*, 8.6 (1987): 513-514.

32. Gschneidner, K. A., and F. W. Calderwood. The Ca−Gd (Calcium-Gadolinium) system. *Bulletin of Alloy Phase Diagrams*, 8.6 (1987): 515.

33. Gschneidner, K. A., and F. W. Calderwood. The Ca−Dy (Calcium-Dysprosium) system. *Journal of Phase Equilibria*, 8.6 (1987): 512-513.

34. Gschneidner, K. A., and F. W. Calderwood. "The Ca−Er (Calcium-Erbium) System." *Bulletin of Alloy Phase Diagrams* 8.6 (1987): 513.

35. Predel, B. "Ca-Tm (Calcium-Thulium)." *Ca-Cd–Co-Zr*. Springer, 1993. 1-1.

36. Gschneidner, K. A., and F. W. Calderwood. "The Ca−Yb (Calcium-Ytterbium) System." *Journal of Phase Equilibria* 8.6 (1987): 521-522.

37. Soderquist, Sven Dale, and FX Kayser. "The Calcium-Ytterbium System." *Journal of the Less Common Metals* 16.4 (1968): 361-365.

38. Predel, B. "Ca-Yb (Calcium-Ytterbium)." *Ca-Cd–Co-Zr*. Springer, 1993. 1-2.

39. Spedding, F. H., A. H. Daane. "Ca-Yb (Calcium-Ytterbium)." IS-350, *Annual Summary Res. Rep. In Chem.*, Jul. 1, 1960–Jan. 30, 1961 (1961).

40. Fei, Hou-jun, Guang-long Xu, Li-bin Liu, B. O. Hong, Li-jun Zeng, and Cui-ping Chen. "Phase equilibria in Mg-rich corner of Mg–Ca–RE (RE= Gd, Nd) systems at 400° C." *Transactions of Nonferrous Metals Society of China* 23.4 (2012): 881-888.

41. Trindade, Vicente Braz, Rodrigo Borin, Behzad Zandi Hanjari, Songlan Yang, Ulrich Krupp, Hans-Jürgen Christ. "High-temperature oxidation of pure Fe and the ferritic steel 2.25 Cr1Mo." *Materials Research* 8.4 (2005): 365-369.

42. Thomas, L. C. "Interpreting unexpected events and transitions in DSC results." *Technical publication TA-039, TA Instruments* (2010).

43. Kang, Youn-Bae, Liling Jin, Patrice Chartrand, Aïmen E. Gheribi, Kewu Bai, and Ping Wu. "Thermodynamic evaluations and optimizations of binary Mg-light rare Earth (La, Ce, Pr, Nd, Sm) systems." *Calphad* 38 (2012): 100-116.

44. Wang, Jian. *Experimental and thermodynamic study on the Mg-X (X: Ag, Ca, In, Li, Na, Sn, Sr and Zn) multicomponent systems*. Diss. École Polytechnique de Montréal, 2014.

45. Pelton, Arthur D. "A general “geometric” thermodynamic model for multicomponent solutions." *Calphad* 25.2 (2001): 319-328.

List of Figures

List of Tables